Journal of CO2 Utilization 100 (2025) 103175

Contents lists available at ScienceDirect

Journal of CO2 Utilization

journal homepage: www.elsevier.com/locate/jcou

Review Article

Ferrite-based nanomaterials for photocatalytic CO_2 reduction: Synthesis, properties, and mechanistic insights

Khaled M. Amin [a,b,*,1], Nada A. Eldeeb [c,1], Zineb Gargar [d,1], Ibrahim M.A. Mohamed [e,**,1], Mohamed Elsenety [f,**,1], Mahmoud M. Emara [c,**,1], M. Abd Elkodous [g,h], Marwa M. Abouelela [g,i], Poussy A. Ibrahim [j], Abdelmoneim A. Ayed [k], Hani Nasser Abdelhamid [l], Hesham A. Hamad [m,n,o,***]

[a] Institute of Energy Technologies, Electrochemical Process Engineering (IET-4), Forschungszentrum Jülich, Jülich 52425, Germany
[b] Department of Polymer Chemistry, Atomic Energy Authority, Cairo 11787, Egypt
[c] Chemistry Department, Faculty of Science, Alexandria University, Baghdad Street, P.O. Box 21511, Moharam Bek, Alexandria, Egypt
[d] Laboratoire des Sciences des Matériaux et Optimisation des Procédés, Faculté des Sciences Semlalia, Université Cadi Ayyad, Marrakech, Morocco
[e] Department of Chemistry, Faculty of Science, Sohag University, Sohag 82524, Egypt
[f] Department of Chemistry, Faculty of Science, Al-Azhar University, P.O.11823, Nasr City, Cairo, Egypt
[g] Department of Electrical and Electronic Information Engineering, Toyohashi University of Technology, 1-1 Hibarigaoka, Tempaku-cho, Toyohashi, Aichi 441-8580, Japan
[h] Center for Nanotechnology (CNT), School of Engineering and Applied Sciences, Nile University, Sheikh Zayed, Giza 16453, Egypt
[i] Petrochemical Department, Egyptian Petroleum Research Institute (EPRI), Nasr City, Cairo 11727, Egypt
[j] 3 Brother for Lighting Solutions Company, 10th Ramadan City, Sharkia 34888, Egypt
[k] Department of Chemistry, Faculty of Science, Tanta University, Tanta 31527, Egypt
[l] Department of Chemistry, College of Science, Imam Mohammad Ibn Saud Islamic University (IMSIU), Riyadh 11623, Saudi Arabia
[m] Fabrication Technology Research Department, Advanced Technology and New Materials Research Institute (ATNMRI), City of Scientific Research and Technological Applications (SRTA-City), New Borg El-Arab, Alexandria, Egypt
[n] Laboratoire d'Electrochimie Moléculaire, Université de Paris, CNRS, Paris F-75006, France
[o] UGR-Carbon, Materiales Polifuncionales Basados en Carbono, Departamento de Química Inorgánica, Facultad de Ciencias - Unidad de Excelencia Química Aplicada a Biomedicina y Medioambiente" Universidad de Granada (UEQ-UGR), Granada 18071, Spain

ARTICLE INFO

Keywords:
Magnetic ferrites
CO_2 conversion
Physicochemical properties
Air purification
Solar fuels

ABSTRACT

The scientific community has shown increasing interest in the use of magnetic nanoparticles, particularly ferrite-based nanomaterials, for the photocatalytic reduction of carbon dioxide (CO_2). Compared to other nanomaterials, they could provide a range of advantageous characteristics, including high performance, low cost, low toxicity, and distinctive magnetic properties that facilitate separation using external magnetic fields. This review offers a comprehensive and updated assessment of ferrite-based magnetic nanomaterials for photocatalytic CO_2 reduction. It uniquely integrates recent advancements in synthesis, properties, and mechanistic insights, highlighting emerging materials to bridge fundamental science with practical challenges for sustainable CO_2 conversion and solar fuel generation. It presents a thorough overview of their synthesis, characterization, and photocatalytic properties, surveying techniques like dimensional tuning, co-catalyst loading, doping, coupling with plasmonic materials, oxygen vacancies, charge separation methods, morphological optimization, porosity enhancement, heterojunction formation, and Z-scheme implementation. By bridging the gap between fundamental science and applied challenges, this review identifies emerging design principles and future directions for developing highly efficient, magnetically recoverable photocatalysts aimed at mitigating CO_2 emissions through solar-driven chemical transformation.

* Corresponding author at: Institute of Energy Technologies, Electrochemical Process Engineering (IET-4), Forschungszentrum Jülich, Jülich 52425, Germany.
** Corresponding authors.
*** Corresponding author at: Fabrication Technology Research Department, Advanced Technology and New Materials Research Institute (ATNMRI), City of Scientific Research and Technological Applications (SRTA-City), New Borg El-Arab, Alexandria, Egypt.
E-mail addresses: khaledamin89@gmail.com, k.amin@fz-juelich.de (K.M. Amin), ibrahim_mohamed@science.sohag.edu.eg (I.M.A. Mohamed), m.elsenety@azhar.edu.eg (M. Elsenety), mahmoud.emara@alexu.edu.eg (M.M. Emara), hhamad@srtacity.sci.eg, heshamaterials@hotmail.com (H.A. Hamad).
[1] Equal contribution

https://doi.org/10.1016/j.jcou.2025.103175
Received 15 April 2025; Received in revised form 26 June 2025; Accepted 12 July 2025
Available online 22 July 2025

1. Introduction

Environmental pollution and the energy crisis are amongst the most significant contemporary global challenges [1–3]. Both the generation of power and its use have substantial repercussions for the natural environment. Among several methods, photocatalytic technology is one of the viable approaches that offers several advantages, including the low cost of the process, as well as operation under ambient pressure and temperature [4,5]. However, based on the relevant literature and a number reviews, the main technical barriers that limit the utilization of photocatalysts include the following: (i) first and foremost, the quantified energy bandgap structure implies the absorption of a quantified amount from the solar spectrum, which leads to low energy utilization; (ii) the e^-/h^+ rapid recombination via heat generation or luminescence; and (iii) difficulty in the direct recovery and isolation of photoactive materials after catalysis [6,7]. All these constraints hamper economic characteristics and the long-term sustainability of heterogeneous photocatalyst materials. Consequently, the chemical fabrication of an appropriate photocatalyst that is active in solar power generation is critical to achieving acceptable photocatalytic efficiency results. Therefore, the chemical design of high-performance, easily separated photocatalysts is a priority in photocatalysis technology.

Among several materials that can be used as photocatalysts, titanium dioxide (TiO_2) is the most extensively studied, owing to its powerful oxidation power, chemical and biological inertness, low cost, and high stability across a broad pH range [8,9]. TiO_2 is considered a pioneering and well-studied photocatalyst due to its high reactivity, eco-friendliness, and sufficient stability, as well as a bandgap of 3.03 eV (rutile), and 3.18 eV (anatase). While the bandgap of TiO_2 is appropriate for photocatalysis compared to other metal oxides e.g., ZnO, CdS, and WO_3 [10–13], TiO_2 faces significant limitations: TiO_2 can only absorb a small portion of the visible region of sunlight and is difficult to separate and recover after a photocatalytic reaction [14,15].

To address these fundamental limitations, particularly the challenges of visible light utilization and catalyst recovery, magnetic photocatalysts have emerged as a promising solution. Magnetic photocatalysts were first developed by Hiroshi *et al.* in 1994, who prepared magnetic photocatalysts via the deposition of TiO_2 over a magnetite substrate [16]. Magnetic materials have gained increasing priority in several disciplines, such as catalysis [17,18], biomedicine/biotechnology [19–22], and water treatment [23–25]. Magnetic photocatalysts offer alternative solutions to the issues of visible light response and catalyst recovery challenges. The integration of magnetic properties into photocatalysts has been developed to take advantage of both high activity and the easy reusing of semiconductor photocatalysts. Magnetic nanoparticles (MNPs) have emerged as promising candidates for the photocatalytic reduction of carbon dioxide (CO_2) and photocatalytic degradation of hazardous compounds due to their unique advantages, including high performance, low cost, low toxicity, and distinctive magnetic properties. Several thorough reviews have already been published that focus on magnetic photocatalysts [7,26–28]. However, few evaluations have concentrated on the adaptable qualities and logical construction of magnetic-based photocatalysts.

Recently, photocatalytic CO_2 reduction has gained significant attention due to its dual role in addressing both energy shortages and greenhouse gas mitigation [29]. Compared to other nanomaterials like TiO_2, which often suffer from challenges such as rapid electron-hole recombination and difficult post-reaction separation, ferrite-based magnetic nanomaterials offer significant advantages due to their tunable magnetic properties, narrow bandgaps, and structural versatility [30]. Despite their promise, a systematic and focused evaluation of their synthesis strategies, structure-activity relationships, and mechanistic roles in photocatalytic CO_2 reduction is still lacking. Most prior reviews have only broadly addressed materials properties including heteroatom-doped/hierarchical porous carbon materials [31], transition metal nitrides [32], porous aromatic frameworks [33], covalent heptazine framework [34], MXene@MOF [35] as well as ferrites [36] without studying deeply into the nuanced role of ferrites in photocatalytic applications.

This review aims to fill this critical gap by providing a contemporary and comprehensive analysis of ferrite-based magnetic nanomaterials, emphasizing their synthesis, structural modification, and photocatalytic mechanisms with a focus on their application in heterogeneous photocatalysis for environmental remediation and sustainable energy conversion. The review will elucidate the key features required by the research community to gain a comprehensive understanding of the behaviors shown by magnetic materials in the context of generation of solar fuels through CO_2 reduction, and provide insights into the design and development of MNP-based photocatalysts with enhanced performance for environmental remediation and sustainable energy production. Particular emphasis is placed on performance-enhancing techniques such as bandgap engineering, charge carrier optimization, and hierarchical morphology regulation. The photocatalytic activity of MNPs can be further enhanced through dimensional tuning, co-catalyst loading, doping, and coupling with plasmonic materials, the utilization of oxygen vacancies, charge separation approaches, morphological considerations, porosity optimization, heterojunction formation, and the implementation of the Z-scheme. These techniques can be used to tailor the physicochemical characteristics of MNPs, such as their bandgap energy, surface area, and charge separation efficiency, in order to achieve optimal photocatalytic performance. This review provides an integrated overview of the synthesis, characterization, and photocatalytic characteristics of ferrite-based magnetic nanomaterials, and offers a comprehensive examination of several techniques employed to promote photocatalysis for air purification and energy conversion applications. By integrating current advancements and addressing key knowledge gaps, this review provides valuable insights into the design of next-generation magnetic photocatalysts with enhanced activity, selectivity, and reusability. We believe that the information presented will inform future advancements in practical and scalable photocatalytic devices, facilitating clean energy generation and environmental remediation and helping to address the difficulties associated with the widespread use of magnetic-based photocatalysts in the production of renewable and sustainable energy.

2. Magnetic photocatalysts

The most extensively used iron oxide-based materials are magnetite (Fe_3O_4), maghemite (γ-Fe_2O_3), and MFe_2O_4 (where M stands for divalent metallic cations, e.g., Cu, Zn, and Co). Magnetic photocatalysis has received extensive attention due to its paramagnetic/ferrimagnetism, moderate environmental impact, low-toxicity, high-adsorption capacity, and stability [37]. A primary advantage is their simple recovery for liquid phase reactions, eliminating the need for complex centrifugation or filtration, which contributes to increased durability by preventing agglomeration. Unfortunately, some drawbacks have been raised by implementing magnetic photocatalysts, such as photocatalytic performance and their stability as the contact between the utilized photocatalysts and magnetic particles causes the photogenerated electron–hole recombination and the photo-dissolution of the magnetic particles [14]. Magnetic photocatalysts can be simply recovered for liquid phase reactions [28]. One of the main advantages of magnetic separation is the conformity removal of the enforced catalyst from the liquid phase without complex centrifugation, filtration, or other impractical approaches for recycling, leading to expected durability increasing due to their agglomeration-avoiding properties [38,39].

To circumvent such limitations of the low photocatalytic activities, several approaches have been implemented by research and overcome the technical issues. In addition, many attempts have been made to modify the structural, optical, electrical, and photoelectrochemical properties, which resulted in improvement in the photocatalytic activity of iron oxide-based nanomaterials such as doping [40]. Another strategy

for improving photocatalytic activity is the coupling of magnetic materials with semiconductor photocatalysts, which seems to be one of the most adequate solutions. The validity of the separation of non-magnetic materials can be accomplished using magnetically-separable materials in the hybrid photocatalytic framework [41–43].

Bibliometric analysis is a crucial statistical tool for mapping the top of the line in certain areas of research and identifying critical data for a variety of reasons, including identifying potential research topics and corroborating findings. The technique involves tools for identifying and analyzing indexed keywords based on the number of citations, revealing general trends through keyword analysis, and identifying and clustering knowledge gaps in recent publications. The network and density visualization (Fig. 1) demonstrate a bibliometric mapping analysis employing the most recent 5000 results up to the year 2025, as documented in Scopus. The Data were collected using the keywords "ferrites", "magnetic materials", and "magnetite". This map visually represents the interconnectedness of research themes, highlighting prominent areas of investigation and emerging trends within the field of magnetic materials. It reveals clusters of related works and identifies key research directions, thereby providing a foundational context for the current review by illustrating the historical and contemporary landscape of ferrite research.

3. Fundamentals of ferrite-based magnetic photocatalysts

The increased appeal of transition metal oxides, endowed with magnetic properties, can be readily elucidated in light of their promising conductivity, catalytic performance, magnetic characteristics, electronic properties, and photo response [44]. Of the several types of magnetic nanoparticles, ferrites are a particularly noteworthy category of magnetic materials that have found broad application in numerous fields. As the magnetic response is strongly dependent on porosity, surface area, and the size of the prepared particles, the synthesis of particles with different sizes could allow for the tailoring of the particles to specific applications [6,45].

Ferrites represent a category of ceramic materials that are produced through the process of combining and heating iron (III) oxide (Fe_2O_3, often known as rust) with one or more metallic elements, including, but not limited to, manganese (Mn), strontium (Sr), barium (Ba), zinc (Zn) and nickel (Ni). Most of the reported ferrites have the chemical formula $M^{2+}Fe_2^{+3}O_4^{2-}$; wherein M is indicative of divalent metal ions, including Ni^{2+}, Mn^{2+}, Cd^{2+}, Zn^{2+}, Mg^{2+}, Fe^{2+}, and others. Combining two or more types of M^{2+} ions, or a monovalent ion with a trivalent metal ion, results in the creation of mixed ferrites that can be modified and tailored to specific applications. Ferrites are ferrimagnetic oxides that possess both high magnetic and high electrical resistivity. The saturation magnetization of ferrites is less than half that of ferromagnetic alloys; nevertheless, they possess advantages like withstanding high frequencies, greater heat resistance, lower prices, and higher corrosion resistance. In recent studies, some ferrites have been reported as electrophotocatalyst, including NiCo nanoferrites [46]. Ferrite-based electrophotocatalysts have exhibited inherent limitations that include low conductivity, a limited redox-active surface area, and inefficient charge-transfer kinetics. These issues could be addressed through the following

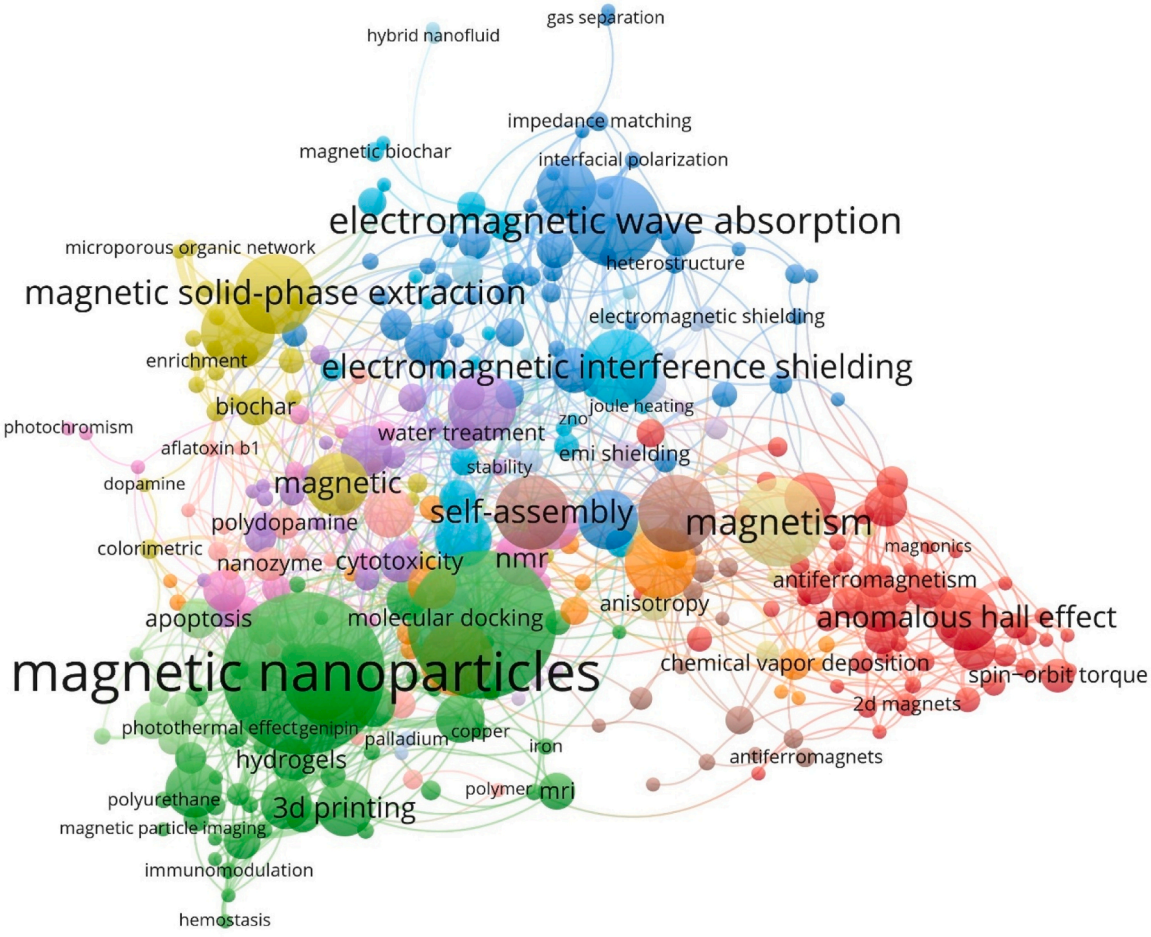

Fig. 1. Bibliometric mapping: network visualization and density visualization of research themes related to ferrites, magnetic materials, and magnetite, based on recent Scopus data. The map illustrates the interconnectedness of research areas, highlighting prominent topics and emerging trends within the field of magnetic materials.

approaches: doping, heterostructure engineering, integration with conductive frameworks, and defect modulation strategies to enhance charge carrier dynamics.

4. Synthesis strategies of ferrite nanoparticles

The development of diverse techniques for the synthesis of ferrite nanoparticles has been the subject of substantial research over the last decade. To create ferrite nanoparticles of the optimal size, shape, stability, and biocompatibility, various synthetic approaches have been employed. The synthesis process is governed by two factors: practicability and cost-effectiveness. The magnetic iron oxide photocatalysts' inherent colloidal characteristic makes the synthesis process time-consuming. Advanced chemical-based synthetic approaches including co-precipitation [47,48], microemulsion[48,49], thermal decomposition, microwave [50,51], hydrothermal (solvothermal) [52,53], sonochemical [53,54], and biosynthesis approaches [55,56] have been followed for the synthesis of ferrite-based magnetic photocatalysts (Fig. 2).

4.1. Co-precipitation

Hydrolytic coprecipitation, which utilizes the Massart process, is a method for designing MNPs on a large scale that has been recognized in the scientific community [57]. The coprecipitation is carried out Fe^{2+}/Fe^{3+} salt solution with a high pH value, at either ambient or elevated temperatures. The rapid growth of monomers has exceeded the critical supersaturation, followed by slower growth, resulting in the synthesis of small particle sizes in the nanoscale range. Thereafter, the nuclei develop at the same speed, resulting in monodisperse NPs [58]. Even though this rapid approach has extraordinary shape and phase homogeneity control, it has poor size control [59]. Experimental characteristics, such as the practiced temperature, pH, and salts employed, Fe^{2+}/Fe^{3+} ratio, as well as the nature of the base, have a significant consequence on the size and form of the designed NPs. However, the pH parameter is one that affects the size of MNPs [60]. The repulsion among initial MNPs adds smaller magnetite NPs as the pH of the reaction rises. Overall, this method makes use of low-cost ingredients and moderate reaction conditions, and it may be used to directly synthesize nanoparticles in water. Topel *et al.* and Bhandari *et al.* developed polyethyleneimine (PEI)-coated Fe_3O_4 NPs with a measured diameter of approximately 10 nm that were covalently coupled with fluorophores using a modified coprecipitation process [61,62]. Shape-controlled iron oxide nanoparticles can also be made using the coprecipitation approach. Shen *et al.* have recently studied the production of Fe_3O_4 NPs with improved saturation magnetization in different forms, including nanocubes, nanoneedles, and nanospheres using a coprecipitation approach, and by changing the proportion of surfactant. The morphology of the prepared materials can be controlled via the amount of surfactant (sodium dodecyl sulfate), according to the results from transmission electron microscopy (TEM) [63].

4.2. Hydrothermal

The hydrothermal process is defined as the development of ferrite nanoparticles in an aqueous environment under conditions of elevated pressure and temperature, which are meticulously calibrated to ensure optimal functionality [64]. This approach uses a sealed container or autoclave to perform a chemical reaction at a certain temperature and high vapor pressure. The procedure is known as hydrothermal synthesis when water is used, with the reaction solvent and another solvent being referred to as solvothermal synthesis. The production of crystalline ferrite nanoparticles of uniform size can be achieved through the execution of reactions in aqueous solutions at elevated temperatures and pressures [65]. Various studies have been published on using hydrothermal synthesis to produce iron oxide MNPs, either with or without the use of stabilizing surfactants [66,67]. A surfactant-free hydrothermal approach was developed to create iron oxide NPs with nano-sized holes. The produced samples were calcined in air and nitrogen, yielding MNPs with cavities ranging from 7 to 15 nm and 5–12 nm in diameter, respectively [68]. The shape and crystallinity of the produced MNPs were determined by the correct solvent mixture, time, pressure, and temperature. When compared to the microemulsion method, this method can produce better NPs. However, because this procedure

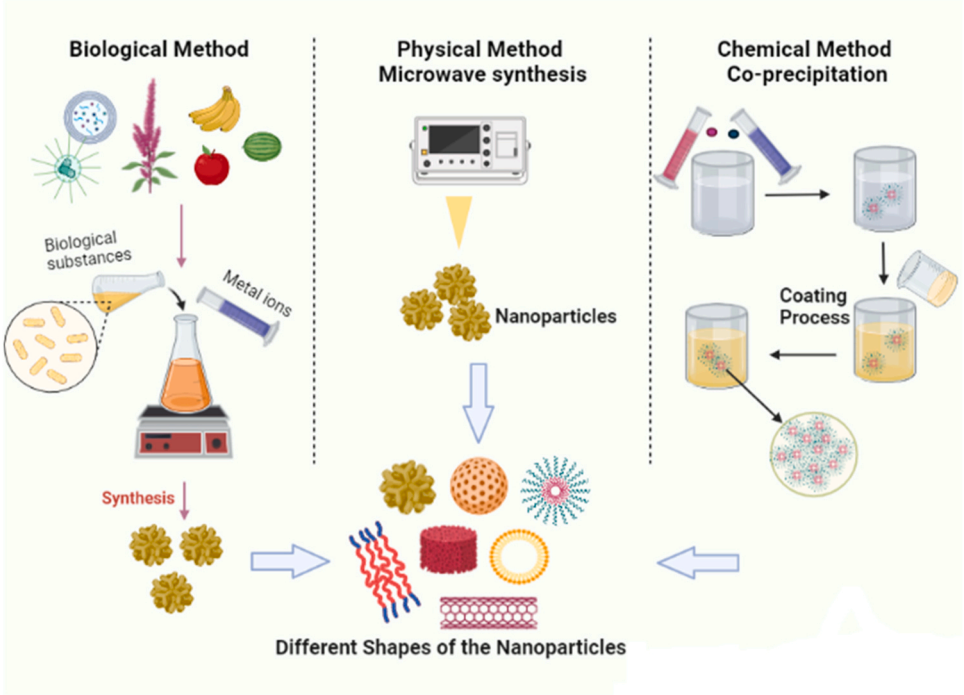

Fig. 2. Diverse fabrication strategies for spinel ferrite-based nanomaterials, illustrating biological, physical, and chemical methods. The figure was created with BioRender.com.

necessitates high pressure and requires more power, it must be carried out with extreme caution and with specialized equipment. In comparison to sol-gel and other approaches, the hydrothermal process is favored because it produces NPs of the desired shape, size, crystallinity, and composition consistency [69]. However, as the reaction requires high temperatures and pressures and the use of special reactors, the strategy is not as energy-efficient if compared with other simple fabrication methodologies.

4.3. Microemulsion

Based on thermodynamics, microemulsion is a stable isotropic dispersion of two immiscible phases (like water and oil) in the presence of surfactants or co-surfactants. The monolayer could be formed at the interface layer between the two phases of water and oil [70]. The fundamental disadvantage of hydrolytic methods is their inability to obtain a homogeneous size in the synthesized ferrite NPs. As a result, amphiphilic molecules (surfactants) were used to improve reaction conditions by creating nanoreactors in which the coprecipitation process could take place in constrained environments, either as micelles or reverse micelles. The aqueous phase microemulsions (water-in-oil, w/o) were distributed as micro-droplets (typically less than 50 nm in diameter) in the continuous hydrocarbon phase, which was enclosed by the utilized surfactant molecules. The contents of the utilized surfactant affect the reverse micelle size [71]. The microdroplets in bi-identical microemulsions (w/o) carrying the appropriate reactants would then collide, consolidate, and break, eventually forming precipitate in the micelles [72]. However, by adding a solvent to the microemulsions (like ethanol or acetone), the precipitate could be easily removed via centrifuging or filtration. Microemulsions could be employed in this situation. The w/o microemulsion technique was utilized to design ferrite NPs through the use of several types of surfactants to evaluate the shape, size, homogeneity, and crystallinity of the produced MNPs. The oil phase was n-heptane, with traditional one-chain surfactants and new Gemini surfactants, whereas the co-surfactant phase was n-hexanol. The displayed results reveal that the film flexibility of reverse micelles and the lifetime of a surfactant in the formed micelle have a substantial impact on nanocrystalline nucleation and growth. Furthermore, the temperature of the samples had a major effect on crystal defects, with the hydrophobic chain length having a significant impact on the lattice defect in response to temperature changes [73]. Consequently, the microemulsion approach has a significant impact on the design of MNPs with limited size distribution and homogeneous magnetic characteristics, given the increased size control. However, when compared to the coprecipitation process, the microemulsion route produces MNPs with poorer yields and lower crystallinity. However, it has been demonstrated that heating the reverse micelle improves the crystallinity of ferrite. Scaling up is also problematic because of the sensitivity of the preparation environments, the necessity for significant volumes of non-aqueous solvent, and the difficulty of removing the utilized surfactants [74].

4.4. Thermal decomposition

Thermal decomposition has been employed to produce high-quality ferrite MNPs [75] [71,76]. The procedure entails the decomposition of metal components in boiling organic solvents in the presence of surfactants, thereby yielding stable MNPs with well-defined magnetic characteristics [77]. The key reason for the success of this method can be attributed to the rapid burst nucleation followed by crystallization. The process can be further optimized by controlling associated factors, such as the type of precursor and surfactant, their relative ratios, solvent, reaction temperature, and reaction duration [70]. Earlier studies have described the thermal decomposition method for synthesizing MNPs with a limited size distribution in the range of 3–50 nm and form control, exhibiting spherical or cubic morphology [78,79]. Hufschmid *et al.* studied the chemical production of iron oxide NPs from the degradation of various precursors for their capacity to create NPs with specific size and phase purity requirements [75]. In contrast, the creation of harmful organic–soluble solvents is a danger factor associated with this approach, which decelerates its practice in the biomedical sector [50]. For producing magnetic particles of smaller sizes, the thermal composition is more recommended than coprecipitation.

4.5. Microwave-assisted technology

The microwave-assisted methodology has gained interest due to its merits of quick volumetric heating, higher rate of reaction, reduced reaction time, and increased familiar yield [80]. Microwaves can be employed as another source of heat, either on their own or in combination with other synthesis methods. This method has been classified as a non-hydrolytic approach because the microwave-assisted technique is frequently paired with thermal breakdown. It can also be used to speed up hydrolytic processes such as hydrothermal and sol-gel. Microwave-assisted polyol methodology was used to produce spinel-structured $M^{II}Fe_2O_4$ (M is Mn or Co) NPs with diameters smaller than 10 nm [81]. The small particle sizes are most likely the consequence of the microwave synthesis's rapid and homogenous reactions. They discovered that by altering the water ratio to ethylene glycol (EG) during microwave heating, they could control the reaction temperature and crystal quality. Gonzalez-Moragas *et al.* recently reported on the production of aqueous–dispersible iron oxide NPs using a microwave-aided methodology. They used multimode equipment to raise the volume of the reaction from 4.5 up to 50 mL, resulting in a significant reduction in the compulsory cost, energy, and duration of producing high quantities of MNPs [51]. The fundamental benefit of introducing microwaves into the reaction system is the ability to obtain an exceptionally fast kinetic crystallization. However, other approaches, including thermal decay, co-precipitation, and so on, require processes for improving crystallinity due to long reaction periods, which account for industrial or commercial usage.

4.6. Sonochemical method

This approach utilizes the acoustic cavitation phenomenon for synthesis due to the constant production, expansion, and abrupt collapse of bubbles in solutions. When the solution container is placed in an ultrasonic reactor with a high cooling rate, high pressure, and a high temperature, NPs are created by the collapse of bubbles accompanied by severe shockwaves and micro-jets [82]. As the bubbles have already been formed, they have effectively accumulated ultrasonic energy and a vacuum emboldens the diffusion of solute vapor into their volumes, resulting in the development of bubbles. This growth may continue until the bubble reaches its maximum size and collapses, releasing the stored energy [83]. It has been established that the substantial cooling rates of collapsed bubbles yield amorphous or, in other words, low-crystalline NPs. Conversely, non-volatile precursors have the capacity to yield nanostructured products [84]. Abbas *et al.* used a sonochemical approach to make homogenous ferromagnetic magnetite nanocubes in the absence of surfactants [85]. To enhance the crystallinity of the magnetic nanocubes, a 600 °C annealing process was employed. However, the presence of a thin non-magnetic dead layer on the surface resulted in a reduction of the saturation magnetization with increasing annealing temperature. the presence of a thin non-magnetic dead layer on the surface resulted in a reduction of the saturation magnetization with increasing annealing temperature. Bang *et al.* introduced the use of carbon templates to produce nanoscale particles from hollow iron oxides [86]. The assembled NPs were crystalline hematite with extremely weak ferromagnetism and were thermodynamically-stable.

Notwithstanding the necessity for the ultrasound irradiation mechanism, the sonochemistry methodology significantly reduces the anticipated reaction time by enhancing mixing through a non-invasive

energy mechanism. The process under investigation yields NPs that exhibit a restricted, homogeneous size distribution. Additionally, these NPs demonstrate high crystallinity and adequate dispersity.

4.7. Biosynthesis

The green source preparation of NPs via the biosynthesis method has gained wide attention [87]. The process involves the implementation of various techniques aimed at the elimination of hazardous compounds, thereby ensuring environmental safety. Plants are currently being studied for their ability to biosynthesize metal NPs, which can be synthesized utilizing plant tissue [88], extract [89–91], exudates [92], fungi [93], and enzymes [94]. It is critical to address effective procedures for the synthesis of NPs for further biomedical uses [95]. In addition, utilizing plants could sometimes be more advantageous than other biological procedures, as it eliminates the time-consuming of maintaining microbial cultures [96]. The application of *F. oxysporum* and *Verticillium sp.* with an aqueous solution of ferricyanide $[Fe(CN)_6]^{3+}$ and ferrocyanide $[Fe(CN)_6]^{4+}$ has been demonstrated to produce magnetite NPs with proper stoichiometr. *F. oxysporum* has been observed to yield quasi-spherical magnetite NPs with a particle size ranging from 20 to 50 nm, while the Cubo octahedral magnetite NPs were produced by *verticillium sp.* and revealed a size in the range of 100–400 nm [97]. *Lagenaria siceraria* leaves generated cubic and well-stable biomagnetic Fe_3O_4 NPs (BMNPs) with a size of 30–100 nm using a hot water extract. The antioxidant behavior and biocidal activity against *Escherichia coli* and *Staphylococcus aureus* were enhanced [98]. The aqueous extract of the Lantana camera was used to make a less costly and environmentally friendly design of iron oxide NPs [105]. The photosynthesized NPs were proven to be pure and crystalline, with a particle size of 10–20 nm. Moreover, Sandhya and Kalaiselvam used an alcohol extract of Borassus flabellifer L. seed peels to synthesize hexagonal facets 35 nm Fe_3O_4 NPs [98]. For the construction of magnetite NPs, the biosynthesis method has several advantages: it is non-toxic, cost-effective, and ecologically friendly methodology. However, the state of reaction and the size of the magnetite NPs can be regulated in a single-vessel reaction under low conditions.

4.8. Comparative overview of synthesis strategies

The method of synthesizing ferrite-based magnetic nanoparticles used in photocatalytic CO_2 reduction greatly influences their properties and performance. Different techniques offer varying degrees of control over size, crystallinity, and surface characteristics. It is therefore essential to select an appropriate synthesis approach, bearing in mind that each method offers specific advantages and limitations with regard to control over nanostructure, scalability, cost and environmental impact (Table 1). There are trade-offs in terms of scalability, cost, and environmental impact.

The choice of synthesis method for ferrite-based materials is critical and depends heavily on the intended application, particularly for the photocatalytic reduction of CO_2. While co-precipitation is simple and inexpensive for large-scale production, precise control over particle size and homogeneity is often difficult to achieve, which can impact photocatalytic efficiency. Conversely, hydrothermal synthesis yields highly crystalline and uniformly sized nanoparticles, but the high pressure and temperature required limit its energy efficiency and scalability for industrial applications. Microemulsion methods provide excellent control over size, but suffer from low yields and the need for large volumes of organic solvents. Thermal decomposition can produce high-quality, monodisperse nanoparticles, but it involves the use of toxic organic solvents. Microwave and sonochemical methods offer rapid synthesis and improved crystallinity, but they still require further development for mass production. Biosynthesis, while environmentally friendly, presents challenges in controlling particle size and properties. Therefore, for efficient photocatalytic CO_2 reduction, methods that offer a balance between precise control over material properties (e.g., bandgap, surface area, defect concentration) and scalability, cost-effectiveness, and environmental benignity are preferable. Future research should focus on optimizing hybrid approaches or developing novel green synthesis routes that can achieve high yield, purity, and controlled nanostructures suitable for industrial-scale CO_2 conversion.

5. Physico-chemical properties of ferrites-based magnetic photocatalysts

It is well known that the comprehensive properties of ferrites themselves, including their crystal structural, surface physicochemical, stability, optical, adsorption, electrochemical, photoelectrochemical, and electronic properties, critically determine the photocatalytic efficiency of ferrite-based magnetic photocatalysts. Consequently, fundamental comprehension and deterministic control of the previously mentioned characteristics will allow for the rational design and scalable production of ferrite-based magnetic nano photocatalysts with optimized photocatalytic behavior. This will be advantageous for developing some sturdy ferrites-based magnetic nanomaterial systems for practical photocatalytic applications, as well as fundamental insights into photocatalytic enhancement mechanisms at the single-atom level. The performance of ferrite-based nanomaterials for photocatalytic CO_2 reduction is intricately linked to their intrinsic structural and morphological characteristics. Structural and chemical features determine phase purity and composition, while vibrational analysis reveals bonding and molecular interactions. Surface area and functional groups affect reactivity and dispersion. The specific morphology of nanostructures is vital; two-dimensional (2D) nanosheets, for example, offer maximized surface exposure and reduced charge carrier diffusion distances, facilitating more efficient reactions [106]. Furthermore, controlled defect engineering, such as the introduction of oxygen vacancies, can create

Table 1
Comparative analysis of synthesis methods for ferrite-based magnetic photocatalysts.

Technique	Advantages	Disadvantages	Ref.
Coprecipitation	Mild conditions; Synthesis in aqueous media; Large quantity	Time-consuming; Low reproducibility; Impurities	[99]
Hydrothermal	Narrow scale-size distribution; Good crystallinity; Synthesis in aqueous media	High T; High P; Special autoclaves	[100]
Sonochemistry	High crystallinity; Saturation magnetization; Narrow size distribution; Good dispersivity	Ultrasound wave irradiation equipment is required; The mechanism is still not well understood	[101]
Microemulsion	Thermodynamically stable; Improved size control	Poor crystallinity; Low reaction yield; Huge quantities of organic solvents are required; High temperature and pressure	[102]
Thermal decomposition	High yield; Controllable size; High crystallinity	High temperature; Toxic organic solvents	[50]
Microwave-assisted	Rapid kinetic for crystallization; High yield of product; high energy efficiency	Homogeneous nucleation occurs Because of uniform heating; Need for organic solvent	[51, 103]
Biosynthesis	Higher biocompatibility; Environmentally-/eco-friendly reducing agent	Difficult control in terms of size and properties; High temperature; Poor reproducibility	[104, 105]

mid-gap states that improve visible light absorption and facilitate charge separation within the ferrite crystal lattice. Magnetic measurements provide insights into spin dynamics and superparamagnetism, and optical/photoelectrochemical properties govern light absorption and charge transfer. Understanding these interconnected features is essential for optimizing MNPs for targeted applications.

5.1. Structural properties

The incorporation of the transition metal oxides with spinel structures brings up the most important magnetic photocatalysts, which are designated as ferrites. Depending on their crystallinity, ferrites can be classified into four distinct categories as presented in Fig. 3: (i) spinel (MFe_2O_4, where M is Ni, Fe, Zn, Cu… etc.); (ii) garnet ($M_3Fe_5O_{12}$, where M is rare earth elements); (iii) hexagonal ($MFe_{12}O_{19}$); and (iv) ortho-ferrite ($MFeO_3$) [107–109].

Spinel ferrites are a diverse type of material with a wide range of electronic, magnetic, and chemical aspects. Spinel transition metal oxides (AB_2O_4) containing two metals have recently shown the ability to tune the energy density and working voltage by regulating the metallic configuration [110,111]. Spinel ferrites have been used in inductors, transformers, magnetic recording, gas sensors, and photocatalysts, amongst other applications. The different spinel types of ferrites are classified into three groups based on the positions of ferric ions on the crystal lattice as follows:

a) Normal spinel ferrites

A typical spinel structure, in which cations (II) exclusively occupy the tetrahedral site and Fe (III) ions utilize the octahedral site, is characteristic of this class of compounds. The structural formula could be $[M^{2+}]_{Tetra}[Fe^{3+}]_{Octa}O_4$, where M denotes divalent cations (II) while 'tetra' and 'octa', refer to tetrahedral, and octahedral sites, respectively. It is imperative to note that only one type of cation is permitted at each location. $ZnFe_2O_4$ is an example of a normal spinel, in which the divalent Zn^{2+} accommodates the tetrahedral regions, with the octahedral locations accommodated by Fe^{3+} [112,113]. Spinel ferrite, Fe_3O_4, which belongs to the ferromagnetic materials, possesses a cubic system and an inverse spinel structure with Fd3m [114]. The unit cell of magnetite (Fe_3O_4) contains Fe^{3+} and Fe^{2+} ions with good magnetic properties and 32 oxygen ions in regular cubic closed packs with vacancies in Fe sites, which induce reduced symmetry of crystals [115].

b) Inverse spinel ferrites

In the inverted spinel structure, cations (II) occupy the octahedral locations, whereas Fe(III) accommodates both tetrahedral and octahedral sites. The inverse spinel has the chemical formula $[Fe^{3+}]_{Tetra}[M^{2+}\ Fe^{3+}]_{Octa}O_4$. Two cations, namely the divalent and trivalent Fe (III) ones, accommodate the octahedral site [113]. The naturally occurring spinel structure Fe_3O_4 possesses an inverse spinel structure, with Fe^{2+} accommodating octahedral sites and Fe^{3+} encompassing both octahedral and tetrahedral positions.

c) Mixed spinel ferrites

In a mixed spinel structure, the divalent and trivalent cations occupy both octahedral and tetrahedral positions. These cations are partially housed on octahedral and tetrahedral sites to create the mixed spinel structure [116,117], which has the formula $[M^{2+}_{1-\delta}Fe^{3+}]_{Tetra}[M^{2+}_{\delta}Fe^{3+}_{2-\delta}]_{Octa}O_4$, where δ is the inversion degree. In the case of a mixed spinel structure, two metal ions (M^{2+}) and (Fe^{3+}) are distributed on tetrahedral and octahedral sites [118]. A well-known example of mixed spinel ferrite is copper ferrite ($CuFe_2O_4$). It is worth mentioning that the metal cations in both sites are distributed according to their tendency to occupy the positions, which is influenced by many parameters such as stabilization energy, radii of metal cations, interstitial site size, synthesis approach, and reaction conditions during the synthesis [119,120]. The coordination between the cations and oxygen atoms of octahedral and tetrahedral positions for a mixed spinel structure is described in Fig. 4 [121–124].

Mixed metal spinel ferrites possess a single-phase cubic system [126]. $Ni_{0.7}Zn_{0.3}Fe_2O_4$ is a two-mixed spinel ferrite in which Zn^{2+} ions incline towards tetrahedral sites and Ni^{2+} ions have a strong tendency to lie in octahedral sites [37], but Fe^{3+} ions occupy both T_h and O_h ones. Upon adding Mn^{2+} ions, which fully occupy A-sites, we obtain the three mixed spinel ferrite $Ni_{0.7-x}Zn_{0.3}Mn_xFe_2O_4$. As a result of the introduction of Mn^{2+} ions into the A-sites, Fe^{3+} is shifted from the T_h sites to the O_h ones. In the case of $Ni_{0.7-x}Zn_{0.3}Co_xFe_2O_4$, when Ni^{2+} ions are substituted by Co^{2+} ions to the octahedral sites, a small amount of Zn^{2+} ions in the T_h sites change their positions to O_h sites [127].

Sharma *et al.* synthesized $CoFe_2O_4$, $NiFe_2O_4$, $CuFe_2O_4$, and $ZnFe_2O_4$ spinel ferrite [128]. The recorded XRD patterns displayed the formation of a single-phase FCC crystal structure. The lattice parameter "a" value could be calculated from the most intense (311) reflection using the formula $(1/d^2_{hkl} = (h^2+k^2+l^2)/a^2)$ corresponding to the Fd3m cubic spinel structure. The steady addition of Co^{2+} ions resulted in an obvious reduction in the lattice parameter "a" from 8.420 to 8.341 Å, which may be due to the different ionic radii of Co^{2+} (0.072 nm) and Zn^{2+} (0.074 nm). Furthermore, small scattering domain sizes are indicated in four $Zn_{1-x}Co_xFe_2O_4$ (x = 0, 0.03, 0.1, 0.2) samples, as wide diffraction lines can be observed. The coherent diffraction domain size and full width at half maximum (FWHM) values of the (311), (511), and (440) diffractions, were in the range of 9–12 nm. However, due to its higher crystallinity, the $Zn_{0.6}Co_{0.4}Fe_2O_4$ sample revealed a 27 nm bigger domain size.

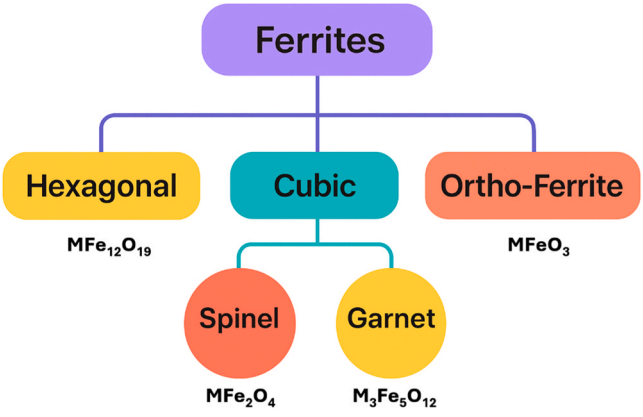

Fig. 3. Schematic classification of ferrites according to their crystal structure, showing the four major types: spinel, garnet, hexagonal, and ortho-ferrite.

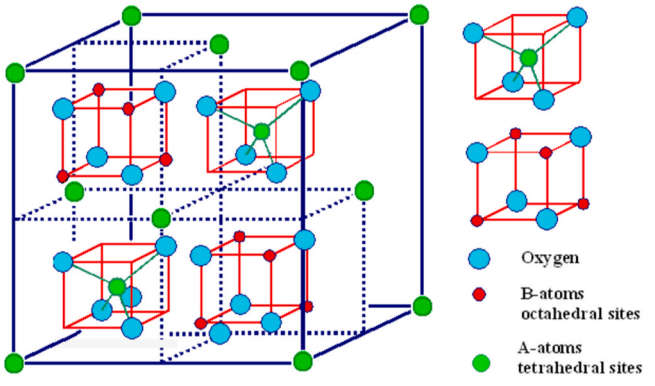

Fig. 4. Schematic illustration of the spinel structure of $CoFe_2O_4$, depicting the cation distribution: Fe^{3+} ions in tetrahedral sites (green), oxygen atoms (sky blue), and Fe^{3+}/Co^{2+} ions in octahedral sites (red). Reproduced from reference [125].

The utilization of TEM and high-resolution TEM (HR-TEM) analysis facilitates the acquisition of comprehensive information regarding the morphology of samples, in addition to their structural and textural properties. As demonstrated in the research by Sharma *et al.,* the TEM image obtained at two distinct annealing temperatures revealed the size and distribution of $CoFe_2O_4$ [128]. The particles were heavily agglomerated in both micrographs with a permanent magnetic moment equal to their volume. The estimated particle size for the samples annealed at 400 °C and 1000 °C was about 20 nm and 100 nm, respectively. This may be due to adjacent particles fusing due to surface melting. A similar increase in particle size has also been observed at higher annealing temperatures in previous literature.

5.2. Chemical and vibrational properties

Vibrational spectroscopy techniques, such as Fourier Transform Infrared (FT-IR) spectroscopy and Raman spectroscopy, are essential for characterizing the structural and chemical properties of spinel ferrites. These methods provide insights into the presence of functional groups, metal–oxygen bonding environments, and lattice dynamics.

Fourier transform infrared (FT–IR) was utilized to study the functional groups and composition changes throughout preparation [129–131]. M–O and M–OH functional groups are present in every spinel ferrite. Zinc ferrite (ZFO) samples have been observed to display surface-adsorbed OH group stretching and deformation vibrations at 3600–3300 cm^{-1} and 1650–1550 cm^{-1}[132,133]. The spectra showed three T_{2g} modes at 174, 480, and 543 cm^{-1}, along with E_g and A_{1g} modes at 287 and 686 cm^{-1}. Sharma *et al.* identified two fundamental absorption bands, indicative of a spinel-like structure [128]. The greater absorption peak at 550 cm^{-1} (ν_{tet}) is attributable to the tetrahedral metal ion and oxygen complex (M_{Td}-O) vibration mode, whereas the less intense peak observed at 420 cm^{-1} (ν_{oct}) is due to the stretching vibration of the complex.

Complementary to FT-IR, Raman spectroscopy offers detailed information about the short-range order and cation distribution in spinel lattices. Raman spectra of mixed spinel ferrite show that the transition metals modify the chemical structure and molecular interaction. Mund *et al.* acquired room-temperature Raman spectra for $Co_{1-x}Mg_xFe_2O_4$ (x = 0.0, 0.2, 0.4, 0.6, 0.8, and 1.0) in the 180–900 cm^{-1} frequency range [134]. In typical inverse spinel ferrite, half of the Fe^{3+} cations reside in tetrahedral sites and the rest in octahedral ones. Studying this structure could yield five optical active Raman modes, namely: A_{1g}, E_g, and 3 T_{2g}. Previous work on different ferrites has demonstrated higher-frequency Raman modes (A_{1g}) above 600 cm^{-1}, indicating local lattice effect within the tetrahedral sub-lattice, whereas lower frequency ones (E_g and T_{2g}) conform to the octahedral sub-lattice [127]. Together, FT-IR and Raman analyses play a critical role in confirming the formation of spinel phases and understanding their local bonding environments.

5.3. Surface physicochemical properties

X-ray photoelectron spectroscopy (XPS) provides critical insights into the surface chemistry of spinel ferrites, which is largely influenced by the distribution and valence states of transition metals. The surface chemistry of spinel ferrite is based on the transition metal in the structure of spinel ferrite in mixed spinel ferrite. For example, Fan *et al.* used XPS analysis to examine the $Zn_{0.8}Co_{0.2}Fe_2O_4$ sample [135]. The Zn 2p, Co 2p, and Fe 2p peaks' fine spectra were obtained. The Zn $2p_{3/2}$ peak's binding energy (BE) was 1021.3 eV, indicating the existence of Zn^{2+} species. The Co 2p region's XPS can be subdivided into four contributions. The BE values assigned to Co $2p_{3/2}$ and its shakeup satellite are approximately 780.8 and 785.8 eV, respectively, whereas the BE values assigned to Co $2p_{1/2}$ and its shakeup satellite are approximately 796.1 and 802.5 eV, respectively. The presence of the Co^{2+} species in the prepared sample has been indicated by the strong Co 2p shakeup satellites. The collected Fe $2p_{3/2}$ and Fe $2p_{1/2}$ spectra display two distinct main peaks with BE values around 710.5 and 724.2 eV, respectively, along with a satellite peak of Fe $2p_{3/2}$ visible at 718.7 eV, indicating the presence of the Fe^{3+} cations. These findings underscore the efficacy of XPS in delineating the chemical structure. Such information is essential for understanding the chemical stability, reactivity, and functional behavior, making XPS an indispensable tool for characterizing spinel ferrite surfaces.

5.4. Mössbauer properties

Mössbauer spectroscopy is a highly effective technique for analyzing the electronic and magnetic environments of iron-containing compounds, particularly in spinel ferrites. It provides detailed information on the valence state of iron, typically Fe^0 (metal), Fe^{2+}, and Fe^{3+}. In addition, the method is employed to ascertain the type of coordination polyhedron occupied by iron atoms (trigonal, tetrahedral, octahedral, etc.). Mössbauer spectroscopy is also utilized to assist in the identification of iron oxide phases based on their magnetic properties. In spinel structures, Mössbauer spectra often display multiple sextets corresponding to iron ions in distinct lattice sites. Fig. 5 shows the Mössbauer absorption spectrum of $MnFe_2O_4$ sample measured at room temperature [136]. The spectrum obtained was analyzed using two overlapping sextets, which were found to be consistent with the standard spinel crystal structure (A-ions in T_h positions and B-ions in O_h sites). At both the A- and B-sites, the quadrupole splitting (QS) value was zero, suggesting that symmetrical electric fields surround the Mössbauer nuclei, consistent with a well-ordered spinel configuration.

Mössbauer spectroscopy serves as a powerful, non-destructive technique for probing the oxidation states and local environments of iron atoms in spinel ferrites, especially when conventional methods like XRD are insufficient for poorly crystallized phases. Cabrera *et al.* reported Mössbauer spectra at 298 and 13 K in their manufactured Mg-ferrite samples to determine Fe atom oxidation and check the surrounding environment [137]. $MgFe_2O_4$ is donated as $[Mg_{1-c}Fe_c](Mg_cFe_{2-c})O_4$ (c is the inversion degree) and looks like inverted ferrite except for Mg and Fe atoms distributed between the spinel sites of the tetrahedral [A] and octahedral C, which is close to 0.9; however, it changes with the fabrication process and determines ferrite's physical properties and active site types. In $MgFe_2O_4$, Fe nuclei at (B) and [A] spinel locations feature similar average hyperfine magnetic fields, and therefore the zero-field Mössbauer spectroscopy shows an overlap of [A] and (B) sub-spectra, prohibiting c determination. Due to non-equilibrium sites and surface effects' unpredictable occupancy, nanostructured Mg–ferrite spectra investigation may be more difficult. All samples' room temperature spectra display a large central Fe^{3+} doublet (*Quadrupole Splitting* (ΔQ)

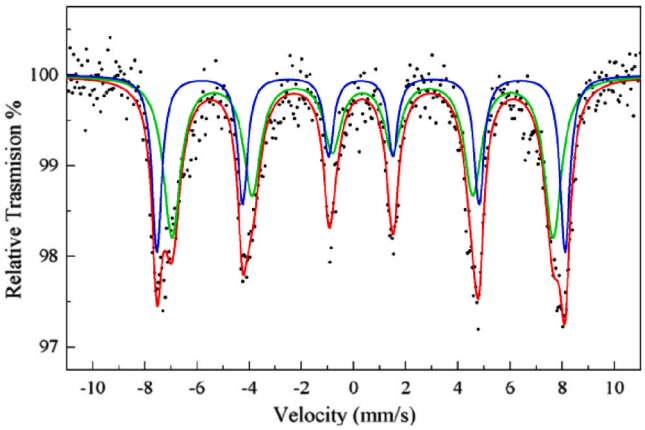

Fig. 5. Room-temperature Mössbauer absorption spectrum of $MnFe_2O_4$ sample. Adapted from [136] with copyright permission from Elsevier, 2010.

~0.655 mm/s and IS ~0.31 mm/s) and a broad magnetic signal. No Fe^{2+} signals were identified. The doublet to Fe ions of $MgFe_2O_4$ relax superparamagnetically within the (10^{-8} to 10^{-9}s) Mössbauer time window. Resolved magnetic signals account for blocked ferrite ferric ions. The thermal method increases the crystallinity, raising the magnetic signal's relative region from 10 % Magnesium Ferrite synthesized via Auto-Combustion and Thermal Treatment (MFOAT) to 37 % in auto-combustion samples. This means that MFOAT blocks more particle moments. The Magnesium Ferrite synthesized via Pechini Method (MFOP) room temperature-determined signal area is about 36 %. Spectra at 13 K show a proportionate increase in resolved magnetic signals at the expense of non-resolved signals, which occurs when thermal energy is inadequate to pass the anisotropy barrier in Fe-containing nanomagnetic materials, blocking some of the relaxed particle moments that relaxed SPM at 298 K at 13 K. Both cases show asymmetry and broadness in the lines, suggesting that Fe nuclei at spinel sites sense dispersed iron magnetic fields. Three six-line components were used in Recoil's "dynamic line form site study" to fit the spectra. These findings emphasize the sensitivity of Mössbauer spectroscopy in detecting the subtle structural and magnetic features of Mg–ferrite, especially in its nanostructured forms. Overall, Mössbauer spectroscopy plays a crucial role in confirming structural and magnetic ordering in ferrite materials.

5.5. Magnetic properties

Spinel ferrites exhibit remarkable magnetic properties, making them ideal for a variety of applications. Their magnetism arises from a ferrimagnetic ordering of spins in tetrahedral and octahedral lattice sites, where opposing magnetic moments of different strengths result in net magnetization. The magnetic properties of non-mixed spinel ferrite are higher than mixed spinel ferrite due to the contribution of dead magnetic materials such as transition metals. The magnetic properties of spinel ferrites are tuned by their unique crystal size [138,139]. The crystal structure of ionic oxides, particularly Fe oxides, enables a complex structure of magnetic ordering known as ferrimagnetism. The structural design of these ferrites allows for two distinct spins (up and down). Moreover, the total magnetic moment from all directions is not equal to zero [86]. Interestingly, the magnetic moments of atoms are opposed when compared to each other; however, the opposing moments are not balanced for various neighboring sublattices [88,89]. Ni-ferrite ($NiFe_2O_4$) is a ferrimagnetic soft ferrite with high saturation magnetization and low coercivity. Magnesium ferrite ($MgFe_2O_4$) is a soft magnetic material that has found application in a variety of fields [140–143]. In contrast, pure Co-ferrite ($CoFe_2O_4$) is known as a harder magnetic material, exhibiting high coercivity and significant magnetic anisotropy [122].

Tuning the magnetic properties can be achieved by mixing two or more metals in different ratios. *Verma et al.* reported the magnetic properties of Ni-Zn and Mn-Zn ferrites synthesized using the citrate precursor technique and the structure denoted by $Mn_{0.2}Ni_{0.8-x}Zn_xFe_2O_4$ where x = 0.4–0.6 [144]. The findings reveal that, at sintering temperatures below 1200 °C, the prepared mixed ferrites possessed relatively higher saturation magnetizations. Whereas Bhandare *et al.* employed a sol-gel auto-combustion route to prepare Mg-doped Co–Ni-mixed ferrite $Co_{0.5}Mg_xNi_{0.5-x}Fe_2O_4$ (x = 0–0.4), Wherein Ni and Mg occupied spinel structure octahedral (Oh) and tetrahedral (Td) sites, respectively [126]. While Co occupied both the Td and Oh regions by 2:3 ratios, the observations showed a slight decline in the saturation magnetization upon Mg substitution for Ni, whereas coercivity was not changed. In addition, the ferrimagnetic nature of the prepared structure was confirmed by both Fe-the Mössbauer spectroscopy and XRD results. Tailoring these properties through controlled metal substitution and processing conditions, such as sintering temperature or synthesis route, enables the development of ferrites with optimized performance for specific applications.

5.6. Stability properties

The thermal properties of the ferrite-based nanocomposite are considered one of the important characteristics of their application as photocatalysts. Thermogravimetric analysis (TGA) is a critical method for assessing the thermal stability of the prepared composites [145]. In general, all spinel ferrites, mixed and non-mixed, exhibit high thermal stability. Understanding these thermal decomposition patterns is essential for optimizing synthesis conditions and ensuring the structural integrity of the resulting ferrites during application. The decomposition process in all ferrites was divided into two stages [128]. Firstly, weight loss occurred in the 50–100 °C temperature range, which was attributed to water loss adsorbed from the sample. The decomposition of other components such as ethylene glycol and nitrate decomposition into CO_2 and NO_x, respectively, caused significant weight loss in the second stage in the 300–400 °C temperature range. The curve became almost featureless beyond 400 °C, suggesting the development of pure ferrite. Consequently, the optimal annealing temperature was determined to be 400 °C.

Sharma et al. synthesized Zn-incorporated Ni ferrite ($Zn_xNi_{1-x}Fe_2O_4$) (where x was from 0.0 to 1.0) for MB photocatalytic degradation [146]. The thermal decomposition and crystallization of the synthesized ferrite samples were recorded by TGA. TGA was obtained for both the as-prepared $Zn_{0.8}Ni_{0.2}Fe_2O_4$ and the annealed at 1000 °C sample in the 50–900 °C temperature range, with a 10 °C/min heating rate. The thermal decomposition method for the as-obtained sample entailed weight loss in three major steps. The initial weight loss in the 50–100°C range was attributed to the removal of adsorbed water from the investigated sample. The second major step, which occurred within the 300–400°C range, was initiated by the decomposition of nitrates and ethylene glycol, resulting in the formation of NOx and CO2, respectively. The third decomposition stage (which occurred at 550 °C) resulted in ferrite crystallization. Additionally, the absence of weight loss indicated the formation of ferrite. The 1000°C annealed sample exhibited an almost straight line, indicative of the formation of stable ferrite. These findings underscore the importance of thermal characterization in guiding the synthesis and functionalization of ferrites for efficient photocatalytic use.

5.7. Adsorption properties

Adsorbtion characteristics of spinel ferrite strongly depend on both surface chemical properties and the materials' microstructures [147,148]. The adsorption of spinel ferrite is a promising prospect, exhibiting a number of attractive characteristics, including a short duration, cost-effectiveness, high efficiencies, and ease of operation [149].

During the adsorption process, a substance (adsorbate) is redistributed from an aqueous solution to a solid surface (adsorbent) [150]. Many parameters influence adsorption efficiency, including adsorbent surface characteristics (surface area, size and number of pores, surface functional groups, thermal stability, and mechanical strength) [151], adsorbate concentration, pH, temperature, and contact time [150].

The adsorption process can take place via different mechanisms, including physical, chemical, and electrostatic interactions[152]. Electrostatic attraction occurs between the positively-charged surface of the adsorbent and negatively-charged anionic dyes [153]. Physical interactions, such as adsorption, occur by means weak intermolecular forces of attraction between adsorbates and adsorbents such as π–π electron donor–acceptor interactions, which often occur between a carbonaceous adsorbent's π-electrons and an adsorbate aromatic ring's π-electron, as initially suggested by Coughlin and Ezra (1968) [154]. Finally, in adsorbate–adsorbent chemical adsorption, strong covalent bond formation is the main factor [155]. One way to differentiate between physical and chemical adsorption is adsorption isotherms, especially Langmuir, Freundlich, Temkin, Dubinin-Radushkevich, and Redlich–Peterson isotherms [152,156].

Two other important adsorption characteristics are adsorption kinetics and thermodynamics. Kinetics is concerned with describing the retention rate of a solute from an aqueous solution to an interface (solid phase) at a given pH, temperature, adsorbent dose, and flow rate. Thermodynamics, in contrast, investigates adsorption feasibility, sustainability, and mechanisms, as summarized in Table 2 [157]. The porosity of the prepared nano-ferrites plays an important role in their adsorption capacities. A higher surface area means an optimized quantity and quality of active sites and thus better adsorption capacity. In addition, porosity provides efficient pathways and more active sites [133]. Ferrite nanomaterials not only exhibited promising adsorption capacities for dyes and ions but also potential gas adsorption applications.

5.8. Optical properties

The optical properties of ferrite nanoparticles can be evaluated using ultraviolet–visible (UV/Vis) absorption, photoluminescence (PL), and electrochemiluminescence (ECL). Various spinel ferrites possess outstanding optical characteristics, including parasitic light absorption [162] and luminescence [163], which are employed in magneto–optical recording devices [164] and lasers [165]. Optical studies of spinel ferrite may be influenced by many parameters, including the rejoins of M^{2+} and Fe^{3+} ions, crystal size, and the type of doping metals as summarized in Table 3 [118]. These parameters affect charge carrier dynamics and light–matter interactions within the material, making optical characterization a key tool in understanding and tuning ferrite nanoparticles for specific applications.

Photoluminescence (PL) studies are important for the measuring, migration, and recombination of light-generated charge carriers in material. Renuka *et al.* used both sol-gel and combustion methods to prepare $NiFe_2O_4$ NPs [175]. PL analysis showed that Ni^{2+} ions were present in the octahedral site and Fe^{3+} ions in tetrahedral sites, leading to a mixed spinel structure. In addition, at 413, 426, and 513 nm, PL signatures were observed for samples prepared by combustion and sol-gel methods without any peak shift. The presence of Ni^{2+} ions in octahedral sites was assured by the 413 nm-located peak with a $^3A_2$ (^3F) → $^3T_1$ (^3P) transition. 426 and 513 nm bands were attributed to Fe^{3+} ions' transitions of $^3d_5$ → $^3d_4$ 4 s upon electron excitation to the conduction band (CB) as shown in Fig. 6. Hammad *et al.* illustrated the influential behavior of Co^{2+} ions on the optical properties of $CuFe_2O_4$ NPs synthesized by a precipitation method [176]. Their results revealed that upon doping Co^{2+} ions, the luminescence intensity of the $CuFe_2O_4$ sample increased. This can be attributed to the distance increment between the dopant and the array [177]. In summary, spinel ferrite nanoparticles demonstrate remarkable optical characteristics which are crucial for various advanced technological applications. Employing PL and UV/Vis techniques can show how ion distribution and doping significantly affect light absorption and emission behavior.

5.9. Electrochemical and photoelectrochemical properties

Spinel ferrite-based magnetic nanomaterials have emerged as versatile and efficient electrocatalysts for a variety of key electrochemical reactions such as the oxygen reduction reaction (ORR), and hydrogen evolution reaction (HER). These reactions are crucial to energy conversion and storage technologies, particularly in fuel cells and water-splitting systems. The photocatalytic reduction and oxidation reactions on the surface of ferrites-based magnetic nanoparticles are electrocatalytic ones driven by the photogenerated electron and holes, respectively. More interestingly, mixed metal spinel ferrite can also serve as multifunctional electrocatalysts with higher activity than non-mixed spinel ferrite [172], which plays an important role in the improved photocatalytic activity. Das *et al.* studied the electrochemical properties of cathodes supported by $Co_{0.5}Zn_{0.5}Fe_2O_4$, $CoFe_2O_4$, $ZnFe_2O_4$, and Pt/C synthesized materials [178]. The photoelectrochemical behaviour of ferrites, which is facilitated by their semiconductor nature, has garnered significant interest. Many electrochemical parameters such as exchange current density, charge transfer resistance, and electroactive surface can directly affect the performance of ferrite-based photocatalysts. These properties have been elucidated by analytical techniques such as cyclic voltammetry (CV), electrochemical impedance spectroscopy (EIS), and Mott-Schottky (MS) analysis. Recent advances highlight the potential of ferrite nanomaterials as inexpensive, abundant alternatives to precious metals like platinum in sustainable energy technologies.

The ORR kinetics these cathodes were studied in an O_2-saturated 100 mM phosphate buffer saline (PBS) solution, as the electrolyte using CV. The current response (Fig. 7) shows a sharp ORR current peak for the cathode using $Co_{0.5}Zn_{0.5}Fe_2O_4$ at - 0.69 V with a 45 mA peak current, which was considerably higher than the $CoFe_2O_4$ ORR current peak (3.2 mA) and that of $ZnFe_2O_4$ (6.5 mA), indicating superior catalytic activity of $Co_{0.5}$ $Zn_{0.5}Fe_2O_4$. EIS assessed the charge transport cathode performance and the exchange current densities using prepared $Co_{0.5}Zn_{0.5}Fe_2O_4$. The EIS spectra were simulated in an equivalent circuit in the form of a typical Nyquist plot to obtain the solution resistance (R_s) and to obtain R_{ct}. Fig. 7 shows the virtual Nyquist graphs. The R_s value for all the cathodes was determined to be about 1.22 Ω, which is understandable given the related 100 mM PBS electrolyte used in the study. The R_{ct} value of 0.18 Ω for the $Co_{0.5}Zn_{0.5}Fe_2O_4$ cathode was observed to be 1.33-fold lower than the Pt/C cathode (0.24 Ω), five times less than $CoFe_2O_4$ (0.9 Ω), and three times less than $ZnFe_2O_4$ (0.5 Ω), indicating greater ORR operation. Furthermore, the $Co_{0.5}Zn_{0.5}Fe_2O_4$-based cathode could achieve a 3.26 A/m^2 exchange current density, which is higher than the Pt/C cathode (2.44 A/m^2). The electrochemical tests revealed that $Co_{0.5}Zn_{0.5}Fe_2O_4$ is a good ORR catalyst with low overpotential losses.

Electrochemical water splitting necessitates the utilization of catalysts that exhibit both robust electrocatalytic activity and durability, thereby accelerating the sluggish kinetics inherent to the process [179].

Table 2
Key adsorption parameters of ferrite nanomaterials in recent studies.

System	Preparation method	Adsorbed dye/ions	Surface area (m^2/g)	Pore volume (cm^3/g)	Adsorption isotherm	Adsorption kinetics	Adsorption capacity	Ref.
$MnFe_2O_4$ and $CoFe_2O_4$	Co-precipitation	Zn (II)	84.5 and 50.4	0.2769 and 0.1846	Langmuir model (higher R^2)	Pseudo-second-order	454.5 and 384.6 mg g^{-1} at pH = 6	[157]
Mixed$CaFe_2O_4$ and $MnFe_2O_4$	Co-precipitation	Methyl orange (MO)	47.67	0.121	Langmuir model	Second-order	99.88 % after 24 min	[158]
$CuFe_2O_4$ / Kaoline	Co-precipitation	Methylene blue (MB) and methyl violet (MV)	174.78	0.256	Freundlich model	Quasi-second-order	98.64 % and 99.25 % at pH = 8 and 25°C after 30 min	[159]
$NiFe_2O_4$-GO	Solvothermal	MB	88.027	0.131	Langmuir model	Pseudo-second-order	1.4 mg g^{-1} after 240 min	[160]
$ZnFe_2O_4$/MgAl-LDH	Hydrothermal	Congo Red (CR)	0.015	0.257 mL g^{-1}	Langmuir-type monolayer adsorption	Pseudo-second-order	294.12 mg g^{-1} with Mg/Al molar of 2	[161]

Table 3
Optical properties of spinel ferrites: influence of composition, doping, and synthesis method.

Spinel system	System type	Preparation method	Doping metal	Absorbance profile	Bandgap (E_g)	Ref.
$CoFe_2O_4$	Non-mixed spinel ferrite	Coprecipitation method	-	Blue shift with particle size reduction	2.44 eV	[166]
$NiFe_2O_4$	Non-mixed spinel ferrite	Coprecipitation method	-	Blue shift with particle size reduction	3.54 eV	[166]
$ZnFe_2O_4$	Non-mixed spinel ferrite	Coprecipitation method	-	Blue shift with particle size reduction	3.25 eV	[166]
$CuFe_2O_4$	Non-mixed spinel ferrite	Sol-gel method	-	Strong visible light absorption	2.22 eV	[167]
$MnFe_2O_4$	Non-mixed spinel ferrite	Hydrothermal method	-	Strong visible light absorption	0.98 eV	[168]
$MgFe_2O_4$	Non-mixed spinel ferrite	Solvothermal method	-	UV–visible region broad absorption	1.82 eV	[169]
$Co_{1x}Zn_xFe_2O_4$ (x = 0, 0.3, 0.5, 0.7, and 1)	Two-metal mixed spinel ferrite	Co-precipitation method	Zn	Shift toward higher wavelength with increasing (Zn) concentration	E_g decreased to 2.258 eV from 2.8306 eV with Zn content increase	[170]
$Co_{1x}Ni_xFe_2O_4$ ($0 \leq x \leq 1$, with 0.25 steps)	Two-metal mixed spinel ferrite	Precipitation method	Ni	Blueshift was observed with (Ni) increase	By (Ni) increase, E_g got broadened	[171]
$Cu_{0.5}Zn_{0.5x}Ba_xFe_2O_4$ [x = 0.05, 0.1]	Three-metal mixed spinel ferrite	Solid state route	Ba^{2+}	Absorption in the visible region	E_g increased when Ba^{+2} increased	[172]
$Mn_{0.5}Zn_{0.5-x}Mg_xFe_2O_4$ NPs (x = 0, 0.125, 0.25, 0.375, and 0.5)	Three-metal mixed spinel ferrite	Sol-gel method	Mg^{2+}	200–800 nm reflection band was observed	By increasing Mg^{+2}, E_g decreased	[173]
$Ni_{1-x}Cu_xFe_2O_4$ ($0 \leq x \leq 0.9$)	Two-metal mixed spinel ferrite	Mechanochemical technique	Cu	The blue shift was detected by increasing Cu cations	Upon increasing Cu cations, E_g decreased	[174]

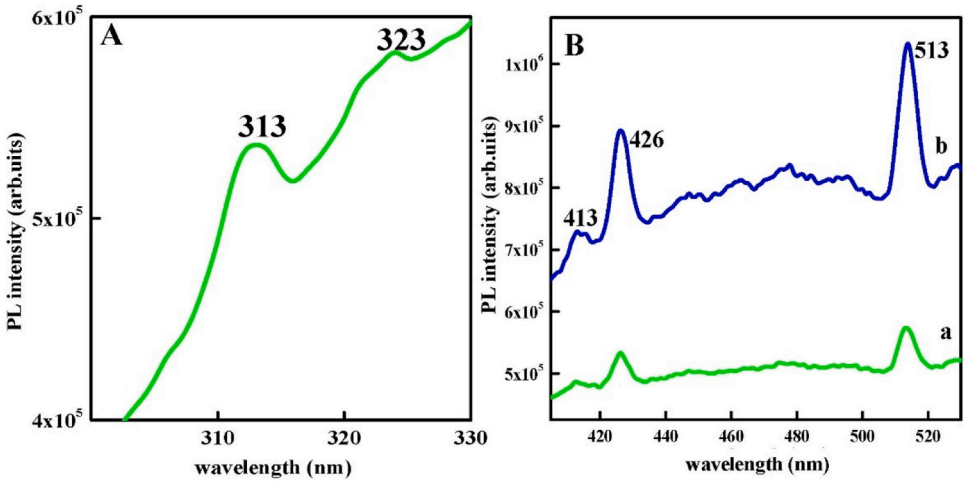

Fig. 6. (A) excitation spectrum of the prepared $NiFe_2O_4$ NP; (B) Emission spectra of $NiFe_2O_4$ samples synthesized via (a) combustion method and (b) sol-gel method. Adapted from [175], with copyright permission from Elsevier, 2021.

In contrast to the majority of Pt-free electrocatalysts, the most well-known heterogeneous Pt/C composite has been demonstrated to be the most efficient HER electrocatalyst due to its high-exchange current density at low overpotentials, chemical inertness, versatility, high conductivity, and oxidation resistance [180]. Nevertheless, the practical applications of Pt were significantly limited by its high cost and low abundance. An alternative to Pt is represented by earth-abundant transition metals, which have been found to be inexpensive and effective electrocatalysts. These metals include Fe, Co, Ni, Mo, and W. In this context, due to their abundance on earth, customizable molecule architectures, and the special benefits of readily producing a variety of nanostructures, mixed and non-mixed spinel ferrites have also shown tremendous potential as attractive HER electrocatalysts for water-splitting reactions. In recent years, ferrite oxides, including Fe-spinel oxides and Fe_3O_4, along with ferrites such as AFe_3O_4 (A = Mn, Co, Zn, Ni), have emerged as promising anode candidates for electrocatalysts [181]. *Nivetha et al.* cited electrochemical studies on synthesized graphene-$MnFe_2O_4$ (MFG) and graphene-$ZnFe_2O_4$ (ZFG) materials [182]. A comprehensive understanding of catalytic efficiency within an acid medium necessitates electrochemical surface area tests to investigate the double-layer capacitance (C_{dl}), and electroactive surface areas could be obtained in the non-faradaic zone. The CV technique was used to achieve this objective, with varying scan rates ranging from 0.002 to 0.1 Vs^{-1}. The estimation of electroactive site numbers can be achieved through the calculation of the active surface area, derived from electrochemical analysis, which is one of the most critical measurements in the estimation of turnover frequency (TOF).

Mott-Schottky (MS) studies on AFe_2O_4 ferrospinels (where A = Co, Cu, Zn) were published by Helaili *et al.* [183]. The semiconductor (SCs)-electrolyte junction's capacitance (C) and its change with an external bias voltage were calculated at 1 kHz. The MS plot intercept was used to calculate the flat band voltage (V_{fb}) potential (Fig. 8) and the

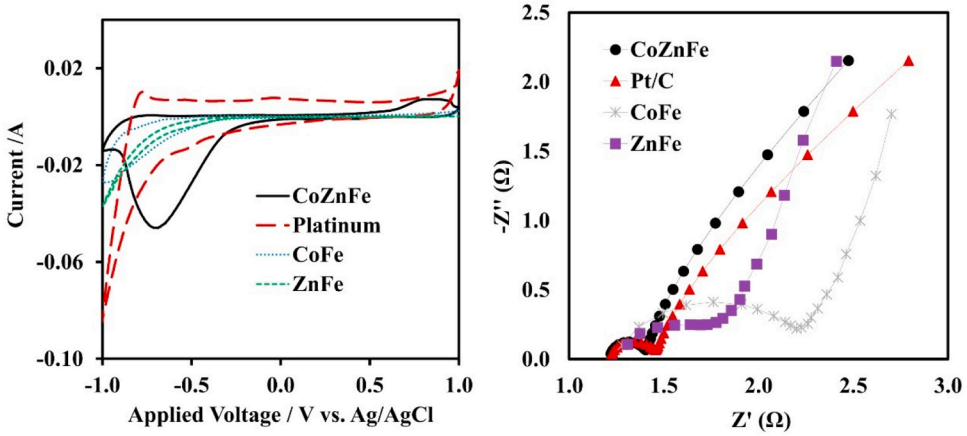

Fig. 7. (a) CV curves; and (b) Nyquist plots of $Co_{0.5}Zn_{0.5}Fe_2O_4$, $CoFe_2O_4$, $ZnFe_2O_4$, and Pt/C catalyzed cathodes. Adapted from [178] with copyright permission from Elsevier, 2018.

donor density (ND) was determined by its slope. The MS plot slope, where the +ve sign refers to the n-type and the -ve sign refers to the p-type, also confirms the semiconductor type. The MS relation (Eq. 1) was applied to estimate the density ND and potential V_{fb} at the SCs/electrolyte interface [183]:

$$\frac{1}{c^2} = \frac{2}{\varepsilon\varepsilon_0 eN_D}\left(V - V_{fb} - \frac{kT}{e}\right) \quad (1)$$

where C, ε, ε_0, k and N_D represent the capacitance of the space charge region, the permittivity of the vacuum, the dielectric constant of the semiconductor, the Boltzmann constant, and the donor density (hole acceptor quantity for the p-type SC or electron donor quantity for the n-type SC), respectively. The electron density (N_D) was calculated for the three spinels using the slope; the +ve value approves the n-type character. The flat band voltage (V_{fb}) was nearly identical to the onset potential (V_{on}), meaning the gap area was devoid of surface states. Upon contact between SC and the electrolyte, the space-charge width (W) arises. In the space charge field, the transition to equilibrium with the redox couple created a Schottky barrier. From the following relationship (Eq. 2), the W amount of semiconductor oxides was determined for a band bending ($\Delta V = 0.5$ V) [183]:

$$W = \sqrt{\frac{\varepsilon\varepsilon_0(V - V_{fb})}{eN_D}} \quad (2)$$

The low photocurrent of a photocatalyst was attributed to the low

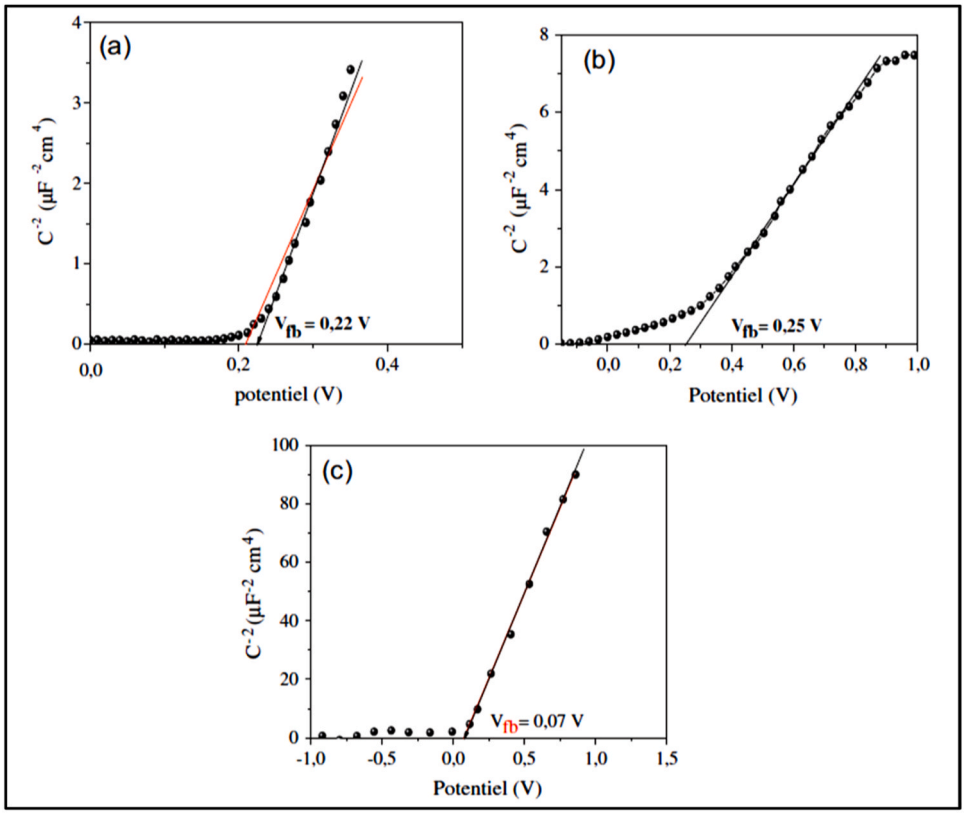

Fig. 8. (a) MS plots of $CoFe_2O_4$; (b) $CuFe_2O_4$; and (c) $ZnFe_2O_4$ electrodes. Measurements were conducted in 0.5 mol/L NaOH electrolyte under a nitrogen atmosphere at a scan rate of 0.01 V/s. Adapted from [183] with copyright permission from Elsevier, 2015.

electrical transport properties, which resulted in low conductivities and a small photo response. Furthermore, short charge carrier diffusion lengths were often recorded. As a result, before approaching the SCs/electrolyte interface, the majority of the produced holes could recombine with the existent electrons (present at the CB. The small particles helped the SCs/electrolyte interface move closer to the hole photogeneration, resulting in improved performance collecting holes. Smaller particles, in contrast, increase the depletion-to-diffusion ratio. Because of the low-density N_D calculated W increased from 2.84 nm for $CuFe_2O_4$ to 2760.58 nm for $ZnFe_2O_4$.

Due to their superior thermal and chemical stability as well as their optimal electronic band structure, spinel ferrite-based magnetic nanoparticles have also shown promise as photoelectrode candidates for solar energy conversion in photoelectrochemical (PEC) cells, in addition to their direct use as electrocatalysts. Ferrite-based nanomaterials for photoelectrocatalytic applications are typically synthesized using the same diverse techniques detailed in Section 4, such as co-precipitation, hydrothermal, and sol-gel methods, which allow for control over size, morphology, and crystallinity crucial for photoelectrode performance. For instance, Singh et al. demonstrated the photoelectrochemical properties of a $CoFe_2O_4$ nanostructure film [184]. A three-electrode cell assembly was used for the photoelectrochemical tests, with the photoanode being a $CoFe_2O_4$ nanostructure film coated onto a fluoride tin oxide (FTO) substrate, the counter, and reference electrodes being a Pt-wire and Ag/AgCl, respectively, and the electrolyte being 0.1 M Na_2S solution (Fig. 9**a**). A tungsten halogen lamp with a ~100 mW/cm^2 illumination rate was applied as the source of photons. To research the effect of an external magnetic field on the $CoFe_2O_4$ film photoanodic behavior, a permanent magnet assembly was used to apply a magnetic field parallel to the film plane. The J-V properties of the $CoFe_2O_4$ photoanode with and without a light source, as well as $CoFe_2O_4$ photoanode J-V curves in light conditions in the presence of various strengths of magnetic fields, are shown in Fig. 9**b**. The J-V curves in $CoFe_2O_4$ film reveal a ~1.55 mA/cm^2 significant photocurrent (at 1.9 V vs. RHE) in the absence of a magnetic field. However, on subjecting the $CoFe_2O_4$ film to an external magnetic field of 400 Oe, the current increased to ~2.14 mA/ cm^2. When the magnetic field strength was increased to 600 Oe, the maximum increase in photocurrent was ~3.47 mA/cm^2. No major change in the photocurrent may be inspected as the magnetic field was increased further. The detected magnetic field-induced shift in the photocurrent correlates to a ~123 % increase in the photocurrent, which is significantly higher than previously reported studies on the magnetic field effect on photocurrents and other photocurrent effects. As magnetic fields vary in frequency, the $CoFe_2O_4$ nanostructure films chronoamperometry findings at a 1.23 V fixed potential (vs. RHE) are shown in Fig. 9**c**. The photocurrent enhancement with magnetic fields follows the same pattern as the chronoamperometry findings. The chemical stability of the $CoFe_2O_4$ nanostructure photoanode is also strong.

The combined effects of photocatalysis and electrocatalysis are thought to be responsible for the remarkable increase in activity, which can be attributed to the boosted activity of electrocatalytic (EC) oxidation, improved charge separation, and increased reactive radical species, such as OH and O_2^-. Thus, it is expected that spinel ferrite-based magnetic films will soon be widely used in an increasing number of PEC fields. Their activity should also be further improved through better balancing electronic structures (such as band-gap and redox ability), stability, change–carrier mobility, and active sites. In summary, the integration of spinel ferrites into electrocatalytic and photoelectrochemical systems represents a promising avenue for advancing renewable energy technologies through sustainable material solutions.

5.10. Density functional theory for electronic and catalytic property tailoring

Density Functional Theory (DFT) has played a vital role in

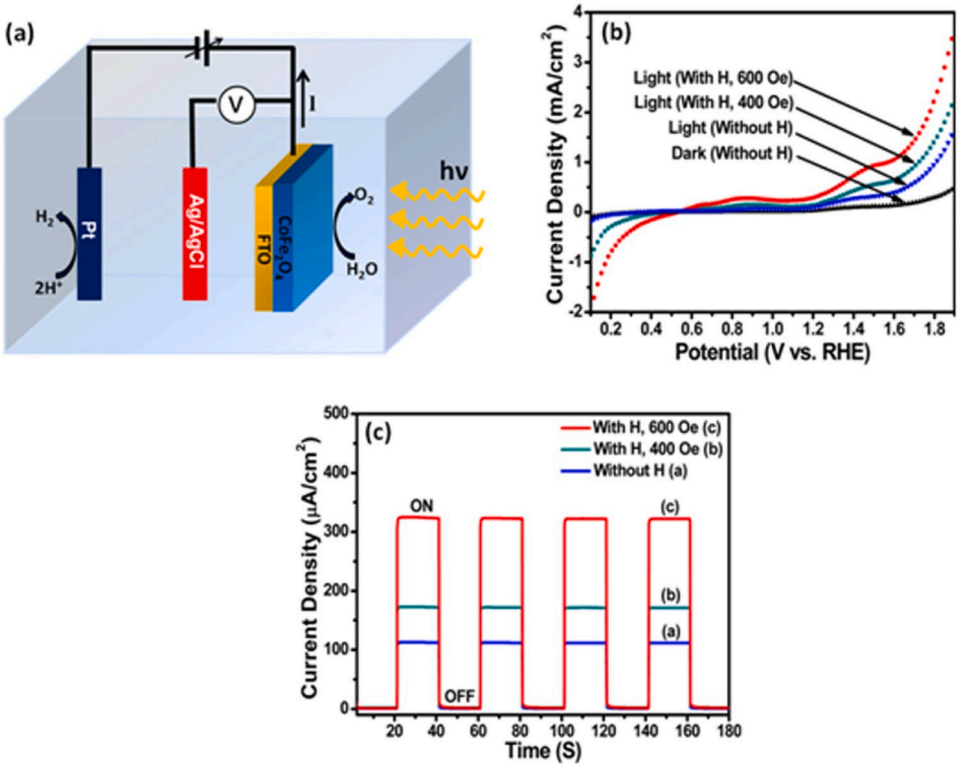

Fig. 9. (a) Schematic illustration of a three-electrode cell configuration for photoelectrochemical performance measurements; (b) Current density-potential (*J-V*) curves of a $CoFe_2O_4$ photoanode under dark conditions, and light illumination (100 mW/cm^2) with and without an external magnetic field; (c) Chronoamperometry results demonstrating the photoresponse of a $CoFe_2O_4$ nanostructure film under varying magnetic field strengths. Reproduced from reference [184].

understanding and predicting the electronic properties and bandgap tuning of ferrite-based nanomaterials, particularly in the context of photocatalysis and CO_2 reduction. These theoretical calculations offer atomic-level insight into band structure, density of states (DOS), charge distribution, and magnetic interactions, which are all critical for photocatalytic activity. DFT has been extensively used to predict and tune bandgaps of ferrite nanomaterials, which are typically narrow (~1.8–2.2 eV). This enables visible-light absorption, a desirable trait for photocatalytic CO_2 reduction [185–188]

Salcedo-Rodríguez *et al.* used DFT to examine the (001) surface terminations of $ZnFe_2O_4$ compound [189]. They observed that zinc-terminated surfaces are most stable, and that cationic inversion (Zn–Fe antistites) emerges as a surface defect. This, in turn, promotes ferrimagnetic behavior and modifying electronic structure. However, Fritsch and Ederer explored how epitaxial strain influences cation distribution, electronic structure, and magneto crystalline anisotropy in $CoFe_2O_4$ and $NiFe_2O_4$. Their DFT results demonstrated strain-dependent tuning of electronic and magnetic properties, which is useful for engineering band alignments [190]. Another study investigated the properties of Al-doped $NiFe_2O_4$, utilizing both sol-gel and DFT methods. The doping process has been shown to modify surface electronic states and adsorption properties, thereby enhancing CO_2 capture. This represents a significant step towards photocatalytic CO_2 reduction [191]. Recently, DFT has become a cornerstone in elucidating reaction mechanisms for electrochemical CO_2 reduction, particularly in identifying intermediates and pathways of photocatalytic CO_2 reduction on metal oxide and ferrite surfaces. These studies aim to model the sequential proton-coupled electron transfer steps by calculating the Gibbs free energies associated with reaction intermediates such as $*CO_2$, *COOH, *CO, *CHOH, and $*CH_4$ [192]

As CO_2 reduction mechanisms often involve multiple intermediates and complex reaction pathways, DFT has become essential in identifying energetically favorable routes and predicting key reaction steps at the molecular level. Liu *et al.* investigated carbon monoxide (CO) oxidation over the surface of $MnFe_2O_4$ during chemical looping combustion [193]. Thanks to its distinctive properties such as good thermal stability and cost-effectiveness, $MnFe_2O_4$ is a promising oxygen carrier. DFT results revealed that the octahedral Fe^{3+} site was preferred for CO chemisorption with a C-down orientation, as is shown in Fig. 10. In addition, CO oxidation on the $MnFe_2O_4$ surface took place in three steps, including CO adsorption, diffusion, and CO_2 desorption. Specifically, some active O sites were occupied by the Mn atomic layer present on the top of the Mn-terminated surface, which led to a weakening of surface activity. Then, in order to generate a CO_2 complex, adsorbed CO reacts with a bridging surface O. CO_2 desorption finally occurs by overlapping an energy barrier.

5.11. Properties engineering for efficient photocatalytic reduction of CO_2

For effective photocatalytic reduction of CO_2 using magnetic photocatalysts, several key material properties could be precisely engineered. First and foremost, bandgap tuning is critical to enable visible-light absorption and align the conduction band potential to match the reduction potentials of CO_2 to value-added products such as CO, CH_4, and CH_3OH [194–196]. Tailoring the bandgap could help in reducing electron-hole recombination rates. Secondly, efficient charge separation and transport could be achieved through strategies such as heterojunction formation, Z-scheme architecture, and co-catalyst loading [197]. This facilitates the migration of photogenerated electrons to surface-active sites before recombination occurs. The presence of oxygen vacancies could introduce mid-gap states and serve as active adsorption and activation sites for CO_2 molecules. Furthermore, the magnetic separability (intrinsic to ferrites) offers a significant practical advantage, facilitating facile recovery and reuse of photocatalysts in continuous operation setups [198]. Finally, properties such as surface area, porosity, crystallinity, and defect density synergistically influence CO_2 capture, light harvesting, and active site availability. A comprehensive understanding of how these properties interplay in ferrite systems provides a rational basis for designing next-generation magnetic nanomaterials tailored for highly efficient and sustainable photocatalytic CO_2 reduction.

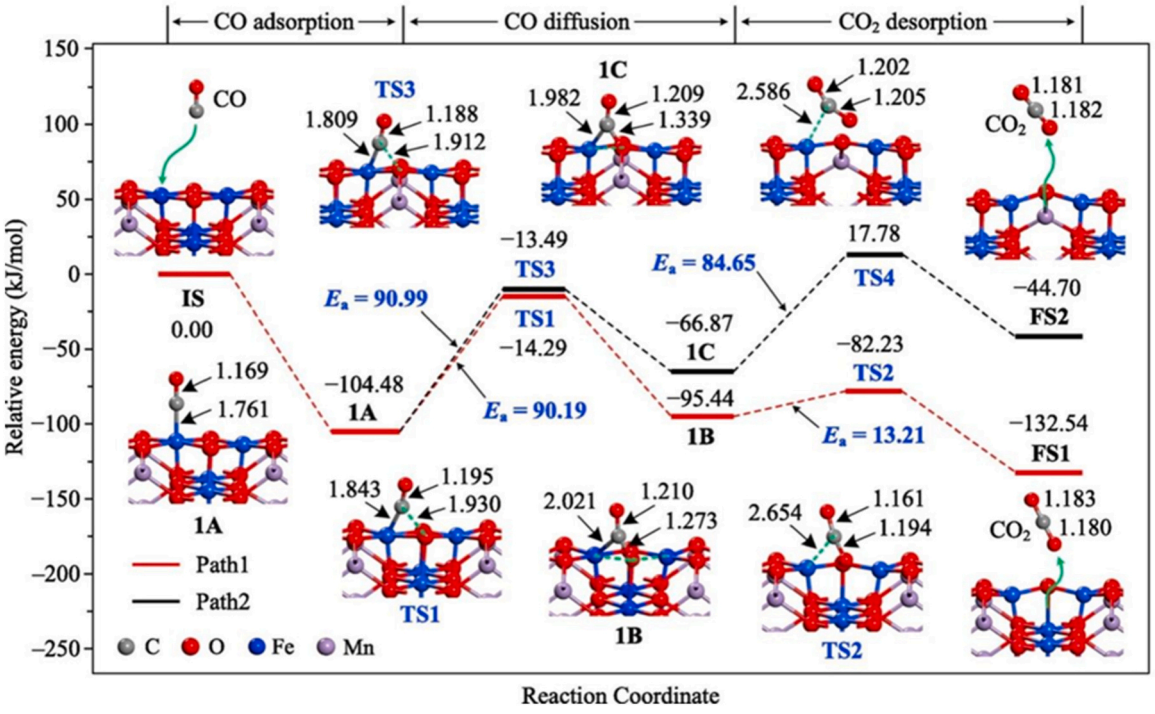

Fig. 10. CO oxidation energy profiles and reaction pathways over Fe-terminated surface. The bond lengths are indicated in Å. Adapted from [193] with copyright permission from Elsevier, 2018.

6. Photocatalytic reduction of carbon dioxide

This section provides a comprehensive overview of the photocatalytic reduction of CO_2, with a specific focus on the application and enhancement strategies of Spinel Ferrite-Based Magnetic Photocatalysts (SFMPs). It first establishes the global context and fundamental principles of photocatalytic reduction of CO_2, followed by an in-depth discussion of SFMPs' unique properties and their general catalytic mechanism. Subsequently, various advanced strategies employed to enhance the efficiency and selectivity of SFMPs for CO_2 conversion are detailed, supported by specific research examples.

6.1. Global context and fundamental principles of photocatalytic CO_2 reduction

The escalating global atmospheric CO_2 levels are significantly intensifying the greenhouse effect, leading to severe environmental challenges and exacerbating the depletion of fossil fuel resources. Addressing these interconnected global challenges necessitates the urgent development of sustainable energy solutions. In this context, the photocatalytic reduction of CO_2 into valuable energy-bearing compounds such as CO, methane, and methanol) (Fig. 11). Inoue *et al.* initially demonstrated the photocatalytic reduction of CO_2 in 1979 [199] to hydrocarbons as an ecofriendly method for CO_2 conversion. The utilization of solar light as an illumination source in photoreduction reactions is a significant development due to the inherent advantages of solar energy, including its clean nature, perpetual availability, and cost-free status. The reduction of CO2 in various products is contingent upon the density of photoinduced electrons [200,201] (Table 4). The reaction starts with activating the bonds on both sides of O═C═O with photogenerated e^- and then the reaction proceeds according to the number of available electrons and the redox potential of each product. Product type (selectivity) and yield could be controlled by engineering a suitable photocatalyst. Semiconductors are known to provide good photocatalytic activity, as some of the photoexcited electrons in the conduction band undergo redox reactions while others recombine. Therefore, we must design an effective photocatalyst for CO_2 reduction with a minimum recombination rate, the highest activity, and lowest cost. Semiconductors with wide band gaps (<3 ev) like TiO_2, SiC, and ZnS are not active under solar irradiation. On the other hand, iron oxides are solar-activated photocatalysts with a narrow band gap, but their conduction band is more positive than the redox potential of CO_2 [202]. Mixing different semiconductors with iron oxides creates photocatalysts that have the advantages of both types. The conduction band potential of the photocatalyst must be lower than the reduction potential of the reaction to occur [203]. Spinel ferrites are also known for their magnetic properties, which facilitate their recovery and reusability. Nano-catalysis is preferred rather than bulk catalysis, as it provides a larger surface area, improved light harvesting, more active sites, and enhanced adsorption of CO_2. The three-step mechanism of illumination→ charge activation→ catalyzed reaction is involved in CO_2 conversion [204].

Table 4
Equilibrium potentials for CO_2 reduction products and the corresponding density of activated electrons [201].

$CO_2 + 2\,H^+ + 2\,e^- \rightarrow CO + H_2O$	$E^0 = -0.52$ V
$CO_2 + 2\,H^+ + 2\,e^- \rightarrow HCOOH$	$E^0 = -0.61$ V
$CO_2 + 4\,H^+ + 4\,e^- \rightarrow HCHO + H_2O$	$E^0 = -0.48$ V
$CO_2 + 6\,H^+ + 6\,e^- \rightarrow CH_3OH + H_2O$	$E^0 = -0.38$ V
$CO_2 + 8\,H^+ + 8\,e^- \rightarrow CH_4 + 2\,H_2O$	$E^0 = -0.24$ V
$CO_2 + e^- \rightarrow CO_2^{\bullet}$	$E^0 = -1.90$ V

The activation of inert CO_2 molecules requires a considerable amount of energy. Generally, CO_2 hydrogenation into C^{2+} hydrocarbons goes through two consecutive reaction steps: firstly, a reduction of CO_2 to CO via the reverse water–gas shift (RWGS), $CO_2 + H_2 \rightarrow CO + H_2O$, followed by the hydrogenation of CO to C^{2+} hydrocarbons via Fischer–Tropsch synthesis (FTS, $n\,CO + 2n\,H_2 \rightarrow C_nH_{2n} + nH_2O$) using traditional FTS catalysts (e.g., Fe, Co, Ni and Ru). However, the product follows the Anderson–Schulz–Flory (ASF) distribution, which is mainly straight-chain paraffins. Promoters (e.g., sodium, kalium, manganese, etc.) are added to FTS catalysts to improve the selectivity towards light olefin products by promoting the dissociation and adsorption of CO and enhancing surface basicity [205].

A photoelectron participating in the reduction of CO_2 into products has been reported in some studies. The photocatalytic activity of various photocatalysts was compared by a measurement standard: the total utilized photoelectron number (UPN) [206–209], calculated by the Eq. 3:

$$N_{UPN} = 2\,N_{H2} + 2\,N_{CO} + 8\,N_{CH4} \quad (3)$$

where (N) represents the molar number of generated products. Not all studies that are discussed in this section paid attention to that important factor (UPN), although it identifies the photocatalytic activity of the catalyst under investigation.

The selectivity of the reduction products depends on the density of activated charges and the reaction medium. The photocatalytic CO_2 reduction can operate in vaporous or aqueous media [210], each one of which pushes the reaction to a specific pathway (Fig. 11).

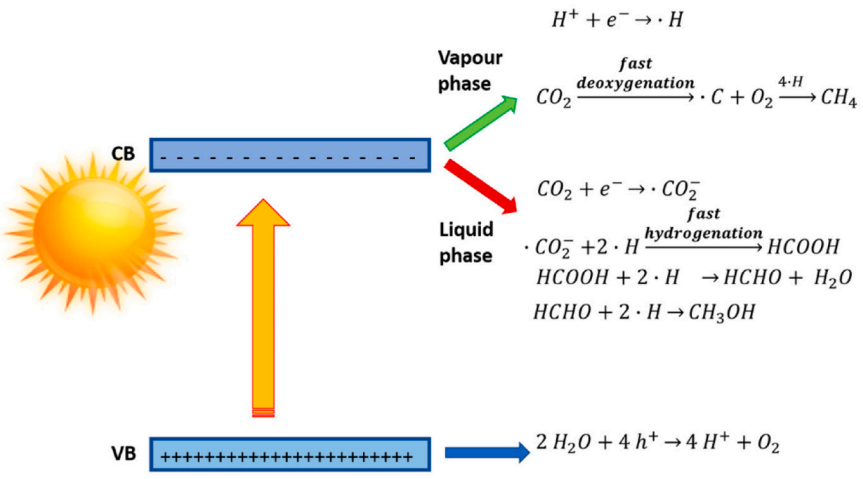

Fig. 11. Possible pathways of photocatalytic CO_2 reduction in vapor and aqueous media. Adapted from [210] with copyright permission from MDPI, 2017.

6.2. SFMPs: properties and general mechanism

A deeper understanding of the photocatalytic reduction mechanism of CO_2 over SFMPs is imperative for guiding future design strategies. When exposed to light, SFMPs absorb visible photons, which could generate electron-hole pairs. The photogenerated electrons in the CB migrate to the surface and could participate in the multi-electron reduction of adsorbed CO_2 molecules while holes in the valence band (VB) could react with water or other sacrificial agents. The reduction pathway typically involves key intermediates including CO_2^-, COOH, and $HCOO^-$, with subsequent formation of products like CO, HCHO, CH_3OH, and CH_4. The outcome is contingent on the number of electrons transferred and the redox potentials of the reaction steps. The efficiency and selectivity of these pathways are closely tied to catalyst properties like band gap, surface adsorption energy, and charge separation efficiency. All of these properties can be tuned by means of structural modifications [211]. Upon light irradiation, these photocatalysts (e.g., $ZnFe_2O_4$, $CuFe_2O_4$, $MnFe_2O_4$) generate electron-hole pairs, where the excited electrons reducing CO_2 into valuable hydrocarbons or solid carbon, while holes often oxidize water or sacrificial donors. The mechanistic pathway of photocatalytic CO_2 reduction on SFMPs, can be simplified as follows:

$$CO_2 + e^- \rightarrow CO_2^{\bullet -} \quad (4)$$

$$CO_2^{\bullet -} + H^+ \rightarrow COOH^* \text{ or } HCOO^* \quad (5)$$

$$COOH^* \rightarrow CO + OH^- \quad (6)$$

$$HCOO^* \rightarrow HCHO \rightarrow CH_3OH \rightarrow CH_4 \quad (7)$$

The overall efficiency and selectivity of these pathways are critically linked to intrinsic catalyst properties, including band gap, surface adsorption energy, and charge separation efficiency. Metal doping, for instance with Ce or Mn, introduces mid-gap states and oxygen vacancies, enhancing visible-light absorption and facilitating CO_2 activation and conversion via intermediate species like COOH* and HCOO* [212]. Heterojunction and Z-scheme architectures (e.g., $CuFe_2O_4/TiO_2$, $ZnFe_2O_4/Ag/TiO_2$) could promote directional charge separation, allowing more electrons to participate in CO_2 reduction and suppressing recombination, thus improving the yield of CH_3OH or CH_4 [213]. Furthermore, vacancy engineering (e.g., in $MgFe_2O_4$ or Co-Fe_2O_3) increases the density of oxygen vacancies, which serve as CO_2 adsorption and activation sites, thereby stabilizing COOH* intermediates and enhancing CO or H_2 production [214].

6.3. Modification strategies and their impact on SFMP performance

To significantly boost the photocatalytic activity and efficiency of SFMPs for CO2 reduction, a diverse array of advanced modification approaches has been developed and extensively explored (Fig. 12). These strategies include doping with metal/nonmetal elements to tailor bandgaps and introduce defects, creating oxygen vacancies to enhance adsorption and charge separation, and controlling morphology for improved light harvesting and active site exposure. Moreover, incorporating the plasmonic effect has been demonstrated to enhance light absorption and the generation of hot electrons. Concurrently, the construction of Type II heterojunctions and Z-scheme systems has been shown to effectively separate charges and maintain strong redox potentials. Each approach contributes uniquely to enhancing CO_2 activation and conversion efficiency, as further discussed below. The following sections delve into specific examples of how different modification strategies enhance the photocatalytic CO_2 reduction efficiency of SFMPs, building upon the general principles outlined previously and referencing the summarized data in Table 5.

6.3.1. Doping

The modification of SFMP by doping introduces tailored electronic and surface properties that enhance light absorption, charge separation, and redox activity. The incorporation of metal dopants (e.g., Ce, Mn) allows for the manipulation of the band structure, thereby ensuring a more precise alignment with solar irradiation. This, in turn, facilitates enhanced electron transfer, contributing to an optimized energy conversion process. Guo *et al.* [215] fabricated Ce-doped $ZnFe_2O_4$ spinels, which demonstrated considerable adsorption capacities and high photocatalytic CO_2 reduction with H_2O vapor, producing CO, H_2, and CH_4 under sunlight illumination and a temperature of 200 °C for four hours. The photocatalytic reduction activity of Ce doped $ZnFe_2O_4$ was four times higher than that of the undoped one. The introduction of Ce^{3+} into the $ZnFe_2O_4$ crystal resulted in the formation of a heterojunction between the $ZnFe_2O_4$ and CeO_2 phases. This heterojunction led to several notable improvements in optical properties. Firstly, it enhanced the

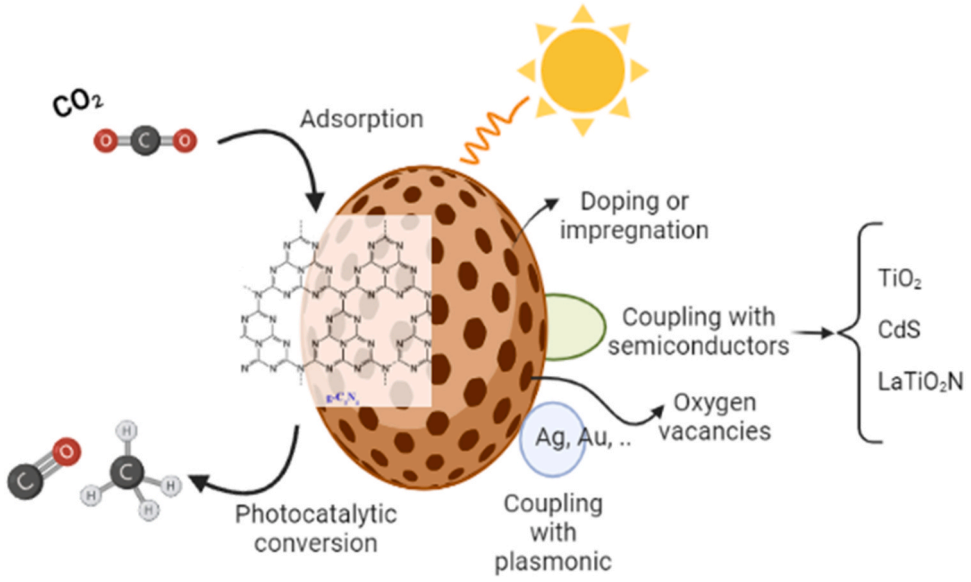

Fig. 12. Schematic illustration of common modification strategies for enhancing the photocatalytic CO_2 reduction efficiency of ferrite-based materials. The figure depicts approaches such as doping, coupling with other semiconductors, introducing oxygen vacancies, and incorporating plasmonic effects to optimize light absorption, charge separation, and CO_2 conversion. The figure was created with BioRender.com.

Table 5
SFMP modification strategies for enhanced photocatalytic co₂ reduction: performance and mechanisms.

Photocatalyst	synthesis approach	Morphology	Optical properties	Irradiation spectrum and source	Reduction product	Proposed Enhancement Mechanism	Ref.
Ce doped $ZnFe_2O_4$	Sol–gel	Polyhedralparticles	1.78, 2.07, 2.22, 2.32, 2.40, 2.47 and 3.4 eV for ZFC_x (x = 0, 0.1, 0.15, 0.2, 0.25 and 0.3) respectively	Visible light	H_2, CO and CH_4	Band-gap tailoring, visible-light utilization, enhanced CO_2 adsorption	[215]
Mn–Fe_3O_4	Dispersion of Mn on Fe_3O_4 microspheres	Microspheres	-	Not applicable (thermal hydrogenation)	Light olefins	Increased BET area, C═O bond activation, inhibited C-C coupling	[205]
Co-α-Fe_2O_3	Alcohol-thermal reaction	Platelet-like	-	Visible light	80.2 % CO (37.8 μmol/h)	Synergistic Co/oxygen vacancies, enhanced selectivity towards CO_2 reduction	[216]
$MgFe_2O_4$	Coprecipitation followed by calcination	Hollow-Cubic structure	1.99–2.04 eV	Visible light	CO and H_2 (24.4 and 34.3 μmol/g/h)	Oxygen vacancies: modified electronic structure, extended photoabsorption, minimized e^-/h^+ recombination	[214]
$CuFe_2O_4/TiO_2$	Sol–gel	Flocculent shapewith a diameter of 1–10 μm	TiO_2 (3.1 eV) $CuFe_2O_4/TiO_2$ (2.61 eV) $CuFe_2O_4$ (1.24 eV)	Visible light (500 W xenon lamp) for 8 h	Methanol(651 lmol/gcat L)	$CuFe_2O_4$ CB shift, Type-II heterostructure for e^-/h^+ separation	[217]
$Co_xZn_{1-x}Fe_2O4@TiO_2$	Co-precipitation followed by calcination of titania anatase	Aggregates of different sizes (less than 150 nm)	3.14 – 3.19 eV	UVC light irradiation via6 UVC-lamps (Philips TUV 6 W TL mini)	CO and CH_4	Z-scheme ($ZnFe_2O_4@TiO_2$); Type-I heterojunction ($CoFe_2O_4@TiO_2$)	[218]
α-$Fe_2O_3/LaTiO_2N$	Solvothermal	Fine particles distributed on plates	2.05 eV	300 W Xe lamp simulated light source/3h	CO and CH_4	Synergistic CO_2 adsorption & direct Z-scheme charge transfer	[207]
α-Fe_2O_3/CdS	Two-step solvothermal	Hierarchical flower-like microsphere	2.05 and 2.75 eV for α-Fe2O3 and CdS	Solar light	CO	Direct Z-scheme enhanced charge separation & lifetime; Interfacial electronic coupling	[219]
g-C_3N_4 QDs/Au NPs/ CeO_2/Fe_3O_4	Hydrothermal-calcination, deposits grow and self-assembly processes	Micro flowers	2.83 eV and 1.46 eV for CeO_2 MFs and CN QDs	UV–vis light	CO and CH_4	Enhanced charge separation via $Ce^{4+} \rightarrow Ce^{3+}$, oxygen defects, Z-scheme, heterojunctions; Magnetic recovery	[220]
$ZnFe_2O_4/Ag/TiO_2$	Photo-deposition assisted solvothermal	$ZnFe_2O_4$ microspheres deposited over TiO_2 NRs	2.15 eV	UV-light irradiation with 200 Hg lamp	CO, CH_4 and CH_3OH	Z-scheme heterojunction; Ag-NPs as metal mediator	[221]
$Fe_3N/Fe_2O_3/C_3N_4$	Thermal pyrolysis	Structure includes three different phases:a) layered g-C_3N_4 nanosheets.b) Spherical Fe_3N grains.c) dark black particles of Fe_2O_3	2.23 eV	300 W xenon lamp with 420 nm cut-off filter	CO 8.03 and CH_4 1.6 μmol/g/h	Z-scheme charges pathway; Fe_2O_3 increases photosensitivity & mediates e^-	[222]
$K_4Nb_6O_{17}/Fe_3N/$ α-Fe_2O_3/C_3N_4	One-step thermal pyrolysis	Nanoflakes (diameter of a few hundred nm)	2.75 eV	300 W xenon lamp with a 420 nmcut-off filter	CO and CH_4(7.01 and 1.3 μmol/g/h respectively).	Coexistence of 4 photosensitive compounds; 4 interfacial junctions for charge transport; Fe_3N electron mediator	[223]
α-Fe_2O_3/g-C_3N_4	Hydrothermal	Honeycomb-like porous structure	2.79 and 2.04 eV for g-C_3N_4 and α-Fe_2O_3 respectively	Visible light 300 W Xenon lamp with a 420 nm cut-off filter	CH_3OH	Band-gap tailoring; Z-scheme transfer mechanism	[224]
rGO@CuZnO@Fe_3O_4	Ionic interaction followed by hydrothermal	Core-shell microspheres	1.44 eV	Visible light 20 W white cold LED light	CH_3OH(2656 μmol/g cat)	rGO facilitated electron transport; Fe_3O_4 facilitated charge migration & magnetic recovery; Cu captured electrons	[225]
Fe_3O_4@NC/Cu_2O	Cu^{2+} reduction followed by aerobic oxidation	Rod-shaped core-shell	Optical band gap is difficult to determine for black catalysts	5 W Xenon HID lamp (irradiance of 12.5 cm^{-2})	CH_3OH	Nitrogen doping inhibited recombination; Surface Cu_2O NPs increased S_{BET}; Fe_3O_4 core retarded photo-corrosion &	[226]

(*continued on next page*)

Table 5 (*continued*)

Photocatalyst	synthesis approach	Morphology	Optical properties	Irradiation spectrum and source	Reduction product	Proposed Enhancement Mechanism	Ref.
						enabled magnetic recovery	
$CoO_x/ZnFe_2O_4$@H-TiO_2/Au-Cu	Stepwise solvothermal	Double-shell hollow nanospheres	1.89 and 2.91 eV	Visible light irradiation. by 300 W Xe lamp with AM1.5 filter	CH_4 21.39 μmol/g/h with 93.8 % selectivity	Double-shell inhibited bulk recombination; Type-II heterojunction; Au-Cu/CoO cocatalysts trapped e^-/h^+	[227]
Co_3O_4@$CoFe_2O_4$	Solvothermal synthesis followed by thermal treatment	Hierarchical hollow double-shelled nano-boxes	1.42 and 1.69 eV for $CoFe_2O_4$ and Co_3O respectively	300 W Xelamp	CH_4 and CO	Hierarchical hollow cubic structure increased photo-utilization/absorption; Z-scheme facilitated e^-/h^+ transfer	[228]

absorption of visible light, resulting in an increase in photoinduced charges. Secondly, it reduced PL emissions by delaying recombination. Thirdly, it enhanced chemisorption and activation of CO_2, thereby forming the reduction precursor CO_2 in the presence of water vapor. Jiang *et al.* [205] used Mn-Fe_3O_4 catalyst for the highly selective conversion of CO_2 to light olefins via reductive hydrogenation. The manganese promoter has demonstrated a number of significant effects, including an increase in the BET area, an enhancement of surface adsorption toward CO_2 by virtue of its provision of active sites, a facilitation of the activation of C═O bonds cleavages on both sides, a maximization of the effective yield of hydrocarbons, and a retardation of the formation of long C–C chains via secondary hydrogenation, thereby favoring the selectivity of light olefins. The mechanism involves two steps, namely first adsorption and the reduction of CO_2 on the catalyst surface producing CO via reverse water–gas shift (RWGS, $CO_2 + H_2 \rightarrow CO + H_2O$). The second step involves activation of the C═O bond and hydrogenation to form C–C chains via Fischer–Tropsch synthesis (FTS, $n\ CO + 2n\ H_2 \rightarrow C_nH_{2n} + n\ H_2O$).

The discussion now includes the transformative potential of two-dimensional (2D) materials, such as graphene, layered double hydroxides, molybdenum disulfide (MoS_2), bismuthene, and MXenes, in enhancing the photocatalytic reduction of CO_2 [229–231]. These materials have significant key advantages, including an exceptionally large specific surface area, abundant active sites, and atomic thickness that facilitates efficient charge transfer, and tunable electronic properties [229]. For example, 2D graphene oxide (GO)-diketopyrrolopyrrole (DPP) film photocatalysts have shown remarkable CO production rates of 32.62 μmol g^{-1} h^{-1} in aqueous solutions, achieving almost 100 % selectivity without the need for sacrificial agents [232]. Similarly, MXenes (e.g., Ti_3C_2Xy) coupled with ZrO_2 photocatalysts have significantly boosted CO formation rates by 6.6 times to 4.6 μmol h^{-1} g_{cat}^{-1} [233]. MXenes function as efficient co-catalysts due to their high electrical conductivity and rich surface functionalities, which promote electron-hole separation and enhance CO_2 adsorption and activation. The ability to control magnetism in 2D van der Waals materials using heat or laser pulses suggests exciting avenues for integrating magnetic separability with advanced photocatalytic properties, potentially offering a new dimension for catalyst recovery and manipulation [234]. This widespread adoption of 2D materials signifies a conceptual shift in catalyst design, moving towards engineering interfaces at the nanoscale to optimize charge dynamics and catalytic performance.

6.3.2. Oxygen vacancies

The incorporation of oxygen vacancies into SFMP has been demonstrated to enhance its photocatalytic activity. This enhancement is attributed to the creation of defect sites, which facilitate charge separation and improve CO_2 adsorption. These vacancies narrow the band gap and serve as active centers for electron transfer, enabling more efficient photocatalytic reduction of CO_2. For example, Yang *et al.* [216] designed an efficient cocatalyst by decorating α-Fe_2O_3 with 1 % Co centers and oxygen defects. This cocatalyst was then utilized for the highly selective photoreduction of CO_2 to CO (80.2 %) where $[Ru(bpy)_3]Cl_2$ was employed as the photosensitizer. Oxygen vacancies enhanced CO_2 adsorption, whereas dispersed Co centers acted as reaction sites and facilitated the transfer of photogenerated electrons from the photosensitizer. Notably, the yield of CO decreased when the reaction time exceeded 2.5 h, which might be attributed to the degradation of the photosensitizer. Both photoreduction activity and CO selectivity significantly decreased as a result of the absence of oxygen vacancies when the 1 %Co-α-Fe_2O_3 catalyst was annealed in air.

Fu *et al.* [214] successfully improved the CO_2 photocatalytic reduction activity of $MgFe_2O_4$ by introducing oxygen vacancies via high-temperature calcination (650–850 °C) under visible light illumination, giving a high yield of CO and H_2. The results show an increase in the oxygen vacancies' concentration within increasing calcination temperature, followed by decreasing vacancies beyond 750 °C. The Mg-Fe-750 displayed the highest EPR signal, implying the highest oxygen vacancies concentration. The increase in oxygen vacancies upon calcination is attributed to the formation of spinel phase crystals below 750 °C. TG analysis shows a decrease in sample weight with increasing temperature (600–750 °C) then weight gain at (800–850 °C) as a result of iron oxide formation resulting from reacting $MgFe_2O_4$ with O_2 at higher temperatures. The introduction of oxygen vacancies boosted the PCA by: (i) enhancing visible light absorption; (ii) the inhibition of e^-/h^+ recombination; and (iii) increasing the chemical adsorption of the catalyst towards CO_2.

6.3.3. Morphology

Modifying the morphology of SFMP offers a powerful strategy to enhance their photocatalytic efficiency for CO_2 reduction. The strategic tailoring of structures such as core–shell microspheres, nanorods, or hollow nanospheres, researchers can improve light harvesting, charge separation, and reactant accessibility. These morphological designs enable synergistic interactions among multi-component systems, facilitating selective and efficient CO_2 conversion into valuable fuels under visible light. Kumar *et al.* fabricated magnetically-recoverable core-shell microspheres of CuZnO@Fe_3O_4 wrapped in reduced graphene oxide (rGO@CuZnO@Fe_3O_4) and used it for the selective reduction of CO_2 to CH_3OH with H_2O under visible irradiation [225]. The restoration of the sp^2 hybridized aromatic system in rGO facilitated electron transportation resulting in better charge separation. The photocatalytic effect is due to the synergism between hetero-catalytic components providing high electron mobility, which is detailed in the following points: (I) the efficient transfer of e^-/h^+ of Fe_2O_3/Fe_3O_4 to ZnO; (II) copper content trapped photoinduced electrons and reduced electron–hole pair recombination; (III) rGO wrap onto ZnO@Fe_3O_4 microspheres enhances methanol selectivity due to efficient electron transfer from the CB of ZnO to the rGO sheets. The catalyst is magnetically-recoverable for six cycles without a significant decrease in methanol yield.

Movahed *et al.* [226] developed Cu_2O NP_S decorated on Fe_3O_4@N-C

NRs-shaped core-shell and investigated its photocatalytic activity on the selective photoreduction of CO_2 to CH_3OH under visible light illumination. Photocatalytic CO_2 reduction with Fe_3O_4@N-C/Cu_2O was found to be four times higher than that of Fe_3O_4/Cu_2O, with the catalyst retaining its reactivity for only four cycles. The unique PCA is a result of three factors: (I) surface-immobilized Cu_2O NPs increase S_{BET} that not only facilitates the absorption and utilization of sunlight but also makes better contact between photocatalysts and CO_2. (II) Fe_3O_4 core rods retarded the photocorrosion of Cu_2O, enhanced the photogeneration of e^-/h^+, and enabled the magnetic recovery of the catalyst. (III) Nitrogen doping into the carbon layer increased the hydrophilicity, improving the dispersibility of the magnetic core and hindering their agglomeration in the solution. Furthermore, nitrogen moieties on the carbon layer served as anchoring sites of the Cu species and the N–C layer retards the recombination of the photoinduced e^-.

Liu *et al.* designed and fabricated double-shell hollow heterostructure nanospheres of $ZnFe_2O_4$@Hollow-TiO_2 anchored with a dual-separated cocatalyst of CoO and Au–Cu [227]. They claimed the creation of surface oxygen vacancies for enhancing visible light utilization, improving carriers' separation and enabling photocatalytic CO_2 reduction with 93.8 % selectivity towards CH_4. A CoO oxidation cocatalyst was used for trapping holes, while Au–Cu reduction cocatalysts were trapping electrons. A high PCA was obtained when oxidation and reduction cocatalysts were separately loaded, which facilitates carriers' separation and inhibits their recombination (Fig. 13). The hollow spherical structure might result in bulk recombination of the photoinduced charges, a phenomenon that was overcome by the formation of a staggered heterojunction between $ZnFe_2O_4$ and H-TiO_2, which strongly accelerated the transfer and separation of the photogenerated e^-/h^+ pairs. The hollow structure also provides a large surface area and high light exploitation. The mechanism involves visible light photosensitization of the composite, which provides e^- that in turn migrates across the heterojunction and is trapped by the reduction cocatalyst Au–Cu and then, finally, participates in CO_2 reduction to CH_4. Meanwhile, photoinduced h^+ also migrates across the junction and is trapped by the oxidizing cocatalyst CoO before participating in water oxidation.

Long *et al.* developed a hierarchical hollow double-shelled nanoboxes of Co_3O_4@$CoFe_2O_4$ photocatalyst utilizing $[Ru(bpy)_3]Cl_2{\cdot}6\ H_2O$ as a photosensitizer [228]. The unique morphology provides a large surface area that boosts light absorption and enhances the adsorption of CO_2 molecules. The Z-scheme heterojunction provided a short electron transport pathway and strengthened the charge density, giving a stronger oxidation/reduction ability. Under UV–vis irradiation, the photocatalyst exhibited a high reduction strength for CO_2 to CO and CH_4. The reaction mechanism postulated that the CO was formed from activated CO_2^-, whereas CH_4 was produced from either the formate intermediate (COO^-) or the consumption of CO by six electrons, when sufficient electrons are provided by the photocatalyst [228].

6.3.4. *Plasmonic effect*

The incorporation of plasmonic nanostructures into SFMP significantly enhances their photocatalytic performance for CO_2 reduction by exploiting localized surface plasmon resonance (LSPR). Plasmonic metals such as Au and Ag generate energetic "hot electrons" under light irradiation, facilitating charge separation and direct injection of electrons into ferrite conduction bands or adjacent semiconductors. This synergistic interaction boosts light absorption, promotes efficient charge transfer, and increases the overall yield and selectivity of CO_2 photoreduction products. Wei *et al.* [220] co-modified CeO_2/Fe_3O_4 micro-flowers with g-C_3N_4 QDs (CN QDs) and Au nanoparticles for the purpose of preparing a photocatalytic composite nominated (CACeF). The composite was examined for CO_2 reduction to CO and CH_4. The modified composite showed, respectively 5- and 8-times higher yield than that of pure CeO_2 under the illumination of UV–visible light. The enhanced photocatalytic activity was attributed to some factors. First, (I) the conversion of Ce^{4+} to Ce^{3+} conversion and oxygen defects on the CeO_2 surface were observed to enhance the separation of photogenerated e^-/h^+; (II) a Z-scheme charges pathway formed between Fe_2O_3/CeO_2; (III) a heterojunction between CeO_2 and g-C_3N_4 that facilitates charge separation; (IV) LSPR of Au, which not only photosensitized CeO_2 but also produced hot electrons participated directly in CO_2 reduction; and (V) Fe_2O_3 enabled the magnetic recovery and promoted light utilization of the composite.

Tahir [221] synthesized $ZnFe_2O_4$ microspheres, coupled with Ag/TiO_2 nanorods, to develop a Z/scheme heterojunction that facilitates photocatalytic reduction of CO_2 to CO, CH_4, CH_3OH, and C_2H_6 under UV and visible light irradiation in the presence of H_2O in a fixed bed reactor system. 1D TiO_2 NRs facilitate a one-directional flow of photogenerated electrons to VB of $ZnFe_2O_4$ microspheres due to the Z-scheme assembly ($ZnFe_2O_4$/TiO_2) obtained under UV irradiation, whereas Ag acts as a metallic mediator. Water oxidation would occur at a VB of TiO_2 NRs and CO_2 reduction at a CB of $ZnFe_2O_4$. The photocatalyst was found to be effective and stable for four cycles; after the fourth cycle, the amount of CO was 1.06-fold lower compared to the first cyclic run, while CH_4 was increased by 1.07-fold higher than it was produced in the first cycle.

6.3.5. *Type II heterojunction*

The formation of type-II heterojunctions between SFMP and semiconductors presents a powerful strategy to enhance photocatalytic CO_2 reduction efficiency. In such systems, staggered band alignments facilitate spatial separation of photogenerated electrons and holes, reducing recombination and boosting charge carrier lifespan. By coupling ferrites

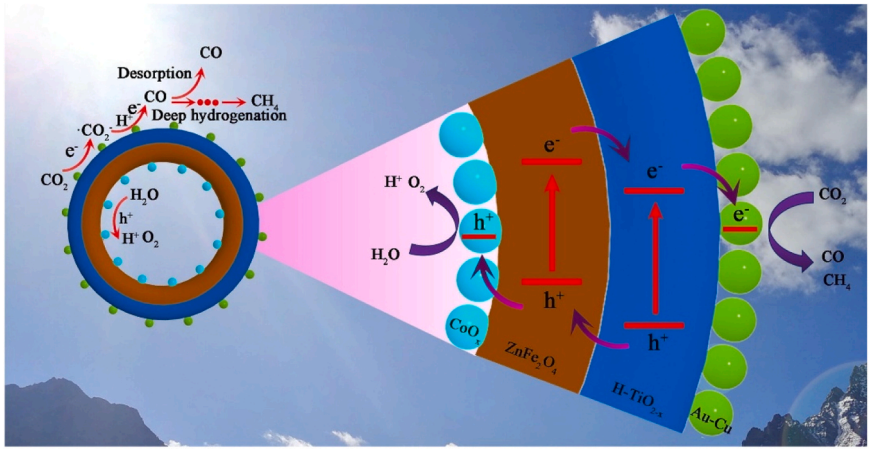

Fig. 13. Mechanism of photocatalytic CO_2 reduction showing charge transfer across the hollow structured photocatalyst $ZnFe_2O_4$@H-TiO_2 and separately loaded cocatalysts (CoO and Au–Cu) Adapted from [227] with copyright permission from Elsevier, 2021.

like $CuFe_2O_4$ or $ZnFe_2O_4$ with TiO_2 or other narrow-bandgap materials, the heterostructure not only tailors band positions to match redox potentials but also improves visible-light absorption and catalytic selectivity toward CO_2 reduction products such as methanol or CO. Uddin *et al.* [235]investigated the photocatalytic reduction of CO_2 to methanol using $CuFe_2O_4/TiO_2$ under visible irradiation, giving a three times higher yield than that of $CuFe_2O_4$ (with the stepwise addition of the catalyst). A low formation rate of methanol on $CuFe_2O_4$ alone was observed due to the large difference between the potential of $CuFe_2O_4$ CB (−1.03 V) and the redox couple (−0.38 V) of photoreduction. Loading TiO_2 onto $CuFe_2O_4$ raised the methanol yield and increased the photocatalytic reduction activity due to three reasons: (I) The band gap of the material was modified to align with the standard reaction potential by adjusting the CB of $CuFe_2O_4$ to a more negative level; (II) $CuFe_2O_4/TiO_2$ Type-II hetero-structure promoted the e^-/h^+ separation and retard their recombination. The methanol formation mechanism follows Eq. 8:

$$CO_2 + 6\ H^+ + 6\ e^- \rightarrow CH_3OH + H_2O\ E^0_{ox} = -0.38\ V \quad (8)$$

In a related study, Ciocarlan *et al.* [218] coupled doped Ferrite nanocomposites of $Co_xZn_{1-x}Fe_2O_4$ with TiO_2 for improving the photocatalytic CO_2 reduction with hydrogen under UVC light irradiation within a fixed-bed batch reactor. The CO_2 reduction to CO exhibited a direct proportionality to the Zn:Co ratio, thereby confirming that Zn ferrites demonstrate significantly higher activity compared to Co ferrites. This is evidenced by an 80 % increase in CO yield, which possesses the potential to further react with H_2 in the rector-producing syngas. The reduction of CO_2 to CH_4 is more favorable when using a Co ferrite photocatalyst. Mott-Schottky plots provide evidence that the junction across $ZnFe_2O_4/TiO_2$ functions as a Z-scheme charge transfer pathway mechanism. In contrast, a type I heterojunction was observed across $CoFe_2O_4/TiO_2$.

Song *et al.* [207] converted CO_2 into CO and CH_4 via visible light photocatalytic reduction using α-$Fe_2O_3/LaTiO_2N$. α-Fe_2O_3 has been demonstrated to enhance the photocatalytic activity of $LaTiO_2N$ in three ways: (I) an increase in SSA from 6.8 (pristine LTON) to 15.0 m^2/g, which increases CO_2 adsorption ability; (II) a direct Z-scheme pathway that facilitate charge separation (proved by Nyquist plots with a semicircular shape), which in turns improves charge generation and migration (as proven by the TPC plot), and inhibits recombination by elongating a carrier's lifetime (proved by the TRPL spectra); (III) bandgap shifting towards longer wavelengths. Furthermore, α-Fe_2O_3 showed a strong water oxidation capacity with a lower VB edge position, whereas $LaTiO_2N$ displayed a strong CO_2 reduction ability with a higher CB edge position. The formation of the heterojunction between α-Fe_2O_3 and $LaTiO_2N$ was confirmed by the XPS spectra of the composite, which showed shifting O 1 s, N 1 s, and Fe 2p peaks of α-$Fe_2O_3/LaTiO_2N$ towards lower binding energies, whereas La 3d and Ti 2p peaks of the LATN were shifted towards the opposite direction. This shift in binding energies is indicative of the formation of a built-in electric field with direction from LTON to α-Fe_2O_3.

Long *et al.* constructed a 2D/2D α-Fe_2O_3/CdS bilayer heterostructure and applied it to photocatalytic CO_2 reduction [219]. The photocatalytic enhancement was mainly attributed to: (i) effective interfacial electronic coupling resulting in a favorable internal built-in electric field (IEF); (ii) a short diffusion distance to the interface between 2D-CdS and 2D-α-Fe_2O_3; and (iii) a direct Z-scheme charge transfer pathway across the large bilayer interface.

6.3.6. Z-scheme

Z-scheme ferrites were introduced for photocatalytic reduction of CO_2 primarily to overcome the limitations of traditional single-component systems. The primary function of these materials is to provide efficient charge separation, strong redox ability, and enhanced light absorption. These elements are indispensable for driving the complex, multi-electron CO_2 reduction process. For example, Padervand *et al.* [222] synthesized a novel ternary $Fe_3N/Fe_2O_3/C_3N_4$ photocatalyst from cheap raw material and applied it to the photocatalytic reduction of CO_2 with H_2O vapors (gas phase reduction) under visible light irradiation. The ternary composite showed CO_2 photoreduction activity seven times higher than that of C_3N_4. That enhancement could be attributed to: (i) The presence of Fe_2O_3 resulted in an increase in photosensitivity, leading to the generation of greater quantities of e^-/h^+ pairs following visible light irradiation; (ii) The presence of Fe_2O_3 resulted in an increase in photosensitivity, leading to the generation of greater quantities of e^-/h^+ pairs following visible light irradiation; and (iii) the Z-scheme pathway, which facilitated carriers' migration across the ternary interfaces and inhibited their recombination. Products of photocatalytic CO_2 reduction detected by gas chromatography were CO (produced at the beginning of the reaction and it started fading smoothly after 1 h) and CH_4 (evolution rate increased slowly along the reaction time). Another study reported the fabrication of a magnetically reusable quaternary $K_4Nb_6O_{17}/\alpha$-$Fe_2O_3/Fe_3N/g$-C_3N_4 photocatalyst, which exhibited boosted photoreduction activity of CO_2 14.6-fold higher than that of g-C_3N_4 [223]. The enhanced photocatalytic activity could be ascribed to the coexistence of various photosensitive compounds that increase light harvesting and the presence of four interfacial junctions, facilitating charge transportation. Moreover, the coexistence of a large number of active sites on the surface of the four crystalline phases can efficiently enhance the photocatalytic reduction process. Fe_3N exhibits unique magnetic and electronic properties that play an essential role in photocatalyst reusability and prolong the carriers' lifetimes by acting as an electron mediator [222]. Guo *et al.* [224] analyzed the photocatalytic activity of α-Fe_2O_3/g-C_3N_4 for the photo-reduction of CO_2 to methanol under visible irradiation at 20 °C and 0.6 MPa. The composite α-Fe_2O_3/g-C_3N_4 showed a three times higher level of CO_2 reduction activity than that of lone g-C_3N_4 for two reasons: (i) α-Fe_2O_3 enhanced visible light utilization; and (ii) Z-scheme transfer mechanism (heterojunction) facilitated separation of photogenerated e^-/h^+ and suppresses their recombination. The mechanism involves the photooxidation of H_2O in the VB of Fe_2O_3 and photocatalytic CO_2 reduction to CH_3OH in the CB of g-C_3N_4.

7. Future perspectives

While significant progress has been made in ferrite-based nanomaterials for photocatalytic CO_2 reduction, several critical challenges and unresolved questions must be addressed to translate laboratory success into practical applications. These challenges span fundamental mechanistic understanding, experimental methodologies, scalable system design, and environmental sustainability.

This review has highlighted recent progress and issues associated with the properties and synthesis of magnetic nanoparticle ferrites with controlled size, crystallinity, and composition as active photocatalysts for different photo-based applications. Numerous synthetic approaches have been developed and explored including coprecipitation, hydrothermal, microemulsion, simple thermal decomposition, microwave-assisted, and bio-based methodologies. Hydrothermal, coprecipitation, and sol-gel methods are the most prevalent approaches for producing MNPs. Despite substantial progress, significant gaps remain in synthetic methodology for controlling key variables, including the cost of chemical design, particle size, the chemistry of the desired structure, and the material quality for the photocatalytic application. Furthermore, a deeper understanding of which of the aforementioned factors is the most significant for evaluating photochemical stability and performance. From a morphological perspective, the controlled addition of surfactants offers advantages during the synthetic of MNPs strategy, due to the interaction between metallic contents and the surfactant, which can control particle aggregation and enable controllable particle growth. Furthermore, the remaining surfactant content on the prepared MNPs might block some active sites, creating performance issues, therefore

complete surfactant removal is essential to maintain catalytic activity. The hydrothermal process is often preferred over sol-gel and other approaches because it could produce NPs of the desired size, crystallinity, and compositional consistency. However, the requirement for high temperatures and pressures, as well as specialized reactors, makes this strategy less energy-efficient compared to other synthesis techniques.

Improved photocatalytic performance could be achieved by designing MNPs with high porosity characteristics. The porosity of prepared MNPs plays a crucial role in their photocatalytic performance and adsorption capacities. Higher surface area provides better quantity and quality of active sites, resulting in enhanced adsorption capacity. Additionally, porosity creates efficient pathways and more active sites for charge transfer during photocatalytic applications.The overall properties of MNPs can be tailored through additional design considerations, including doping to introduce vacancies or crystal defects. The presence of dopant elements during material processing can modify ion distribution and significantly affect physicochemical characteristics. Moreover, novel or enhanced properties can be achieved through exchange coupling between soft and hard MNPs for specific applications. Therefore, optimization between the synthetic cost, desired physicochemical character (including morphology, porosity, and crystallinity), and photocatalytic performance should be discussed in future studies.

Commercial-scale production of MNPs represents one of the key factors for accelerating the commercialization of photocatalysts. Unfortunately, most of the reported synthesis strategies that have been studied ignored commercial requirements, often employing toxic solvents, complex reactors, high-cost precursors, and extreme pressure and temperature. To attract industrial application of MNPs, environmentally friendly and reproducible chemical strategies that can be optimized for commercial use are essential. This requires elaborate studies from multiple research groups to confirm reproducible, low-cost, and efficient MNP production.

The transition from laboratory-scale synthesis to commercial production necessitates a thorough environmental assessment. For instance, a recent study utilizing the Waste Reduction Algorithm (WAR) for large-scale magnetite (Fe_3O_4) nanoparticle production via co-precipitation (806.87 tons/year capacity) indicated that the process, when optimized, can be environmentally friendly, showing negative Potential Environmental Impacts (PEI)[236]. However, this assessment also highlighted that the main environmental impacts often arise from downstream processes, such as the centrifugation unit for separation, rather than the core synthesis reaction itself.[256] This finding underscores the need for holistic life cycle assessments (LCA) that consider the entire product lifecycle, from raw material extraction to end-of-life management, rather than focusing solely on 'green synthesis' at the initial stage. Currently, the literature lacks comprehensive LCA studies for many nanomaterials, which can lead to misleading conclusions about their overall environmental performance.

A promising future trend in synthetic methods involves the utilization of industrial waste as a raw material for ferrite production, as summarized in Fig. 14**.** This approach aligns with circular economy principles and addresses both waste management and resource sustainability challenges. The design process typically begins with the identification of waste sources, which may include industrial waste (e.g., ash, mud, sludge), agricultural biomass, and electronic waste (e.g., computers, batteries, phones, and circuit boards) [237]. These wastes often contain significant quantities of transition metals (Fe, Co, Ni, Mn) critical for magnetic nanoparticle fabrication. After waste sorting, a pre-treatment phase is essential to prepare raw materials for further processing. Pre-treatment procedures often involve drying, grinding, sieving, and, in certain instances, heat activation (e.g., calcination or pyrolysis) to improve metal accessibility and eliminate organic materials. Following extraction, these materials undergo various material synthesis procedures, including co-precipitation, sol-gel methods, hydrothermal or solvothermal approaches, and, progressively, green synthesis utilizing plant extracts or biotemplates. These methods facilitate control over material shape, crystallinity, and dimensions, all critical for photocatalytic efficacy. Fig. 14 provides a comparative overview, contrasting recent advancements and conventional challenges with the future prospects enabled by waste-driven material design.

Another primary challenge lies in the ambiguous reaction pathways and unclear charge transfer mechanisms within complex photocatalytic systems. Despite numerous heterojunction photocatalysts being reported, direct evidence for the precise charge transfer pathways (e.g., built-in electric fields, specific electron/hole migration routes) frequently remains insufficient, and theoretical computations can still be speculative. The dynamic nature of photocatalyst surfaces, which can undergo kinetic state or even shape changes during reactions, further

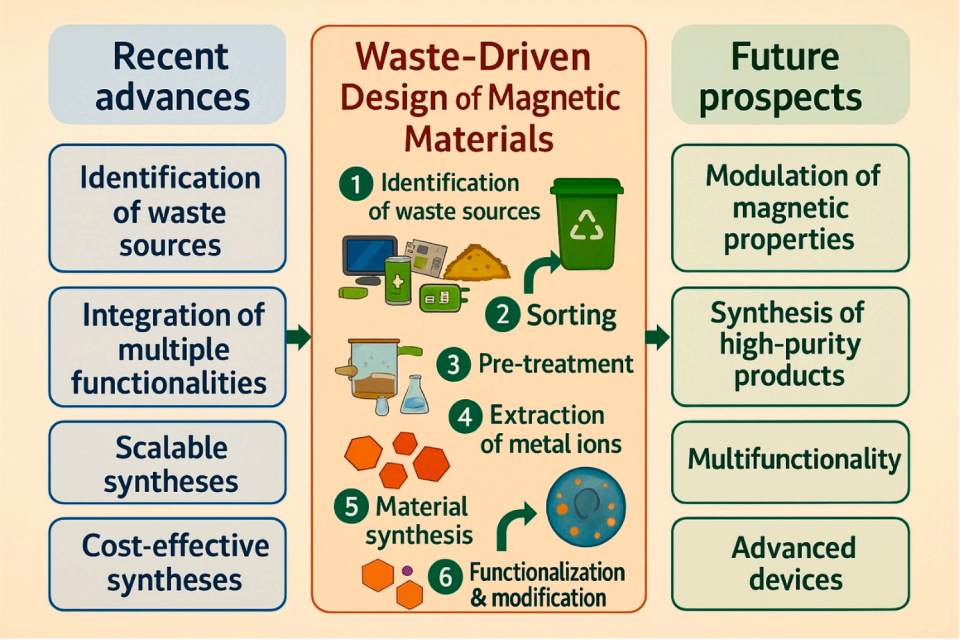

Fig. 14. Schematic illustration of the design pathway for waste-derived magnetic photocatalysts. The comparative overview within the figure further highlights recent advancements and conventional challenges alongside the promising future prospects enabled by this sustainable waste valorization approach.

complicates understanding. Future efforts must prioritize a clever combination of advanced spectroscopic characterizations (e.g., in situ XPS, femtosecond transient absorption spectra, Kelvin probe force microscopy) and sophisticated theoretical calculations to elucidate these intricate mechanisms at an atomic and molecular level.

Artificial intelligence (AI) and machine learning tools are expected to play a more significant role in forecasting waste composition and customizing synthesis settings for optimal efficacy. Moreover, the integration of photocatalysis with other technologies, such as photo-supercapacitors and solar fuel generation systems, creates opportunities for hybrid devices that simultaneously purify the atmosphere and store energy. Ultimately, comprehensive legislative backing and industrial collaboration will be essential for the widespread adoption of these materials, facilitating the transition from laboratory synthesis to pilot or large-scale applications that utilize municipal and agricultural waste streams.

8. Conclusions

This review offers a comprehensive of the advancements in ferrite-based magnetic nanomaterials for photocatalytic CO_2 reduction, distinguishing itself by focusing specifically on the unique advantages, synthesis, and modification strategies pertinent to ferrites. Ferrite-based magnetic nanomaterials exhibit significant potential in photocatalytic applications, particularly in terms of environmental remediation and sustainable energy production. Their unique properties, such as low toxicity, cost-effectiveness, and efficient magnetic separation, make them viable candidates for the photocatalytic CO_2 reduction. Magnetic photocatalysts are typically composed of a magnetic core, which facilitates easy separation and recovery, and a photoactive semiconductor shell. This dual structure ensures both high photocatalytic activity and catalyst reusability. The review has detailed various synthetic approaches, and emphasized how these strategies influence the final structure, stability, and photocatalytic efficiency of the materials.

The enhanced photocatalytic performance of ferrite-based nanoparticles is achieved through various advanced design strategies, including dimensional tuning, co-catalyst integration, heterojunction formation, and the engineering of oxygen vacancies. By modifying physicochemical properties like bandgap energy, surface area, and charge separation efficiency, the photocatalytic activity of these materials can be optimized for the selective conversion of CO_2 into valuable products. This review underscores the importance of the further development of ferrite-based photocatalysts to overcome current limitations and advance sustainable solutions for environmental challenges. The strategic design of waste-driven magnetic photocatalysts presents a versatile, promising frontier. This approach paves the way to green synthesis techniques and application-driven design, redefining the role of waste in next-generation catalytic technologies. Future progress will depend on integrating these innovative material designs with a deeper mechanistic understanding to create practical and scalable systems for a sustainable future.

CRediT authorship contribution statement

Khaled M. Amin: Writing – original draft, Supervision, Visualization, Conceptualization, Writing – review & editing, Data curation. **Nada A. Eldeeb:** Writing – original draft, Writing – review & editing, Data curation, Visualization. **Zineb Gargar:** Visualization, Writing – review & editing, Data curation, Writing – original draft. **Ibrahim M.A. Mohamed:** Conceptualization, Visualization, Writing – review & editing, Supervision, Writing – original draft, Data curation. **Mohamed Elsenety:** Visualization, Conceptualization, Writing – original draft, Data curation, Writing – review & editing, Supervision. **Mahmoud M. Emara:** Supervision, Conceptualization, Writing – review & editing, Data curation, Writing – original draft. **M. Abd Elkodous:** Writing – original draft, Data curation, Writing – review & editing, Visualization. **Marwa M. Abouelela:** Data curation, Writing – original draft, Writing – review & editing, Visualization. **Poussy A. Ibrahim:** Data curation, Visualization, Writing – original draft, Writing – review & editing. **Abdelmoneim A. Ayed:** Writing – review & editing, Data curation, Visualization, Writing – original draft. **Hani Nasser Abdelhamid:** Writing – review & editing, Data curation, Writing – original draft, Visualization. **Hesham A. Hamad:** Writing – original draft, Data curation, Supervision, Writing – review & editing, Visualization, Conceptualization.

Declaration of Competing interest

The authors declare that they have no known competing financial interests or personal relationships that could have appeared to influence the work reported in this paper

Acknowledgement

Open Access publication is funded by the German Research Foundation (Deutsche Forschungsgemeinschaft, DFG) grant number 491111487. Hesham Hamad acknowledges the financial support from the MOPGA 2022 Visiting Fellowship Program for Young Researchers provided by the Ministry of Europe and Foreign Affairs (France) and MAEC-AECID fellowship by the Ministry of Foreign Affairs and Cooperation (Spain).

Data availability

Data will be made available on request.

References

[1] H. Lin, M. Ma, H. Qi, X. Wang, Z. Xing, A. Alowasheeir, H. Tang, S. Chan Jun, Y. Yamauchi, S. Liu, 3D-Printed photocatalysts for revolutionizing catalytic conversion of solar to chemical energy, Prog. Mater. Sci. 151 (2025) 101427, https://doi.org/10.1016/j.pmatsci.2025.101427.

[2] X.J. Wen, X.H. Qiao, Y.X. Li, H. Guo, H.Z. Li, X.K. Wu, B.Bin Qian, Q.H. Xu, Z. T. Liu, Z.H. Fei, Recent advances on Bi12O17Cl2-based photocatalysts for energy and environmental application, J. Clean. Prod. 495 (2025) 145060, https://doi.org/10.1016/j.jclepro.2025.145060.

[3] R. Nawaz, M.M. Hanafiah, Z. Sakawi, Z.A. Baki, S.B.Z. Abidin, M. Anjum, A. Fazli Ismail, U. Arshad, A review of the defective TiO2 materials-based photocatalysis for environmental remediation: exploring the nexus between light wavelength and energy consumption, Appl. Energy 393 (2025) 126143, https://doi.org/10.1016/j.apenergy.2025.126143.

[4] H. Hamad, M. Abd El-Latif, A.E.H. Kashyout, W. Sadik, M. Feteha, Optimizing the preparation parameters of mesoporous nanocrystalline titania and its photocatalytic activity in water: Physical properties and growth mechanisms, Process Saf. Environ. Prot. 98 (2015) 390–398, https://doi.org/10.1016/J.PSEP.2015.09.011.

[5] H.A. Hamad, M. Adel, M.M. Emara, M. Elsenety, I.M.A. Mohamed, A.G. Bedir, Z. Gargar, M.M. Abouelela, N.A. Eldeeb, I. Ibrahim, A.A. Hassan, M. El Abboubi, K.M. Amin, Ferrites/carbon allotropes nanocomposites for photocatalytic applications: A review, Coord. Chem. Rev. 534 (2025) 216537, https://doi.org/10.1016/J.CCR.2025.216537.

[6] E. Casbeer, V.K. Sharma, X.-Z. Li, Synthesis and photocatalytic activity of ferrites under visible light: A review, Sep Purif. Technol. 87 (2012) 1–14, https://doi.org/10.1016/j.seppur.2011.11.034.

[7] P. Singh, K. Sharma, V. Hasija, V. Sharma, S. Sharma, P. Raizada, M. Singh, Systematic review on applicability of magnetic iron oxides e integrated photocatalysts for degradation of organic pollutants in water, Mater. Today Chem. 14 (2019) 100186, https://doi.org/10.1016/j.mtchem.2019.08.005.

[8] M. Fathy, H. Hamad, A.E.H. Kashyout, Influence of calcination temperatures on the formation of anatase TiO2 nano rods with a polyol-mediated solvothermal method, RSC Adv. 6 (2016) 7310–7316, https://doi.org/10.1039/c5ra26739k.

[9] H.A. Hamad, W.A. Sadik, M.M. Abd El-latif, A.B. Kashyout, M.Y. Feteha, Photocatalytic parameters and kinetic study for degradation of dichlorophenol-indophenol (DCPIP) dye using highly active mesoporous TiO2 nanoparticles, J. Environ. Sci. (China) 43 (2016) 26–39, https://doi.org/10.1016/j.jes.2015.05.033.

[10] Z. Huang, F. Sun, Y. Zhang, K. Gu, X. Zou, Y. Huang, Temperature-assisted photochemical construction of CdS-based ordered porous films with photocatalytic activities on solution surfaces (Journal of Colloid and Interface Science), J. Colloid Interface Sci. 356 (2011) 783–789, https://doi.org/10.1016/j.jcis.2011.01.027.

[11] O. Yayapao, T. Thongtem, A. Phuruangrat, S. Thongtem, Ultrasonic-assisted synthesis of Nd-doped ZnO for photocatalysis, Mater. Lett. 90 (2013) 83–86, https://doi.org/10.1016/j.matlet.2012.09.027.
[12] Z. Li, X. Meng, Z. Zhang, Recent development on MoS2-based photocatalysis: A review, J. Photochem. Photobiol. C Photochem. Rev. 35 (2018) 39–55, https://doi.org/10.1016/j.jphotochemrev.2017.12.002.
[13] M. Seifollahi Bazarjani, M. Hojamberdiev, K. Morita, G. Zhu, G. Cherkashinin, C. Fasel, T. Herrmann, H. Breitzke, A. Gurlo, R. Riedel, Visible Light Photocatalysis with c-WO $_{3-x}$ /WO $_3$ ×H $_2$ O Nanoheterostructures In Situ Formed in Mesoporous Polycarbosilane-Siloxane Polymer, J. Am. Chem. Soc. 135 (2013) 4467–4475, https://doi.org/10.1021/ja3126678.
[14] H. Hamad, M. Abd El-Latif, A.E.H. Kashyout, W. Sadik, M. Feteha, Synthesis and characterization of core-shell-shell magnetic (CoFe2O4-SiO2-TiO2) nanocomposites and TiO2 nanoparticles for the evaluation of photocatalytic activity under UV and visible irradiation, N. J. Chem. 39 (2015) 3116–3128, https://doi.org/10.1039/c4nj01821d.
[15] H. Hamad, E. Bailón-García, F.J. Maldonado-Hódar, A.F. Pérez-Cadenas, F. Carrasco-Marín, S. Morales-Torres, Synthesis of TixOy nanocrystals in mild synthesis conditions for the degradation of pollutants under solar light, Appl. Catal. B 241 (2019) 385–392, https://doi.org/10.1016/j.apcatb.2018.09.016.
[16] F. Hiroshi, H. Yukiko, Y. Michichiro, A. Shoichi, Magnetic photocatalyst, JP6154620 (A), 1994.
[17] Y. Zhang, C. Liang, J. Wu, H. Liu, B. Zhang, Z. Jiang, S. Li, P. Xu, Recent Advances in Magnetic Field-Enhanced Electrocatalysis, ACS Appl. Energy Mater. 3 (2020) 10303–10316, https://doi.org/10.1021/acsaem.0c02104.
[18] H.N. Abdelhamid, Delafossite Nanoparticle as New Functional Materials: Advances in Energy, Nanomedicine and Environmental Applications, Mater. Sci. Forum 832 (2015) 28–53, https://doi.org/10.4028/www.scientific.net/MSF.832.28.
[19] M. Dowaidar, H. Nasser Abdelhamid, M. Hällbrink, Ü. Langel, X. Zou, Chitosan enhances gene delivery of oligonucleotide complexes with magnetic nanoparticles–cell-penetrating peptide, J. Biomater. Appl. 33 (2018) 392–401, https://doi.org/10.1177/0885328218796623.
[20] M.L. Bhaisare, H.N. Abdelhamid, B.-S. Wu, H.-F. Wu, Rapid and direct MALDI-MS identification of pathogenic bacteria from blood using ionic liquid-modified magnetic nanoparticles (Fe3O4@SiO2), J. Mater. Chem. B 2 (2014) 4671–4683, https://doi.org/10.1039/C4TB00528G.
[21] D. Fan, Q. Wang, T. Zhu, H. Wang, B. Liu, Y. Wang, Z. Liu, X. Liu, D. Fan, X. Wang, Recent Advances of Magnetic Nanomaterials in Bone Tissue Repair, Front Chem. 8 (2020), https://doi.org/10.3389/fchem.2020.00745.
[22] T. Li, C. Yang, Z. Wei, D. Pei, G. Jiang, Recent Advances of Magnetic Nanomaterials in the Field of Oncology, Onco Targets Ther. 13 (2020) 4825–4832, https://doi.org/10.2147/OTT.S243256.
[23] J. Govan, Recent Advances in Magnetic Nanoparticles and Nanocomposites for the Remediation of Water Resources, Magn. Rev. 49 (2020), https://doi.org/10.3390/magnetochemistry6040049.
[24] S.F. Soares, T. Fernandes, T. Trindade, A.L. Daniel, Recent advances on magnetic biosorbents and their applications for water treatment, Environ. Chem. Lett. (2019), https://doi.org/10.1007/s10311-019-00931-8.
[25] J. Gopal, H.N. Abdelhamid, P.-Y. Hua, H.-F. Wu, Chitosan nanomagnets for effective extraction and sensitive mass spectrometric detection of pathogenic bacterial endotoxin from human urine, J. Mater. Chem. B 1 (2013) 2463, https://doi.org/10.1039/c3tb20079e.
[26] G. Mamba, A. Mishra, Advances in magnetically separable photocatalysts: Smart, Recyclable materials for water pollution mitigation, Catalysts 6 (2016) 1–34, https://doi.org/10.3390/catal6060079.
[27] J. Gómez-Pastora, S. Dominguez, E. Bringas, M.J. Rivero, I. Ortiz, D.D. Dionysiou, Review and perspectives on the use of magnetic nanophotocatalysts (MNPCs) in water treatment, Chem. Eng. J. 310 (2017) 407–427, https://doi.org/10.1016/j.cej.2016.04.140.
[28] M.J. Jacinto, L.F. Ferreira, V.C. Silva, Magnetic materials for photocatalytic applications—a review, J. Solgel Sci. Technol. 96 (2020) 1–14, https://doi.org/10.1007/s10971-020-05333-9.
[29] G. Jia, Y. Zhang, J.C. Yu, Z. Guo, Asymmetric Atomic Dual-Sites for Photocatalytic CO2 Reduction, Adv. Mater. 36 (2024) 2403153, https://doi.org/10.1002/ADMA.202403153.
[30] B. Alqassem, F. Banat, G. Palmisano, M. Abu Haija, Emerging trends of ferrite-based nanomaterials as photocatalysts for environmental remediation: A review and synthetic perspective, Sustain. Mater. Technol. 40 (2024) e00961, https://doi.org/10.1016/j.susmat.2024.e00961.
[31] A. Hayat, M. Sohail, A.Y.A. Alzahrani, H. Ali, A.M. Abu-Dief, M.S. Amin, A. M. Alenad, S.R. Al-Mhyawi, Y. Al-Hadeethi, Z. Ajmal, S.R. Guo, Y. Orooji, Recent advances in heteroatom-doped/hierarchical porous carbon materials: Synthesis, design and potential applications, Prog. Mater. Sci. 150 (2025) 101408, https://doi.org/10.1016/J.PMATSCI.2024.101408.
[32] H. Ali, Y. Orooji, Z. Ajmal, M. Abboud, A.M. Abu-Dief, K.A. Abu Al-Ola, H.M. A. Hassan, D. Yue, S.R. Guo, A. Hayat, A comprehensive Review based on the synthesis, properties, morphology, functionalization, and potential applications of transition metals nitrides, Coord. Chem. Rev. 526 (2025) 216353, https://doi.org/10.1016/J.CCR.2024.216353.
[33] H. Ali, Y. Orooji, A.Y.A. Alzahrani, H.M.A. Hassan, Z. Ajmal, D. Yue, A. Hayat, Advanced Porous Aromatic Frameworks: A Comprehensive Overview of Emerging Functional Strategies and Potential Applications, ACS Nano 19 (2025) 7482–7545, https://doi.org/10.1021/acsnano.4c16314.
[34] A. Hayat, Z. Ajmal, A.Y.A. Alzahrani, M.H. AL Mughram, A.M. Abu-Dief, R. AL-Faze, A.M. Alenad, Y. Al-Hadeethi, H. Ali, S.V. Prabhakar Vattikuti, Y. Orooji, A novel breakthrough in the invention, properties, synthesis of covalent heptazine framework for its sustainable applications, Mater. Today 83 (2025) 331–354, https://doi.org/10.1016/J.MATTOD.2024.12.003.
[35] S. Raza, A.U. Rehman, C. Chen, T. Zhao, A. Hayat, T. Bashir, L. Shen, Y. Orooji, H. Lin, Synergistically self-assembled in situ growth of MXene@MOF derived sodium alginate hydrogel 3D frameworks as next-generation electrocatalysts for oxygen and hydrogen evolution, J. Mater. Chem. A Mater. 13 (2025) 4390–4403, https://doi.org/10.1039/D4TA08240K.
[36] M. Zain Ul Abidin, M. Ikram, S. Moeen, G. Nazir, M.B. Kanoun, S. Goumri-Said, A comprehensive review on the synthesis of ferrite nanomaterials via bottom-up and top-down approaches advantages, disadvantages, characterizations and computational insights, Coord. Chem. Rev. 520 (2024) 216158, https://doi.org/10.1016/J.CCR.2024.216158.
[37] C. Su, Environmental implications and applications of engineered nanoscale magnetite and its hybrid nanocomposites: A review of recent literature, J. Hazard Mater. 322 (2017) 48–84, https://doi.org/10.1016/j.jhazmat.2016.06.060.
[38] M. Shokouhimehr, Magnetically Separable and Sustainable Nanostructured Catalysts for Heterogeneous Reduction of Nitroaromatics, Catalysts 5 (2015) 534–560, https://doi.org/10.3390/catal5020534.
[39] C.A. Orge, O.S.G.P. Soares, P.S.F. Ramalho, M.F.R. Pereira, J.L. Faria, Magnetic Nanoparticles for Photocatalytic Ozonation of Organic Pollutants, Catalysts (2019) 703, https://doi.org/10.3390/catal9090703.
[40] X. Wu, H. Yu, H. Dong, Enhanced infrared radiation properties of CoFe2O4 by doping with Y3+ via sol–gel auto-combustion, Ceram. Int 40 (2014) 12883–12889, https://doi.org/10.1016/j.ceramint.2014.04.147.
[41] L. Xu, Y. Ma, Y. Zhang, Z. Jiang, W. Huang, Direct Evidence for the Interfacial Oxidation of CO with Hydroxyls Catalyzed by Pt/Oxide Nanocatalysts, J. Am. Chem. Soc. 131 (2009) 16366–16367, https://doi.org/10.1021/ja908081s.
[42] V.K. Gupta, D. Pathania, P. Singh, Pectin–cerium (IV) tungstate nanocomposite and its adsorptional activity for removal of methylene blue dye, Int. J. Environ. Sci. Technol. 11 (2014) 2015–2024, https://doi.org/10.1007/s13762-013-0351-8.
[43] T. Palden, M. Regadío, B. Onghena, K. Binnemans, Selective Metal Recovery from Jarosite Residue by Leaching with Acid-Equilibrated Ionic Liquids and Precipitation-Stripping, ACS Sustain Chem. Eng. 7 (2019) 4239–4246, https://doi.org/10.1021/acssuschemeng.8b05938.
[44] M.A.S. Amulya, H.P. Nagaswarupa, M.R.A. Kumar, C.R. Ravikumar, K.B. Kusuma, Sonochemical synthesis of MnFe 2 O 4 nanoparticles and their electrochemical and photocatalytic properties, J. Phys. Chem. Solids 148 (2021) 109661, https://doi.org/10.1016/j.jpcs.2020.109661.
[45] A. Sutka, M. Stingaciu, G. Mezinskis, A. Lusis, An alternative method to modify the sensitivity of p-type NiFe2O4 gas sensor, J. Mater. Sci. 47 (2012) 2856–2863, https://doi.org/10.1007/s10853-011-6115-2.
[46] J. Prakash, R. Jasrotia, Suman, J. Ahmed, S.M. Alshehri, T. Ahmad, M. Fazil, M. Sillanpää, N. Lakshmaiya, V. Raja, Nickel substituted cobalt nanoferrites for advanced photocatalytic and electrocatalytic green hydrogen generation, J. Mol. Struct. 1321 (2025) 140162, https://doi.org/10.1016/J.MOLSTRUC.2024.140162.
[47] T. Ramesh, V. Madhavi, P. Venkateswara Rao, K. Vagdevi, N. Basavegowda, K. H. Baek, Impact of ultrasonic-assisted co-precipitation synthesis and ultrasonication duration on cobalt ferrite nanostructures: A comparative study of structural, morphological, optical and magnetic properties, Inorg. Chem. Commun. 174 (2025) 114035, https://doi.org/10.1016/J.INOCHE.2025.114035.
[48] A. Lu, E.L. Salabas, F. Schüth, Magnetic Nanoparticles: Synthesis, Protection, Functionalization, and Application, Angew. Chem. Int Ed. Engl. 46 (2007) 1222–1244, https://doi.org/10.1002/anie.200602866.
[49] S. Ahmad, H. Ni, F.S. Al-Mubaddel, M.A. Rizk, M.Ben Ammar, A.U. Khan, Z. M. Almarhoon, A.A. Alanazi, M.E.A. Zaki, Magnetic properties of different phases iron oxide nanoparticles prepared by micro emulsion-hydrothermal method, Sci. Rep. 15 (2025) 878, https://doi.org/10.1038/s41598-025-85145-5.
[50] M. Faraji, Y. Yamini, M. Rezaee, Magnetic nanoparticles: Synthesis, stabilization, functionalization, characterization, and applications, J. Iran. Chem. Soc. 7 (2010) 1–37, https://doi.org/10.1007/BF03245856.
[51] L. Gonzalez-Moragas, S.M. Yu, N. Murillo-Cremaes, A. Laromaine, A. Roig, Scale-up synthesis of iron oxide nanoparticles by microwave-assisted thermal decomposition, Chem. Eng. J. 281 (2015) 87–95, https://doi.org/10.1016/j.cej.2015.06.066.
[52] A.M. Abd-Elnaiem, A. Hakamy, N. Afify, M. Omer, R.F. Abdelbaki, Nanoarchitectonics of zinc nickel ferrites by the hydrothermal method for improved structural and magnetic properties, J. Alloy. Compd. 984 (2024) 173941, https://doi.org/10.1016/J.JALLCOM.2024.173941.
[53] G. Unsoy, S. Yalcin, R. Khodadust, G. Gunduz, U. Gunduz, Synthesis optimization and characterization of chitosan- coated iron oxide nanoparticles produced for biomedical applications, J. Nanopart. Res (2012) 1–13, https://doi.org/10.1007/s11051-012-0964-8.
[54] M. Hashim, M.M. Ismail, K.M. Batoo, M. Hadi, S.J. Salih, S.S. Meena, R.B. Jotania, N.P. Kumar, K.C.B. Naidu, S.E. Shirsath, Structural, optical, and dielectric properties of Co0.6Mn0.4GdxFe2-xO4 ferrites prepared through sonochemical method, Ceram. Int 50 (2024) 42677–42685, https://doi.org/10.1016/J.CERAMINT.2024.08.112.
[55] B. Cardoso, G. Nobrega, M. Machado, R.A. Lima, Green synthesis of copper ferrite-based nanofluids using Chlorella vulgaris for heat transfer enhancement, J. Mol. Liq. 428 (2025), https://doi.org/10.1016/J.MOLLIQ.2025.127498.
[56] H. Hussein, S.S. Ibrahim, S.A. Khairy, Biosynthesis of CoFe2O4 ferrite nanoparticles using Greek yogurt solution: Deep structural insights and appraisal

for ecological mitigation via quartz crystal microbalance, J. Water Process Eng. 65 (2024) 105856, https://doi.org/10.1016/J.JWPE.2024.105856.
[57] R. Massart, Preparation of Aqueous Magnetic Liquids in Alkaline and Acidic Media, IEEE Trans. Magn. 17 (1981) 1247–1248, https://doi.org/10.1109/TMAG.1981.1061188.
[58] N.A. Frey, S. Peng, K. Cheng, S. Sun, Magnetic nanoparticles: synthesis, functionalization, and applications in bioimaging and magnetic energy storage, Chem. Soc. Rev. 38 (2009) 2532–2542, https://doi.org/10.1039/b815548h.
[59] T. Belin, N. Guigue-Millot, T. Caillot, D. Aymes, J.C. Niepce, Influence of Grain Size, Oxygen Stoichiometry, and Synthesis Conditions on the -Fe2O3 Vacancies Ordering and Lattice Parameters, J. Solid State Chem. 163 (2002) 459–465, https://doi.org/10.1006/jssc.2001.9426.
[60] H.A. Hamad, M.M. Abd El-latif, A.B. Kashyout, W.A. Sadik, M.Y. Feteha, Study on synthesis of superparamagnetic spinel cobalt ferrite nanoparticles as layered double hydroxides by co-precipitation method, Russ. J. Gen. Chem. 84 (2014) 2031–2036, https://doi.org/10.1134/S1070363214100296.
[61] S.D. Topel, Ö. Topel, R.B. Bostancioğlu, A.T. Koparal, Synthesis and characterization of Bodipy functionalized magnetic iron oxide nanoparticles for potential bioimaging applications, Colloids Surf. B Biointerfaces 128 (2015) 245–253, https://doi.org/10.1016/j.colsurfb.2015.01.043.
[62] R. Bhandari, P. Gupta, T. Dziubla, J.Z. Hilt, Single step synthesis, characterization and applications of curcumin functionalized iron oxide magnetic nanoparticles, Materials Science Engineering C 67 (2016) 59–64, https://doi.org/10.1016/j.msec.2016.04.093.
[63] L. Shen, Y. Qiao, Y. Guo, S. Meng, G. Yang, M. Wu, J. Zhao, Facile co-precipitation synthesis of shape-controlled magnetite nanoparticles, Ceram. Int 40 (2013) 1519–1524, https://doi.org/10.1016/j.ceramint.2013.07.037.
[64] R.M. Ali, M.R. Elkatory, H.A. Hamad, Highly active and stable magnetically recyclable CuFe2O4 as a heterogenous catalyst for efficient conversion of waste frying oil to biodiesel, Fuel 268 (2020) 117297, https://doi.org/10.1016/j.fuel.2020.117297.
[65] M. Abd El Aleem Ali Ali El-Remaily, H.A. Hamad, Synthesis and characterization of highly stable superparamagnetic CoFe2O4 nanoparticles as a catalyst for novel synthesis of thiazolo[4,5-b]quinolin-9-one derivatives in aqueous medium, J. Mol. Catal. A Chem. 404–405 (2015) 148–155, https://doi.org/10.1016/j.molcata.2015.04.023.
[66] J. Li, X. Shi, M. Shen, Hydrothermal Synthesis and Functionalization of Iron Oxide Nanoparticles for MR Imaging Applications, Part. Part. Syst. Charact. 31 (2014) 1223–1237, https://doi.org/10.1002/ppsc.201400087.
[67] M. Zhu, Y. Wang, D. Meng, X. Qin, G. Diao, Hydrothermal Synthesis of Hematite Nanoparticles and Their Electrochemical Properties, 2012, J. Phys. Chem. C. 116 (2012) 16276–16285.
[68] W. Cheng, X. Xu, F. Wu, J. Li, Synthesis of cavity-containing iron oxide nanoparticles by hydrothermal treatment of colloidal dispersion, Mater. Lett. 164 (2016) 210–212, https://doi.org/10.1016/j.matlet.2015.10.170.
[69] M. Zahid, N. Nadeem, M.A. Hanif, I.A. Bhatti, H.N. Bhatti, G. Mustafa, Metal Ferrites and Their Graphene-Based Nanocomposites: Synthesis, Characterization, and Applications in Wastewater Treatment. Nanotechnology in the Life Sciences, Magnetic Nanostructures, Springer, 2019, pp. 181–212, https://doi.org/10.1007/978-3-030-16439-3_10.
[70] A. Lu, E.L. Salabas, F. Schüth, Magnetic Nanoparticles: Synthesis, Protection, Functionalization, and Application, Angew. Chem. Int Ed. Engl. 46 (2007) 1222–1244, https://doi.org/10.1002/anie.200602866.
[71] B.K. Paul, S.P. Moulik, Uses and applications of microemulsions, Curr. Sci. 80 (2001).
[72] A.K. Gupta, M. Gupta, Synthesis and surface engineering of iron oxide nanoparticles for biomedical applications, Biomaterials 26 (2005) 3995–4021, https://doi.org/10.1016/j.biomaterials.2004.10.012.
[73] T. Lu, J. Wang, J. Yin, A. Wang, X. Wang, T. Zhang, Surfactant effects on the microstructures of Fe3O4 nanoparticles synthesized by microemulsion method, Colloids Surf. A Physicochem Eng. Asp. 436 (2013) 675–683, https://doi.org/10.1016/j.colsurfa.2013.08.004.
[74] O. Veiseh, C. Sun, J. Gunn, N. Kohler, P. Gabikian, D. Lee, N. Bhattarai, R. Ellenbogen, R. Sze, A. Hallahan, J. Olson, M. Zhang, Optical and MRI Multifunctional Nanoprobe for Targeting Gliomas, Nano Lett. 5 (2005) 1003–1008.
[75] R. Hufschmid, H. Arami, R.M. Ferguson, M. Gonzales, E. Teeman, L.N. Brush, N. D. Browning, K.M. Krishnan, Synthesis of phase-pure and monodisperse iron oxide nanoparticles by thermal decomposition, Nanoscale 7 (2015) 11142–11154, https://doi.org/10.1039/c5nr01651g.
[76] S. O'Brien, L. Brus, C.B. Murray, Synthesis of Monodisperse Nanoparticles of Barium Titanate: Toward a Generalized Strategy of Oxide Nanoparticle Synthesis, J. Am. Chem. Soc. 123 (2001) 12085–12086.
[77] F.X. Redl, C.T. Black, G.C. Papaefthymiou, R.L. Sandstrom, M. Yin, H. Zeng, C. B. Murray, S.P.O. Brien, Magnetic, Electronic, and Structural Characterization of Nonstoichiometric Iron Oxides at the Nanoscale, J. Am. Chem. Soc. 126 (2004) 14583–14599.
[78] N.R. Jana, Y. Chen, X. Peng, Size- and Shape-Controlled Magnetic (Cr, Mn, Fe, Co, Ni) Oxide Nanocrystals via a Simple and General Approach, Chem. Mater. 16 (2004) 3931–3935.
[79] G. Salazar-Alvarez, J. Qin, V. Sepelak, I. Bergmann, M. Vasilakaki, K.N. Trohidou, J.D. Ardisson, W.A.A. Macedo, M. Mikhaylova, M. Muhammed, M.D. Baro, J. Nogués, Cubic versus Spherical Magnetic Nanoparticles: The Role of Surface Anisotropy, J. Am. Chem. Soc. 130 (2008) 13234–13239.
[80] M. Elkady, H. Shokry, H. Hamad, Microwave-Assisted Synthesis of Magnetic Hydroxyapatite for Removal of Heavy Metals from Groundwater, Chem. Eng. Technol. 41 (2018) 553–562, https://doi.org/10.1002/ceat.201600631.
[81] W. Wang, Microwave-induced polyol-process synthesis of M II Fe 2 O 4 (M = Mn, Co) nanoparticles and magnetic property, Mater. Chem. Phys. 108 (2008) 227–231, https://doi.org/10.1016/j.matchemphys.2007.09.022.
[82] Y. Wang, I. Nkurikiyimfura, Z. Pan, Sonochemical Synthesis of Magnetic Nanoparticles, Chem. Eng. Commun. 202 (2015) 616–621, https://doi.org/10.1080/00986445.2013.858039.
[83] R. Seshadri, Oxide Nanoparticles, Chemistry Nanomaterials Synthesis Properties Applications 1 (2005) 94–112.
[84] K.S. Suslick, S.-B. Choe, A.A. Cichowlas, M.W. Grinstaff, Sonochemical synthesis of amorphous iron, Nature 353 (1991) 414–416.
[85] M. Abbas, M. Takahashi, C. Kim, Facile sonochemical synthesis of high-moment magnetite (Fe3O4) nanocube, J. Nanopart. Res. 15 (2013) 1354, https://doi.org/10.1007/s11051-012-1354-y.
[86] J.H. Bang, K.S. Suslick, Sonochemical Synthesis of Nanosized Hollow Hematite, J. Am. Chem. Soc. 129 (2007) 2242–2243.
[87] S. Gul, S.B. Khan, I.U. Rehman, M.A. Khan, M.I. Khan, A Comprehensive Review of Magnetic Nanomaterials Modern Day Theranostics, Front. Mater. 6 (2019) 1–15, https://doi.org/10.3389/fmats.2019.00179.
[88] V.V.T. Padil, M. Černík, Green synthesis of copper oxide nanoparticles using gum karaya as a biotemplate and their antibacterial application, Int J. Nanomed. 8 (2013) 889–898.
[89] K. Shameli, M.Bin Ahmad, A. Zamanian, P. Sangpour, P. Shabanzadeh, Y. Abdollahi, M. Zargar, Green biosynthesis of silver nanoparticles using Curcuma longa tuber powder, Int J. Nanomed. 7 (2012) 5603–5610.
[90] M. Pourhassan-moghaddam, N. Zarghami, A. Mohsenifar, M. Rahmati-yamchi, D. Gholizadeh, A. Akbarzadeh, M. De Guardia, K. Nejati-koshki, Watercress-based gold nanoparticles: biosynthesis, mechanism of formation and study of their biocompatibility in vitro, Micro Nano Lett. 9 (2014) 345–350, https://doi.org/10.1049/mnl.2014.0063.
[91] Y. Vitta, M. Figueroa, M. Calderon, C. Ciangherotti, Synthesis of Iron Nanoparticles from aqueous extract of Eucalyptus robusta Sm and evaluation of antioxidant and antimicrobial activity, Mater. Sci. Energy Technol. 3 (2020) 97–103, https://doi.org/10.1016/j.mset.2019.10.014.
[92] A.I. Lukman, B. Gong, C.E. Marjo, U. Roessner, A.T. Harris, and anti-bacterial performance of discrete Ag nanoparticles using Medicago sativa seed exudates (Journal of Colloid and Interface Science Facile synthesis, stabilization), J. Colloid Interface Sci. 353 (2011) 433–444, https://doi.org/10.1016/j.jcis.2010.09.088.
[93] N. Vigneshwaran, N.M. Ashtaputre, P.V. Varadarajan, R.P. Nachane, K. M. Paralikar, R.H. Balasubramanya, Biological synthesis of silver nanoparticles using the fungus Aspergillus flavus, Mater. Lett. 61 (2007) 1413–1418, https://doi.org/10.1016/j.matlet.2006.07.042.
[94] B.I. Willner, R. Baron, B. Willner, Growing Metal Nanoparticles by Enzymes, Adv. Mater. 18 (2006) 1109–1120, https://doi.org/10.1002/adma.200501865.
[95] M. Mahdavi, F. Namvar, M.Bin Ahmad, R. Mohamad, Green Biosynthesis and Characterization of Magnetic Iron Oxide (Fe3O4) Nanoparticles Using Seaweed (Sargassum muticum) Aqueous Extract, Molecules 18 (2013) 5954–5964, https://doi.org/10.3390/molecules18055954.
[96] M. Forough, K. Farhadi, Biological and green synthesis of silver nanoparticles, Turk. J. Eng. Env. Sci. 34 (2010) 281–287, https://doi.org/10.3906/muh-1005-30.
[97] A. Bharde, D. Rautaray, V. Bansal, A. Ahmad, I. Sarkar, S.M. Yusuf, M. Sanyal, M. Sastry, Extracellular Biosynthesis of Magnetite using Fungi, Small 2 (2006) 135–141, https://doi.org/10.1002/smll.200500180.
[98] S. Kanagasubbulakshmi, K. Kadirvelu, Green Synthesis of Iron Oxide Nanoparticles using Lagenaria siceraria and Evaluation of its Antimicrobial Activity, Def. Life Sci. J. 2 (2017) 422–427.
[99] W. Jiang, H.C. Yang, S.Y. Yang, H.E. Horng, J.C. Hung, Y.C. Chen, C. Hong, Preparation and properties of superparamagnetic nanoparticles with narrow size distribution and biocompatible, J. Magn. Magn. Mater. 283 (2004) 210–214, https://doi.org/10.1016/j.jmmm.2004.05.022.
[100] L.H. Reddy, J.L. Arias, J. Nicolas, P. Couvreur, Magnetic Nanoparticles: Design and Characterization, Toxicity and Biocompatibility, Pharmaceutical and Biomedical Applications, Chem. Rev. 112 (2012) 5818–5878, https://doi.org/10.1021/cr300068p.
[101] G. Unsoy, S. Yalcin, R. Khodadust, G. Gunduz, U. Gunduz, Synthesis optimization and characterization of chitosan-coated iron oxide nanoparticles produced for biomedical applications, J. Nanopart. Res. 14 (2012) 964, https://doi.org/10.1007/s11051-012-0964-8.
[102] A. Soufi, H. Hajjaoui, R. Elmoubarki, M. Abdennouri, Spinel ferrites nanoparticles: Synthesis methods and application in heterogeneous Fenton oxidation of organic pollutants – A review, Appl. Surf. Sci. Adv. 6 (2021) 100145, https://doi.org/10.1016/j.apsadv.2021.100145.
[103] S. Laurent, D. Forge, M. Port, A. Roch, C. Robic, L. Vander Elst, R.N. Muller, Magnetic iron oxide nanoparticles: synthesis, stabilization, vectorization, physicochemical characterizations, and biological applications, Chem. Rev. 108 (2008) 2064–2110, https://doi.org/10.1021/cr068445e.
[104] Y.P. Yew, K. Shameli, M. Miyake, N.B.B. Ahmad Khairudin, S.E.B. Mohamad, T. Naiki, K.X. Lee, Green biosynthesis of superparamagnetic magnetite Fe3O4 nanoparticles and biomedical applications in targeted anticancer drug delivery system: A review, Arab. J. Chem. 13 (2020) 2287–2308, https://doi.org/10.1016/j.arabjc.2018.04.013.

[105] T. Dippong, E.A. Levei, O. Cadar, Recent advances in synthesis and applications of MFe2O4 (M = Co, Cu, Mn, Ni, Zn) nanoparticles, Nanomaterials 11 (2021) 3–8, https://doi.org/10.3390/nano11061560.

[106] F. Meng, T. Hao, W. Tian, J. Zhao, S. Wang, H. Zhang, Photocatalytic aqueous environmental remediation via two-dimensional carbon nitride nanosheets, Surf. Interfaces 44 (2024) 103717, https://doi.org/10.1016/J.SURFIN.2023.103717.

[107] G. Litsardakis, I. Manolakis, C. Serletis, K.G. Efthimiadis, Effects of Gd substitution on the structural and magnetic properties of strontium hexaferrites, 316 (2007) 170–173. https://doi.org/10.1016/j.jmmm.2007.02.046.

[108] R. Valenzuela, Novel Applications of Ferrites, Phys. Res. Int. 2012 (2012) 1–9, https://doi.org/10.1155/2012/591839.

[109] D.H.K. Reddy, Y.-S. Yun, Spinel ferrite magnetic adsorbents: Alternative future materials for water purification? Coord. Chem. Rev. 315 (2016) 90–111, https://doi.org/10.1016/j.ccr.2016.01.012.

[110] W. Wang, Q. Hao, W. Lei, X. Xia, X. Wang, Ternary nitrogen-doped graphene / nickel ferrite / polyaniline nanocomposites for high-performance supercapacitors, J. Power Sources 269 (2014) 250–259, https://doi.org/10.1016/j.jpowsour.2014.07.010.

[111] S. Sagadevan, Z.Z. Chowdhury, R.F. Rafique, Preparation and Characterization of Nickel ferrite Nanoparticles via Co-precipitation Method, Mater. Res. 21 (2018) 21–25.

[112] H. Ehrhardt, S.J. Campbell, M. Hofmann, Magnetism of the nanostructured spinel zinc ferrite, Scr. Mater. 48 (2003) 1141–1146, https://doi.org/10.1016/S1359-6462(02)00598-5.

[113] Z. Szotek, W.M. Temmerman, D. Ködderitzsch, A. Svane, L. Petit, H. Winter, Electronic structures of normal and inverse spinel ferrites from first principles, Phys. Rev. B 74 (2006) 174431, https://doi.org/10.1103/PhysRevB.74.174431.

[114] A. Boudjemaa, A. Rebahi, B. Terfassa, R. Chebout, Fe 2 O 3 / carbon spheres for ef fi cient photo-catalytic hydrogen production from water and under visible light irradiation (Solar Energy Materials & Solar Cells), Sol. Energy Mater. Sol. Cells 140 (2015) 405–411, https://doi.org/10.1016/j.solmat.2015.04.036.

[115] I. Andjelkovic, D.N.H. Tran, S. Kabiri, S. Azari, M. Markovic, D. Losic, Graphene Aerogels Decorated with α-FeOOH Nanoparticles for Efficient Adsorption of Arsenic from Contaminated Waters, ACS Appl. Mater. Interfaces 7 (2015) 9758–9766, https://doi.org/10.1021/acsami.5b01624.

[116] A.B. Mugutkar, S.K. Gore, U.B. Tumberphale, V.V. Jadhav, R.S. Mane, S. M. Patange, S.S. Jadhav, S.F. Shaikh, M. Ubaidullah, A.M. Al-Enizi, The role of La3+ substitution in modification of the magnetic and dielectric properties of the nanocrystalline Co-Zn ferrites, J. Magn. Magn. Mater. 502 (2020) 166490, https://doi.org/10.1016/j.jmmm.2020.166490.

[117] S.K. Gore, S.S. Jadhav, V.V. Jadhav, S.M. Patange, M. Naushad, R.S. Mane, K. H. Kim, The structural and magnetic properties of dual phase cobalt ferrite, Sci. Rep. (2017) 1–9, https://doi.org/10.1038/s41598-017-02784-z.

[118] K.R. Sanchez-Lievanos, J.L. Stair, K.E. Knowles, Cation Distribution in Spinel Ferrite Nanocrystals: Characterization, Impact on their Physical Properties, and Opportunities for Synthetic Control, Inorg. Chem. 60 (2021) 4291–4305, https://doi.org/10.1021/acs.inorgchem.1c00040.

[119] R.T. Olsson, G. Salazar-alvarez, M.S. Hedenqvist, U.W. Gedde, F. Lindberg, S. J. Savage, Controlled Synthesis of Near-Stoichiometric Cobalt Ferrite Nanoparticles, Chem. Mater. 17 (2005) 5109–5118.

[120] Z. Yan, J. Luo, Effects of Ce Zn co-substitution on structure, magnetic and microwave absorption properties of nickel ferrite nanoparticles, J. Alloy. Compd. 695 (2017) 1185–1195, https://doi.org/10.1016/j.jallcom.2016.08.333.

[121] Y. Zhang, S. Park, Stabilization of dispersed CuPd bimetallic alloy nanoparticles on ZIF-8 for photoreduction of Cr (VI) in aqueous solution, Chem. Eng. J. 369 (2019) 353–362, https://doi.org/10.1016/j.cej.2019.03.083.

[122] R. Mohan, M.P. Ghosh, S. Mukherjee, nanoparticles (Journal of Magnetism and Magnetic Materials), J. Magn. Magn. Mater. 458 (2018) 193–199, https://doi.org/10.1016/j.jmmm.2018.03.030.

[123] Y. Diao, Z. Yan, M. Guo, X. Wang, Magnetic multi-metal co-doped magnesium ferrite nanoparticles: An efficient visible light-assisted heterogeneous Fenton-like catalyst synthesized from saprolite laterite ore, J. Hazard Mater. 344 (2018) 829–838, https://doi.org/10.1016/j.jhazmat.2017.11.029.

[124] S.K. Rashmi, H.S. Bhojya Naik, H. Jayadevappa, R. Viswanath, S.B. Patil, M. Madhukara Naik, Solar light responsive Sm-Zn ferrite nanoparticle as efficient photocatalyst, Mater. Sci. Eng. B Solid State Mater. Adv. Technol. 225 (2017) 86–97, https://doi.org/10.1016/j.mseb.2017.08.012.

[125] B. Issa, I. Obaidat, B. Albiss, Y. Haik, Magnetic Nanoparticles: Surface Effects and Properties Related to Biomedicine Applications, Int J. Mol. Sci. 14 (2013) 21266–21305, https://doi.org/10.3390/ijms141121266.

[126] S.V. Bhandare, R. Kumar, A.V. Anupama, M. Mishra, R.V. Kumar, V.M. Jali, B. Sahoo, Effect of Mg-substitution in Co – Ni-Ferrites: Cation distribution and magnetic properties, Mater. Chem. Phys. 251 (2020) 123081, https://doi.org/10.1016/j.matchemphys.2020.123081.

[127] P.R. Shukla, S. Wang, H.M. Ang, M.O. Tadé, Photocatalytic oxidation of phenolic compounds using zinc oxide and sulphate radicals under artificial solar light, 70, Sep. Purif. Technol. 70 (2010) 338–344, https://doi.org/10.1016/j.seppur.2009.10.018.

[128] R. Sharma, S. Singhal, Photodegradation of textile dye using magnetically recyclable heterogeneous spinel ferrites, J. Chem. Technol. Biotechnol. 90 (2015) 955–962, https://doi.org/10.1002/jctb.4409.

[129] A. Galal, K.M. Amin, N.F. Atta, H.A. Abd El-Rehim, Protective ability of graphene prepared by γ-irradiation and impregnated with organic inhibitor applied on AISI 316 stainless steel, J. Alloy. Compd. 695 (2017) 638–647, https://doi.org/10.1016/j.jallcom.2016.11.081.

[130] M.A. Aldeeb, N. Morgan, A. Abouelsayed, K.M. Amin, S. Hassaballa, Electrical and Optical Characterization of Acetylene RF CCP for Synthesis of Different Forms of Hydrogenated Amorphous Carbon Films, Plasma Chem. Plasma Process. 40 (2020) 387–406, https://doi.org/10.1007/s11090-019-10031-8.

[131] M.A. Aldeeb, N. Morgan, A. Abouelsayed, K.M. Amin, S. Hassablla, Correlation of acetylene plasma discharge environment and the optical and electronic properties of the hydrogenated amorphous carbon films, Diam. Relat. Mater. 96 (2019) 74–84, https://doi.org/10.1016/j.diamond.2019.04.021.

[132] A. Behera, D. Kandi, S.M. Majhi, S. Martha, K. Parida, Facile synthesis of ZnFe 2 O 4 photocatalysts for decolourization of organic dyes under solar irradiation, Beilstein J. Nanotechnol. 9 (2018) 436–446, https://doi.org/10.3762/bjnano.9.42.

[133] C. Su, Y. Guo, L. Yu, J. Zou, Z. Zeng, L. Li, Insight into specific surface area, microporosity and N, P co-doping of porous carbon materials in the acetone adsorption, Mater. Chem. Phys. 258 (2021) 123930, https://doi.org/10.1016/j.matchemphys.2020.123930.

[134] H.S. Mund, B.L. Ahuja, Structural and magnetic properties of Mg doped cobalt ferrite nano particles prepared by sol-gel method, Mater. Res Bull. (2016), https://doi.org/10.1016/j.materresbull.2016.09.027.

[135] G. Fan, J. Tong, F. Li, Visible-light-induced photocatalyst based on cobalt-doped zinc ferrite nanocrystals, Ind. Eng. Chem. Res 51 (2012) 13639–13647, https://doi.org/10.1021/ie201933g.

[136] X. Hou, J. Feng, X. Xu, M. Zhang, Synthesis and characterizations of spinel MnFe 2 O 4 nanorod by seed – hydrothermal route, J. Alloy. Compd. 491 (2010) 258–263, https://doi.org/10.1016/j.jallcom.2009.10.029.

[137] A.F. Cabrera, C.E.R. Torres, S.G. Marchetti, S.J. Stewart, Degradation of methylene blue dye under dark and visible light conditions in presence of hybrid composites of nanostructured MgFe 2 O 4 ferrites and oxygenated organic compounds (Journal of Environmental Chemical Engineering), J. Environ. Chem. Eng. 8 (2020) 104274, https://doi.org/10.1016/j.jece.2020.104274.

[138] A.E. Berkowitz, W.J. Schuele, Magnetic Properties of Some Ferrite Micropowders, J. Appl. Phys. 134 (1959) 10–12, https://doi.org/10.1063/1.2185853.

[139] M.I.A. Abdel Maksoud, R.A. Fahim, A.E. Shalan, M. Abd Elkodous, S.O. Olojede, A.I. Osman, C. Farrell, A.H. Al-Muhtaseb, A.S. Awed, A.H. Ashour, D.W. Rooney, Advanced materials and technologies for supercapacitors used in energy conversion and storage: a review, Environ. Chem. Lett. 19 (2021) 375–439, https://doi.org/10.1007/s10311-020-01075-w.

[140] R. Ali, A. Mahmood, M.A. Khan, A.H. Chughtai, M. Shahid, I. Shakir, M.F. Warsi, Impacts of Ni-Co substitution on the structural, magnetic and dielectric properties of magnesium nano-ferrites fabricated by micro-emulsion method, J. Alloy. Compd. 584 (2014) 363–368, https://doi.org/10.1016/j.jallcom.2013.08.114.

[141] A. Franco, M.S. Silva, High temperature magnetic properties of magnesium ferrite nanoparticles, J. Appl. Phys. 109 (2011) 15–18, https://doi.org/10.1063/1.3536790.

[142] G. Busca, E. Finocchio, V. Lorenzelli, M. Trombetta, S.A. Rossini, IR study of alkene allylic activation on magnesium ferrite and alumina catalysts, J. Chem. Soc. Faraday Trans. 92 (1996) 4687–4693, https://doi.org/10.1039/ft9969204687.

[143] S.A. Oliver, R.J. Willey, H.H. Hamdeh, G. Oliveri, G. Busca, Structure and magnetic properties of magnesium ferrite fine powders, Scr. Metall. Et. Mater. 33 (1995) 1695–1701, https://doi.org/10.1016/0956-716X(95)00412-O.

[144] A. Verma, R. Chatterjee, Effect of zinc concentration on the structural, electrical and magnetic properties of mixed Mn-Zn and Ni-Zn ferrites synthesized by the citrate precursor technique, J. Magn. Magn. Mater. 306 (2006) 313–320, https://doi.org/10.1016/j.jmmm.2006.03.033.

[145] K.M. Amin, A.M. Partila, H.A. Abd El-Rehim, N.M. Deghiedy, Antimicrobial ZnO Nanoparticle–Doped Polyvinyl Alcohol/Pluronic Blends as Active Food Packaging Films, Part. Part. Syst. Charact. 37 (2020), https://doi.org/10.1002/ppsc.202000006.

[146] R. Sharma, S. Singhal, Structural, magnetic and electrical properties of zinc doped nickel ferrite and their application in photo catalytic degradation of methylene blue, Physica B Physics Condensed Matter 414 (2013) 83–90, https://doi.org/10.1016/j.physb.2013.01.015.

[147] M. El Kady, H. Shokry, H. Hamad, Effect of superparamagnetic nanoparticles on the physicochemical properties of nano hydroxyapatite for groundwater treatment: Adsorption mechanism of Fe(II) and Mn(II), RSC Adv. 6 (2016) 82244–82259, https://doi.org/10.1039/c6ra14497g.

[148] D. Bassyouni, M. Mohamed, E.S. El-Ashtoukhy, M.A. El-Latif, A. Zaatout, H. Hamad, Fabrication and characterization of electrospun Fe3O4/o-MWCNTs/polyamide 6 hybrid nanofibrous membrane composite as an efficient and recoverable adsorbent for removal of Pb (II), Microchem. J. 149 (2019) 103998, https://doi.org/10.1016/j.microc.2019.103998.

[149] M.A. Barakat, New trends in removing heavy metals from industrial wastewater, Arab. J. Chem. 4 (2011) 361–377, https://doi.org/10.1016/j.arabjc.2010.07.019.

[150] S. Jafari, M. Sillanpää, Adsorption of dyes onto modified titanium dioxide. Advanced Water Treatment, Elsevier, 2020, pp. 85–160, https://doi.org/10.1016/B978-0-12-819216-0.00002-3.

[151] A.E. Burakov, E.V. Galunin, I.V. Burakova, A.E. Kucherova, S. Agarwal, A. G. Tkachev, V.K. Gupta, Adsorption of heavy metals on conventional and nanostructured materials for wastewater treatment purposes: A review, Ecotoxicol. Environ. Saf. 148 (2018) 702–712, https://doi.org/10.1016/j.ecoenv.2017.11.034.

[152] M.A. Abbasi, K.M. Amin, M. Ali, Z. Ali, M. Atif, W. Ensinger, W. Khalid, Synergetic effect of adsorption-photocatalysis by GO−CeO2nanocomposites for photodegradation of doxorubicin, J. Environ. Chem. Eng. 10 (2022) 107078, https://doi.org/10.1016/j.jece.2021.107078.

[153] N.M. Mahmoodi, J. Abdi, D. Bastani, Direct dyes removal using modified magnetic ferrite nanoparticle, J. Environ. Health Sci. Eng. 12 (2014) 96, https://doi.org/10.1186/2052-336X-12-96.
[154] R.W. Coughlin, F.S. Ezra, Role of Surface Acidity in the Adsorption of Organic Pollutants on the Surface of Carbon, Environniental Sci. Technol. 2 (1968) 291–297.
[155] K. Harsha, P. Senthil, R.C. Panda, A review on heavy metal pollution, toxicity and remedial measures: Current trends and future perspectives, J. Mol. Liq. 290 (2019) 111197, https://doi.org/10.1016/j.molliq.2019.111197.
[156] P.S. Kumar, S. Ramalingam, C. Senthamarai, M. Niranjanaa, P. Vijayalakshmi, S. Sivanesan, Adsorption of dye from aqueous solution by cashew nut shell: Studies on equilibrium isotherm, kinetics and thermodynamics of interactions, DES 261 (2010) 52–60, https://doi.org/10.1016/j.desal.2010.05.032.
[157] R. Asadi, H. Abdollahi, M. Gharabaghi, Z. Boroumand, Effective removal of Zn (II) ions from aqueous solution by the magnetic MnFe 2 O 4 and CoFe 2 O 4 spinel ferrite nanoparticles with focuses on synthesis, characterization, adsorption, and desorption, Adv. Powder Technol. (2020), https://doi.org/10.1016/j.apt.2020.01.028.
[158] M. Bhowmik, A. Debnath, B. Saha, Fabrication of mixed phase CaFe $_2$ O $_4$ and MnFe $_2$ O $_4$ magnetic nanocomposite for enhanced and rapid adsorption of methyl orange dye: statistical modeling by neural network and response surface methodology, J. Dispers. Sci. Technol. 41 (2020) 1937–1948, https://doi.org/10.1080/01932691.2019.1642209.
[159] M. Meigoli, H. Esmaeili, R. Foroutan, Ultrasonic assisted synthesis of Kaolin / CuFe 2 O 4 nanocomposite for removing cationic dyes from aqueous media (Journal of Environmental Chemical Engineering), J. Environ. Chem. Eng. 8 (2020) 103869, https://doi.org/10.1016/j.jece.2020.103869.
[160] T. Ahmed, S.Sen Gupta, Adsorptive Accumulation of Methylene Blue Dye from Aqueous Effluent by NiFe2O4-GO Nano-adsorbent, World J. Chem. Educ. 9 (2021) 28–41, https://doi.org/10.12691/WJCE-9-1-5.
[161] Q. Sun, M. Tang, P. Vang, B. Chen, Biotemplated fabrication of a 3D hierarchical structure of magnetic ZnFe 2 O 4 / MgAl-LDH for ef fi cient elimination of dye from water, J. Alloy. Compd. 829 (2020) 154552, https://doi.org/10.1016/j.jallcom.2020.154552.
[162] A. Goldstein, A.J. Stevenson, Z. Cohen, M. Vulfson, Parasitic Light Absorption Processes in Transparent Polycrystalline MgAl2O4 and YAG, J. Am. Ceram. Soc. 7 (2013) 1–7, https://doi.org/10.1111/jace.12525.
[163] N. Sonoyama, K. Kawamura, A. Yamada, R. Kanno, Electrochemical Luminescence of Rare Earth Metal Ion Doped MgIn 2 O 4 Electrodes, J. Electrochem Soc. 153 (2006) 45–50, https://doi.org/10.1149/1.2158574.
[164] V. Zviagin, P. Richter, T. Böntgen, M. Lorenz, M. Ziese, D.R.T. Zahn, G. Salvan, M. Grundmann, R. Schmidt-Grund, Comparative study of optical and magneto-optical properties of normal, disordered, and inverse spinel-type oxides, Phys. Status Solidi (b) 253 (2016) 429–436, https://doi.org/10.1002/pssb.201552361.
[165] A.R. Molla, C.R. Kesavulu, R.P.S. Chakradhar, A. Tarafder, S.K. Mohanty, J. L. Rao, B. Karmakar, S.K. Biswas, Microstructure, mechanical, thermal, EPR, and optical properties of MgAl 2 O 4: Cr 3 + spinel glass – ceramic nanocomposites, J. Alloy. Compd. 583 (2014) 498–509, https://doi.org/10.1016/j.jallcom.2013.08.122.
[166] P. Chand, S. Vaish, P. Kumar, Structural, optical and dielectric properties of transition metal (MFe 2 O 4; M = Co, Ni and Zn) nanoferrites, Physica B Physics Condensed Matter 524 (2017) 53–63, https://doi.org/10.1016/j.physb.2017.08.060.
[167] S.S. Selima, M. Khairy, M.A. Mousa, Comparative studies on the impact of synthesis methods on structural, optical, magnetic and catalytic properties of CuFe2O4, Ceram. Int (2018), https://doi.org/10.1016/j.ceramint.2018.12.146.
[168] M.Y. Rafique, L. Pan, Q. Javed, M.Z. Iqbal, Growth of monodisperse nanospheres of MnFe 2 O 4 with enhanced magnetic and optical properties, Chin. Phys. B 22 (2013) 1–25.
[169] J. Kurian, M.J. Mathew, Structural, optical and magnetic studies of CuFe 2 O 4, MgFe 2 O 4 and ZnFe 2 O 4 nanoparticles prepared by hydrothermal / solvothermal method, J. Magn. Magn. Mater. (2017), https://doi.org/10.1016/j.jmmm.2017.10.124.
[170] D.D. Andhare, S.R. Patade, J.S. Kounsalye, K.M. Jadhav, Effect of Zn doping on structural, magnetic and optical properties of cobalt ferrite nanoparticles synthesized via. Co-precipitation method, Physica B Physics Condensed Matter 583 (2020) 412051, https://doi.org/10.1016/j.physb.2020.412051.
[171] P. Monisha, P. Priyadharshini, S.S. Gomathi, K. Pushpanathan, Ferro to superparamagnetic transition: Outcome of Ni doping in polyethylene glycol capped CoFe2O4 nanoparticles P. J. Alloy. Compd. (2020) 157447 https://doi.org/10.1016/j.jallcom.2020.157447.
[172] V. Tandon, M. Saleem, N. Kaurav, R.C. Dixit, Barium (Ba 2 +) doped Cu-Zn ferrite: Study of structural and optical properties Barium (, AIP Conf Proc 110009 (2020) 2–6. https://doi.org/10.1063/5.0019603.
[173] M.I.A.A. Maksoud, G.S. El-sayyad, A. Abokhadra, L.I. Soliman, A.H. Ashour, Influence of Mg 2 + substitution on structural, optical, magnetic, and antimicrobial properties of Mn – Zn ferrite nanoparticles, Journal Materials Science Materials Electronics (2020), https://doi.org/10.1007/s10854-019-02799-4.
[174] A.A. Al-ghamdi, F.S. Al-hazmi, L.S. Memesh, F.S. Shokr, L.M. Bronstein, Evolution of the structure, magnetic and optical properties of Ni 1 À x Cu x Fe 2 O 4 spinel ferrites prepared by soft mechanochemical method, J. Alloy. Compd. 712 (2017) 82–89, https://doi.org/10.1016/j.jallcom.2017.04.052.
[175] L. Renuka, P. Mishra, Y.S. Vidya, G. Banuprakash, K.S. Anantharaju, K.N. Harish, Facile surface modification of Nickel ferrite nanomaterial by different routes: Photoluminescence and photocatalytic activities (Materials Today: Proceedings), Mater. Today Proc. 46 (2021) 6022–6027, https://doi.org/10.1016/j.matpr.2020.12.1161.
[176] T.M. Hammad, S. Kuhn, A.A. Amsha, R. Hempelmann, Investigation of structural, optical, and magnetic properties of Co2 + ions substituted CuFe2O4 spinel ferrite nanoparticles prepared via precipitation approach, J. Aust. Ceram. Soc. (2021), https://doi.org/10.1007/s41779-020-00556-z.
[177] L.N. Anh, T.T. Loan, N.P. Duong, S. Soontaranon, T. Thi, V. Nga, T.D. Hien, Influence of Y and La substitution on particle size, structural and magnetic properties of nanosized nickel ferrite prepared by using citrate precursor method, J. Alloy. Compd. (2015), https://doi.org/10.1016/j.jallcom.2015.04.240.
[178] I. Das, T. Noori, G. Dhar, M.M. Ghangrekar, Synthesis of bimetallic iron ferrite Co0.5Zn0.5Fe2O4 as a superior catalyst for oxygen reduction reaction to replace noble metal catalysts in microbial fuel cell, Int J. Hydrog. Energy (2018) 2–11, https://doi.org/10.1016/j.ijhydene.2018.08.113.
[179] K.M. Amin, K.H. Lin, M. Duerrschnabel, L. Molina-Luna, W. Ensinger, Engineering Active Sites Enriched 2D-on-1D NiFe and NiCo Layered Double Hydroxide-Decorated Ni Nanowire Networks for Oxygen Evolution Reaction, ACS Sustain Chem. Eng. 11 (2023) 15410–15422, https://doi.org/10.1021/acssuschemeng.3c04505.
[180] M.G. Walter, E.L. Warren, J.R. Mckone, S.W. Boettcher, Q. Mi, E.A. Santori, N. S. Lewis, Solar Water Splitting Cells, Chem. Rev. 110 (2010) 6446–6473.
[181] B.B. Cui, H. Lin, J. Li, X. Li, J. Yang, J. Tao, Core – Ring Structured NiCo 2 O 4 Nanoplatelets: Synthesis, Characterization, and Electrocatalytic Applications, Adv. Funct. Mater. 18 (2008) 1440–1447, https://doi.org/10.1002/adfm.200700982.
[182] R. Nivetha, A.N. Grace, Manganese and zinc ferrite based graphene nanocomposites for electrochemical hydrogen evolution reaction, J. Alloy. Compd. 796 (2019) 185–195, https://doi.org/10.1016/j.jallcom.2019.05.021.
[183] N. Helaili, G. Mitran, I. Popescu, K. Bachari, I. Marcu, A. Boudjemaa, Photoelectrochemical properties of AFe2O4 (A = Co, Cu, Zn) ferrospinels for water photo-reduction, J. ELECTROANALYTICAL Chem. 4 (2015), https://doi.org/10.1016/j.jelechem.2015.01.018.
[184] S. Singh, N. Khare, Low field magneto-tunable photocurrent in CoFe 2 O 4 nanostructure films for enhanced photoelectrochemical properties, Sci. Rep. (2018) 1–8, https://doi.org/10.1038/s41598-018-24947-2.
[185] K. Yan, R. Chen, Q. Ling, Z. Zhao, Z. Zhou, X. Li, J. Lv, C. Cao, G. He, Z. Sun, M. Zhang, Rapid synthesis of Mn-doped NiFe2O4 nanosheet arrays for high-performance hybrid supercapacitors, Electro Acta 497 (2024) 144551, https://doi.org/10.1016/J.ELECTACTA.2024.144551.
[186] P. Kumar, J. Asokan, S. Sriram, M.C. Ramkumar, P.S. Kumar, M.G. Shalini, Impact of annealing on $ZnFe_2O_4$: Structural, optical, magnetic, photocatalytic, and antibacterial properties with DFT insights into optical parameters, J. Hazard. Mater. Adv. 17 (2025) 100594, https://doi.org/10.1016/J.HAZADV.2025.100594.
[187] M. Shobana, T. Raguram, N. Eswaramoorthy, G. Cárdenas-Jirón, K. Granados-Tavera, A.N. Alodhayb, K.E. Alzahrani, S. Pandiaraj, J. Geethapriya, C. Y R, Influence of Gd doping on the structural, optical, dielectric, and magnetic properties of ZnFe2O4: A combined experimental and theoretical study, Ceram. Int 51 (2025) 6748–6761, https://doi.org/10.1016/J.CERAMINT.2024.12.119.
[188] Y. Fang, S. Mullurkara, K.M. Taddei, P.R. Ohodnicki, G. Wang, Machine learning enabled accurate prediction of structural and magnetic properties of cobalt ferrite, NPJ Comput. Mater. 11 (2025) 103, https://doi.org/10.1038/s41524-025-01598-2.
[189] K.L.S. Rodríguez, J.J.M. Quintero, H.H. Medina Chanduví, A.V.G. Rebaza, R. Faccio, W.A. Adeagbo, W. Hergert, C.E.R. Torres, L.A. Errico, Ab-initio approach to the stability and the structural, electronic and magnetic properties of the (001) Znfe2O4 surface terminations, Appl. Surf. Sci. 499 (2020) 143859, https://doi.org/10.1016/j.apsusc.2019.143859.
[190] D. Fritsch, C. Ederer, Effect of epitaxial strain on the cation distribution in spinel ferrites CoFe2O4 and NiFe2O4: A density functional theory study, Appl. Phys. Lett. 99 (2011), https://doi.org/10.1063/1.3631676/123322.
[191] N.I. Sulaiman, N.H.H. Abu Bakar, M. Abu Bakar, Effect of Al-Doping on Structural and Adsorption Properties of NiFe2O4 via Modified Sol–Gel Approach for CO2 Adsorption, Chem. Afr. 7 (2024) 2139–2154, https://doi.org/10.1007/S42250-024-00879-5/METRICS.
[192] R. Wu, L. Li, Z. Lu, C. Sun, L. Cheng, R. Ye, R. Zhang, Q. Li, G. Feng, DFT insights into doping and oxygen vacancy effects on CO and CO_2 adsorptions over CuAl2O4 spinel surfaces, J. Catal. 434 (2024) 115502, https://doi.org/10.1016/J.JCAT.2024.115502.
[193] F. Liu, J. Liu, Y. Yang, X. Wang, A mechanistic study of CO oxidation over spinel MnFe 2 O 4 surface during chemical-looping combustion, Fuel 230 (2018) 410–417, https://doi.org/10.1016/j.fuel.2018.05.079.
[194] P. Saha, S. Amanullah, S. Barman, A. Dey, Electrochemical Reduction of CO2 to CH3OH Catalyzed by an Iron Porphyrinoid, J. Am. Chem. Soc. 147 (2025) 1497–1507, https://doi.org/10.1021/jacs.4c08922.
[195] K. Zheng, Y. Wu, J. Zhu, M. Wu, X. Jiao, L. Li, S. Wang, M. Fan, J. Hu, W. Yan, J. Zhu, Y. Sun, Y. Xie, Room-Temperature Photooxidation of CH4to CH3OH with Nearly 100% Selectivity over Hetero-ZnO/Fe2O3Porous Nanosheets, J. Am. Chem. Soc. 144 (2022) 12357–12366, https://doi.org/10.1021/jacs.2c03866.
[196] J.R. Huang, W.X. Shi, S.Y. Xu, H. Luo, J. Zhang, T.B. Lu, Z.M. Zhang, Water-Mediated Selectivity Control of CH3OH versus CO/CH4 in CO2 Photoreduction on Single-Atom Implanted Nanotube Arrays, Adv. Mater. 36 (2024) 2306906, https://doi.org/10.1002/adma.202306906.
[197] B. Kong, Y. Ren, M. Liu, J. Zhou, K. Wang, N. Wang, N. Li, Solar-wind energy complementary coupling realizes magnetic-field assisted efficient photocatalytic

CO2 reduction, Appl. Catal. B 334 (2023) 122858, https://doi.org/10.1016/J.APCATB.2023.122858.
[198] D. Hermosilla, C. Han, M.N. Nadagouda, L. Machala, A. Gascó, P. Campo, D. D. Dionysiou, Environmentally friendly synthesized and magnetically recoverable designed ferrite photo-catalysts for wastewater treatment applications, J. Hazard Mater. 381 (2020) 121200, https://doi.org/10.1016/J.JHAZMAT.2019.121200.
[199] T. Inoue, A. Fujishima, S. Konishi, K. Honda, Photoelectrocatalytic reduction of carbon dioxide in aqueous suspensions of semiconductor powders, 1979 277: 5698, Nature 277 (1979) 637–638, https://doi.org/10.1038/277637a0.
[200] C. Hiragond, S. Ali, S. Sorcar, S.-I. In, Hierarchical Nanostructured Photocatalysts for CO2 Photoreduction, Catalysts 9 (2019) 4, https://doi.org/10.3390/CATAL9040370.
[201] H. Ishida, Electrochemical/Photochemical CO2 Reduction Catalyzed by Transition Metal Complexes. Carbon Dioxide Chemistry, Capture and Oil Recovery, InTech, 2018, https://doi.org/10.5772/intechopen.75199.
[202] Y. Matsumoto, M. Obata, J. Hombo, Photocatalytic Reduction of Carbon Dioxide on p-Type CaFe2O4 Powder, J. Phys. Chem. 98 (2002) 2950–2951, https://doi.org/10.1021/J100062A035.
[203] Ž. Kovačič, B. Likozar, M. Huš, Photocatalytic CO2Reduction: A Review of Ab Initio Mechanism, Kinetics, and Multiscale Modeling Simulations, ACS Catal. (2020), https://doi.org/10.1021/acscatal.0c02557.
[204] C. Li, Y. Xu, W. Tu, G. Chen, R. Xu, Metal-free photocatalysts for various applications in energy conversion and environmental purification, Green. Chem. 19 (2017) 4, https://doi.org/10.1039/c6gc02856j.
[205] J. Jiang, C. Wen, Z. Tian, Y. Wang, Y. Zhai, L. Chen, Y. Li, Q. Liu, C. Wang, L. Ma, Manganese-Promoted Fe3O4 Microsphere for Efficient Conversion of CO2 to Light Olefins, Ind. Eng. Chem. Res 59 (2020) 2155–2162, https://doi.org/10.1021/acs.iecr.9b05342.
[206] Z. Zhang, Y. Lin, Q. Liu, X. Wang, X. Fu, W. Su, In situ α-Fe2O3 modified La2Ti2O7 with enhanced photocatalytic CO2 reduction activity, Catal. Sci. Technol. 11 (2021) 6438–6444, https://doi.org/10.1039/D1CY01275D.
[207] J. Song, Y. Lu, Y. Lin, Q. Liu, X. Wang, W. Su, A direct Z-scheme α-Fe2O3/LaTiO2N visible-light photocatalyst for enhanced CO2 reduction activity, Appl. Catal. B 292 (2021), https://doi.org/10.1016/J.APCATB.2021.120185.
[208] S. Yan, S. Ouyang, H. Xu, M. Zhao, X. Zhang, J. Ye, Co-ZIF-9/TiO2 nanostructure for superior CO2 photoreduction activity, J. Mater. Chem. A Mater. 4 (2016) 39, https://doi.org/10.1039/c6ta04620g.
[209] K. Wu, X. Dong, J. Zhu, P. Wu, C. Liu, Y. Wang, J. Wu, J. Hou, Z. Liu, X. Guo, Designing biomimetic porous celery: TiO2/ZnO nanocomposite for enhanced CO2 photoreduction, J. Mater. Sci. 53 (2018) 11595–11606, https://doi.org/10.1007/s10853-018-2397-y.
[210] A. Olivo, E. Ghedini, M. Signoretto, M. Compagnoni, I. Rossetti, Liquid vs. Gas Phase CO2 photoreduction process: Which is the effect of the reaction medium? Energ. (Basel) 10 (2017) 9, https://doi.org/10.3390/en10091394.
[211] J.C. Navarro, C. Hurtado, M. Gonzalez-Castaño, L.F. Bobadilla, S. Ivanova, F. L. Cumbrera, M.A. Centeno, J.A. Odriozola, Spinel ferrite catalysts for CO2 reduction via reverse water gas shift reaction, J. CO2 Util. 68 (2023) 102356, https://doi.org/10.1016/J.JCOU.2022.102356.
[212] T.P. Araújo, S. Mitchell, J. Pérez-Ramírez, Design Principles of Catalytic Materials for CO2 Hydrogenation to Methanol, Adv. Mater. 36 (2024) 2409322, https://doi.org/10.1002/adma.202409322.
[213] M. Tahir, Well-designed ZnFe2O4/Ag/TiO2 nanorods heterojunction with Ag as electron mediator for photocatalytic CO2 reduction to fuels under UV/visible light, J. CO2 Util. 37 (2020) 134–146, https://doi.org/10.1016/j.jcou.2019.12.004.
[214] L. Fu, H. Chen, K. Wang, X. Wang, Oxygen-vacancy generation in MgFe2O4 by high temperature calcination and its improved photocatalytic activity for CO2 reduction, J. Alloy. Compd. 891 (2022) 161925, https://doi.org/10.1016/j.jallcom.2021.161925.
[215] J. Guo, K. Wang, X. Wang, Photocatalytic reduction of CO2 with H2O vapor under visible light over Ce doped ZnFe2O4, Catal. Sci. Technol. 7 (2017) 24, https://doi.org/10.1039/c7cy01869j.
[216] G. Yang, Y. Li, Q. Wang, X. Wang, S. Zuo, H. Zhang, X. Ren, Y. He, F. Ichihara, J. Ye, Synergy between Confined Cobalt Centers and Oxygen Defects on α-Fe2O3 Platelets for Efficient Photocatalytic CO2 Reduction, Online Library, Accessed: Dec. 10 [Online]. Available, Wiley, 2022, https://doi.org/10.1002/solr.202100833.
[217] M.R. Uddin, M.R. Khan, M.W. Rahman, A. Yousuf, C.K. Cheng, Photocatalytic reduction of CO2 into methanol over CuFe2O4/TiO2 under visible light irradiation, React. Kinet. Mech. Catal. 116 (2015) 2, https://doi.org/10.1007/s11144-015-0911-7.
[218] R.G. Ciocarlan, N. Hoeven, E. Irtem, V. Van Acker, M. Mertens, E.M. Seftel, T. Breugelmans, P. Cool, Ferrite@TiO2-nanocomposites as Z-scheme photocatalysts for CO2 conversion: Insight into the correlation of the Co-Zn metal composition and the catalytic activity, J. CO2 Util. 36 (2020) 177–186, https://doi.org/10.1016/j.jcou.2019.11.012.
[219] L. Long, G. Lv, Q. Han, X. Wu, Y. Qian, D. Wang, Y. Zhou, Z. Zou, Achieving Direct Z-Scheme Charge Transfer through Constructing 2D/2D α-Fe2O3/CdS Heterostructure for Efficient Photocatalytic CO2Conversion, J. Phys. Chem. C. 125 (2021) 23142–23152, https://doi.org/10.1021/acs.jpcc.1c06259.
[220] Y. Wei, X. Li, Y. Zhang, Y. Yan, P. Huo, H. Wang, G-C3N4 quantum dots and Au nano particles co-modified CeO2/Fe3O4 micro-flowers photocatalyst for enhanced CO2 photoreduction, Renew. Energy 179 (2021) 756–765, https://doi.org/10.1016/J.RENENE.2021.07.091.
[221] M. Tahir, Well-designed ZnFe2O4/Ag/TiO2 nanorods heterojunction with Ag as electron mediator for photocatalytic CO2 reduction to fuels under UV/visible light, J. CO2 Util. 37 (2020) 134–146, https://doi.org/10.1016/j.jcou.2019.12.004.
[222] M. Padervand, B. Rhimi, C. Wang, One-pot synthesis of novel ternary Fe3N/Fe2O3/C3N4 photocatalyst for efficient removal of rhodamine B and CO2 reduction, J. Alloy. Compd. 852 (2021), https://doi.org/10.1016/J.JALLCOM.2020.156955.
[223] M. Padervand, S. Ghasemi, S. Hajiahmadi, C. Wang, K4Nb6O17/Fe3N/α-Fe2O3/C3N4 as an enhanced visible light-driven quaternary photocatalyst for acetamiprid photodegradation, CO2 reduction, and cancer cells treatment, Appl. Surf. Sci. 544 (2021), https://doi.org/10.1016/J.APSUSC.2021.148939.
[224] H.W. Guo, M.Q. Chen, Q. Zhong, Y.A. Wang, W.H. Ma, J. Ding, Synthesis of Z-scheme alpha-Fe2O3/g-C3N4 composite with enhanced visible-light photocatalytic reduction of CO2 to CH3OH, J. Co2 Util. 33 (2019) 233–241, https://doi.org/10.1016/j.jcou.2019.05.016.
[225] P. Kumar, C. Joshi, A. Barras, B. Sieber, A. Addad, L. Boussekey, S. Szunerits, R. Boukherroub, S.L. Jain, Core–shell structured reduced graphene oxide wrapped magnetically separable rGO@CuZnO@Fe3O4 microspheres as superior photocatalyst for CO2 reduction under visible light, Appl. Catal. B 205 (2017) 654–665, https://doi.org/10.1016/j.apcatb.2016.11.060.
[226] S. Kazemi Movahed, A. Najinasab, R. Nikbakht, M. Dabiri, Visible light assisted photocatalytic reduction of CO2 to methanol using Fe3O4@N-C/Cu2O nanostructure photocatalyst, J. Photochem. Photobio. A Chem. 401 (2020), https://doi.org/10.1016/j.jphotochem.2020.112763.
[227] X. Liu, Y. Chen, Q. Wang, L. Li, L. Du, G. Tian, Improved charge separation and carbon dioxide photoreduction performance of surface oxygen vacancy-enriched zinc ferrite@titanium dioxide hollow nanospheres with spatially separated cocatalysts, J. Colloid Interface Sci. 599 (2021) 1–11.
[228] D. Long, X. Li, Z. Yin, S. Fan, P. Wang, F. Xu, L. Wei, M.O. Tadé, S. Liu, Novel Co3O4 @ CoFe2O4 double-shelled nanoboxes derived from Metal–Organic Framework for CO2 reduction, J. Alloy. Compd. 854 (2021), https://doi.org/10.1016/j.jallcom.2020.156942.
[229] Y. Chen, G. Jia, Y. Hu, G. Fan, Y.H. Tsang, Z. Li, Z. Zou, Two-dimensional nanomaterials for photocatalytic CO2 reduction to solar fuels, Sustain Energy Fuels 1 (2017) 1875–1898, https://doi.org/10.1039/C7SE00344G.
[230] Z. Saleem, E. Pervaiz, M.U. Yousaf, M.B.K. Niazi, Two-Dimensional Materials and Composites as Potential Water Splitting Photocatalysts: A Review, 2020, Vol. 10, Page 464, Catalysts 10 (2020) 464, https://doi.org/10.3390/CATAL10040464.
[231] B.Y. Balarabe, T.Sh Atabaev, Advancing Photocatalysis: Insights from 2D Materials and Operational Parameters for Organic Pollutants Removal, Adv. Sustain Syst. 8 (2024) 2400483, https://doi.org/10.1002/adsu.202400483.
[232] Y. Xu, H. Tang, Y. Wang, X. Zhu, L. Yang, Graphene-Based Organic Semiconductor Film for Highly Selective Photocatalytic CO2 Reduction, Nanomaterials 15 (2025) 677, https://doi.org/10.3390/NANO15090677.
[233] H. Zhang, I. Abe, T. Oyumi, R. Ishii, K. Hara, Y. Izumi, Photocatalytic CO2 Reduction Using Ti3C2Xy (X = Oxo, OH, F, or Cl) MXene-ZrO2: Structure, Electron Transmission, and the Stability, Langmuir 40 (2024) 6330–6341, https://doi.org/10.1021/acs.langmuir.3c03883.
[234] M. Dąbrowski, S. Haldar, S. Khan, P.S. Keatley, D. Sagkovits, Z. Xue, C. Freeman, I. Verzhbitskiy, T. Griepe, U. Atxitia, G. Eda, H. Kurebayashi, E.J.G. Santos, R. J. Hicken, Ultrafast thermo-optical control of spins in a 2D van der Waals semiconductor, Nat. Commun. 16 (2025) 1–10, https://doi.org/10.1038/s41467-025-58065-1.
[235] M.R. Uddin, M.R. Khan, M.W. Rahman, A. Yousuf, C.K. Cheng, Photocatalytic reduction of CO2 into methanol over CuFe2O4/TiO2 under visible light irradiation, React. Kinet. Mech. Catal. 116 (2015) 2, https://doi.org/10.1007/s11144-015-0911-7.
[236] S.J. Arteaga-Díaz, S.I. Meramo-Hurtado, J. León-Pulido, A. Zuorro, A.D. González-Delgado, Environmental Assessment of Large Scale Production of Magnetite (Fe3O4) Nanoparticles via Coprecipitation, 2019, Vol. 9, Page 1682, Appl. Sci. 9 (2019) 1682, https://doi.org/10.3390/APP9081682.
[237] Z. Chen, W. Wei, H. Chen, B.J. Ni, Recent advances in waste-derived functional materials for wastewater remediation, EcoEnviron. Health 1 (2022) 86–104, https://doi.org/10.1016/j.eehl.2022.05.001.